2-1-2018

Studying the QCD medium in proton-proton collisions using PYTHIA

Omar Tarek Elsherif

Studying the QCD Medium in Proton-Proton Collisions Using PYTHIA

A thesis submitted in partial fulfillment of the requirements for the degree of Master of Science

By

Omar Tarek ElSherif

Department of Physics, American University in Cairo

August 2017

This page intentionally left blank.

Abstract

It is believed that in the first microsecond after the big bang, the universe was in a state known as the Quark-Gluon Plasma (QGP), where quarks and gluons were asymptotically free. Signatures of QGP like jet quenching and elliptic flow have been observed in heavy-ion collisions at RHIC and LHC experiments. The aim of this study was to investigate the possibility of QGP formation in proton-proton (p-p) collisions. PYTHIA was used to simulate the p-p collision at center-of-mass energies of $\sqrt{s_{_{NN}}} = 200\ GeV$ and $\sqrt{s_{_{NN}}} = 13\ TeV$ corresponding to the available energies of the current collider experiments. The ratios between the near-side and away-side yields associated with the high transverse momentum particles were calculated and compared for the low and high multiplicity events as a function of transverse momentum in order to search for such phase. For LHC energies at high multiplicity, away-side yields show suppression in comparison to near-side yields. This indicates that there is a possibility of creating QGP at high-energy high-multiplicity p-p collisions.[1]

[1]The work done in this thesis has resulted in an abstract that was accepted for poster sessions at EPS-HEP 2017 and XQCD 2017. Moreover, a journal article is under preparation.

Dedication

To my Father,
Mother, Brother
and Son.

Acknowlegements

I want to express my gratitude to my teacher and supervisor **Dr. Mohammad T. AlFiky** for his support throughout my thesis and master's degree, for mentoring me towards building a stronger physics background, and for his extreme help and support in planning my future academic career.

I would like to express my appreciation to my supervisor **Dr. Ahmed M. Hamed** for introducing me to such an exciting area of research, for his support and patience throughout my thesis, and for the long hours spent guiding me through my research.

I would like to deeply thank **Prof. Salah M. El-Sheikh** for guiding me during my master's degree, for exposing me to different research opportunities and experiences, and above all for his advice in times of need.

I would also like to thank my friends and family for their support and patience.

Contents

List of Figures

Chapter 1

Introduction

This chapter provides an introduction to various concepts and terminology related to elementary particle physics. Certain aspects of the strong nuclear force and Quantum Chromodynamics are discussed in more detail to set the stage for the Quark-Gluon Plasma phase.

1.1 The Standard Model of Particle Physics

At very short distances, it is believed the universe is made out of a number of elementary particles, which can be classified into fermions, interacting via gauge bosons, in addition to the Higgs boson. The current theory which describes these elementary particles and their interactions is known as the standard model of particle physics which is a gauge theory with the symmetry group of $SU(3) \times SU(2) \times U(1)$.

The standard model contains two main categories of spin-$\frac{1}{2}$ particles (fermions), which are quarks and leptons. Those fermions are classified into three generations, each is represented by one of the first three columns in figure 1.1

There are 6 quarks (up, down, charm, strange, top and bottom). Three of them have an electric charge of $\frac{2}{3}e$ (where e is the elementary charge) and the other three have a charge of $-\frac{1}{3}e$. Each quark has its own anti-quark with opposite electric charge.

Quarks possess another property called color charge, in which the quark could have one of three colors (red, green and blue). Only 'colorless' bound states of quarks can be observed in nature. Bound states of 3 quarks are called baryons, while bound states of one quark and one antiquark are called mesons.

Along with the electric and color charges, quarks also carry weak charges, and hence they can interact via electromagnetic, strong and weak interactions.

On the other hand, all the leptons carry weak charge but no color charge,

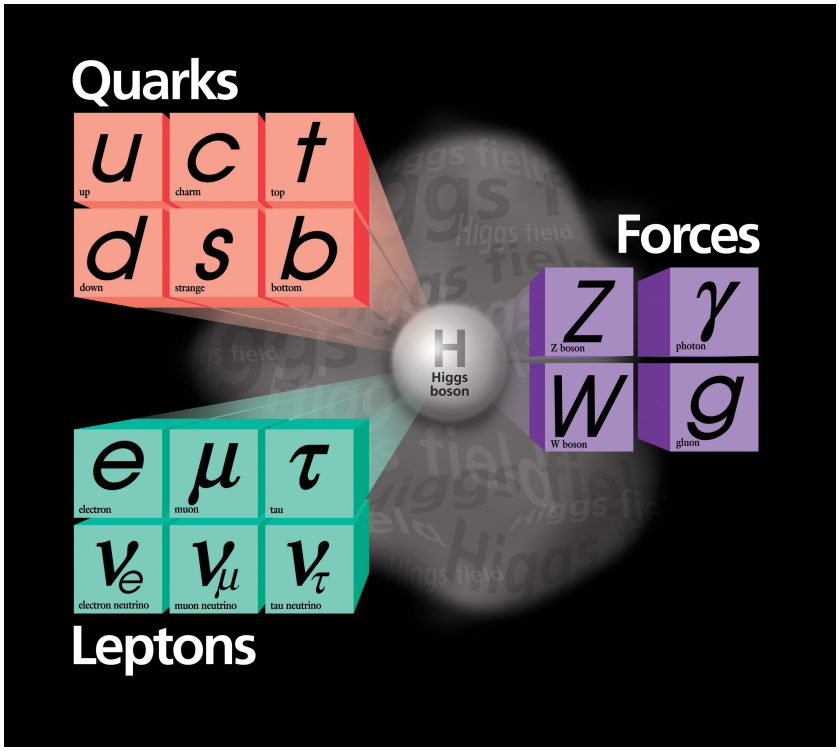

Figure 1.1: The Standard Model of Particle Physics. [1]

and hence generally can interact via weak interaction but do not feel the strong interaction.

The leptons are either electrically charged or uncharged. The charged leptons which are the electron, muon and tau, have an electric charge of $-e$, allowing them to additionally interact via the electromagnetic interactions. The uncharged leptons are the neutrino, muon neutrino and tau neutrino.

According to the standard model every interaction has a mediator with a unit spin. The gluons are the mediators of the strong interaction which acts between particles with color charge. The electromagnetic interaction is mediated by the photon, and acts between particles with electric charge, which are the quarks and the charged leptons. The mediators of the weak interaction are the W^+, W^- and the Z bosons, and they act between particles carrying weak charge.

There is also the Higgs boson which preserves the unitarity of the scattering amplitudes in the standard model. Moreover, elementary particles acquire their masses by interacting with the Higgs field. The Higgs boson is the first discovered elementary particle with zero spin. It was first observed in the Large Hadron Collider in 2012. [2]

1.2 The Strong Interaction

The atomic nucleus consists of protons and neutrons, so the Electromagnetic repulsion force between the protons should cause the nucleus to break apart, however we can find stable nuclei with dozens of protons, which means there must be a stronger force holding them together. This is what we call the Strong Nuclear Force.

The strong interaction acts between particles which have color charge (quarks and gluons, which are collectively referred to as partons), and is responsible for binding them together into Hadrons like the proton and the neutron. In contrast to other interactions, the strength of the strong interaction increases with distance. Due to that unique feature, particles on which the strong force acts on are completely hidden from us. This property is called 'confinement' and it prevents the quarks and gluons from existing freely, instead they have to be bound together in bound states of neutral color charge (baryons and mesons). The confinement feature of the strong interaction makes detecting free quarks much more challenging than in the case of free electrons, which do not feel the strong interaction.

In the standard model, the quantum field theory describing the strong interaction is called Quantum Chromodynamics (QCD).

1.2.1 QCD Running Coupling

According to the quantum field theories, the strength of the forces vary with distances and energies. This variation for the strong interaction is described by the strong coupling constant $\alpha_s(q^2)$.

$\alpha_s(q^2)$ represents the strength of the strong interaction at a certain energy scale q^2. If the coupling constant is known at a certain energy scale μ^2, then its value at any other energy scale q^2 is

$$\alpha_s(q^2) = \frac{\alpha_s(\mu^2)}{1 + \beta\alpha_s(\mu^2) ln(\frac{q^2}{\mu^2})} \tag{1.1}$$

The β-function coefficient can be calculated as

$$\beta = \frac{11N_c - 2N_f}{12\pi} \tag{1.2}$$

where N_c is the number of colors in QCD and N_f is the number of quark flavors [3, p. 258] . For $N_c = 3$ and $N_f \leq 16$, β would be positive which could cause the coupling constant to decrease at higher energy scale.

1.2.2 Asymptotic Freedom

As the energy changes, the value of α_s changes considerably. While at low energies it would have a value of $\mathcal{O}(1)$, at energies greater than $100GeV$, which are achieved at high-energy collider experiments, the value of α_s drops to around 0.1. At such energies quarks are no longer strongly bound together as hadrons and can be treated as quasi-free particles. This asymptotic freedom is a very important property of QCD, and as the energy gets much higher the strong interaction could become negligible as shown in figure 1.2, as

$$\lim_{q^2 \to \infty} \alpha_s(q^2) \to 0 \tag{1.3}$$

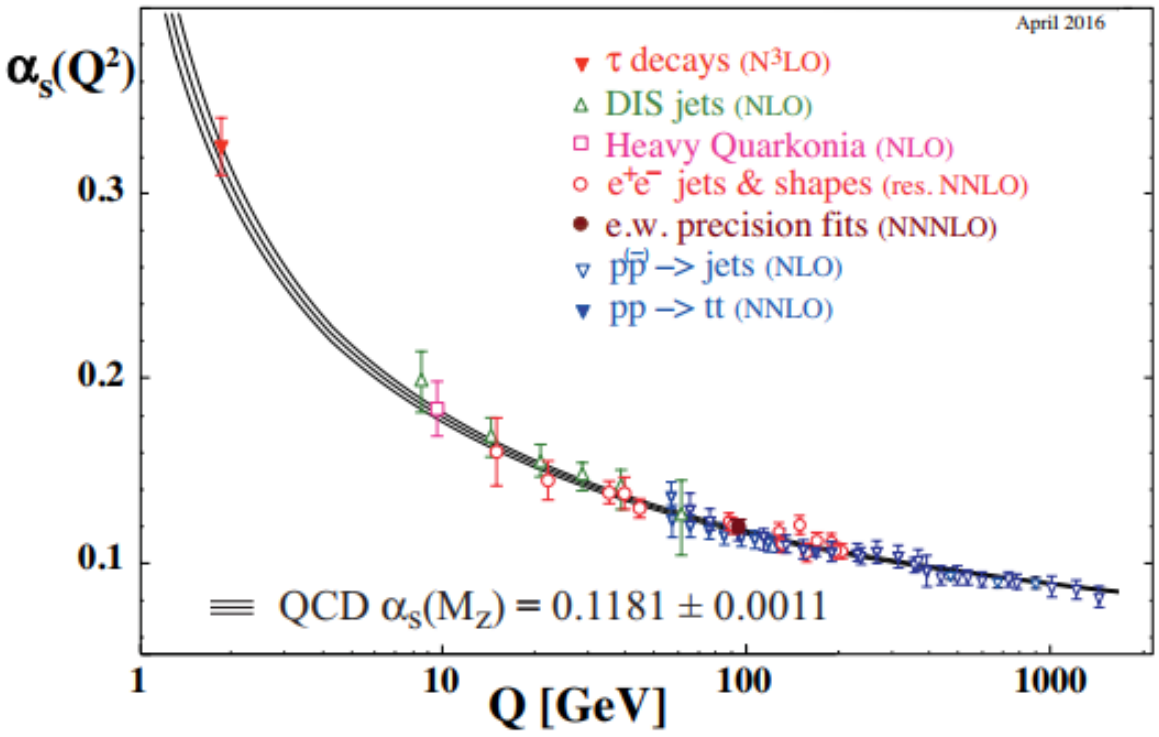

Figure 1.2: Summary of measurements of α_s as a function of the energy scale Q [4].

1.2.3 Confinement

An important property of the strong interaction is color confinement, where color charges cannot be directly observed, only bound-states which have zero net-color charge can be observed as free particles. A cause for that property is the self-interaction of gluons, as they carry color charges themselves.

Two quarks interact with each other by exchanging virtual gluons. These virtual gluons experience attractive interactions between themselves which prevents the color field from spreading out unlike the exchanged photon representing the electromagnetic field. Instead the color field is squeezed into a flux tube which will contain sufficient energy to create a new quark-antiquark pair when the separation between the two original quarks becomes greater than $1fm$ (the confinement scale of the QCD).

This mechanism keeps happening continuously, producing more quark-antiquark pairs until the available energy is no longer sufficient to create new pairs as shown in figure 1.3. At that stage, α_s becomes high enough such that the quark is not free, rather to be bound with other quarks to form hadrons. This process is known in QCD as hadronization and the resulting hadrons are the particles which are identified and whose energies are measured with the detectors. A collection of hadrons originating from the same partons are called a jet.

In terms of forces, the phenomenological potential between two quarks can effectively be expressed as:

$$V(r) \approx -\frac{4\alpha_s}{3r} + kr \tag{1.4}$$

where k is a constant.

As the distance between the quarks increases, the potential between them increases linearly, giving rise to a term in the potential that goes directly with r. On the other hand, as the distance between the quarks decreases, they exhibit a Coulomb-like potential that goes with $1/r$.

Due to the linear term of the potential, at large distances, the quarks would exhibit a constant force between them of $\mathcal{O}(10^5)N$, regardless of the distances between them [3, p. 249]. Consequently, two color-charged particles with a macroscopic distance would have a huge pull towards each other and produce an enormous gluon field. As a result, the gluons arrange themselves into zero net-color particles which exhibit no pull towards each other. As the distance between two individual quarks increases, the potential between them increases, and the stored energy eventually becomes high enough to create a new $q\bar{q}$ pair.

On the other hand, as the distance between the two quarks decreases, α_s decreases more rapidly than r and it should be possible to achieve deconfinement.

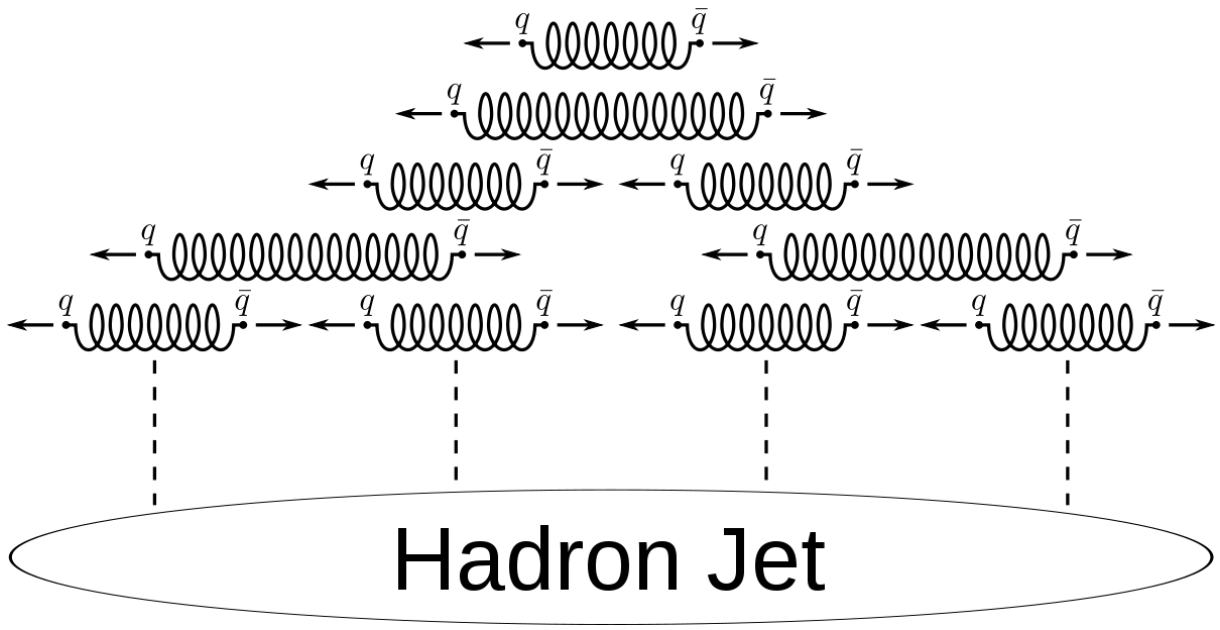

Figure 1.3: The hadronization processes resulting from a quark-antiquark pair. [5]

1.3 Quark-Gluon Plasma and the Early Universe

Shortly after the discovery of asymptotic freedom in 1973 [6] it was suggested that the phase of a freely floating quark and gluon system can be created from nucleus-nucleus collision at high energy. Such system is known as the Quark-Gluon Plasma (QGP). The QGP phase is believed to have existed in the first microsecond after the big bang. As the universe cooled down, the quarks and gluons could no longer remain free and had to form color-neutral hadrons.

In order to study such a state of matter, we try to recreate it by reaching energies and temperatures that probably haven't existed in the universe since the first microseconds after the big bang. Accordingly, certain high energy collider experiments were constructed in order to practically create and study the QGP in the lab.

Chapter 2

Physics of Quark Gluon Plasma

The physics of Quark-Gluon Plasma and its signature are introduces in this chapter. The most relevant phenomena to this analysis, jet quenching, and its current experimental results are shown. Investigating the possibility of QGP formation in the proton-proton collision is proposed towards the end of this chapter.

2.1 From QCD to QGP

2.1.1 Quark Gluon Plasma

It is predicted by QCD that under extreme conditions of high energy and temperatures, baryonic matter would undergo a phase transition from hadronic phase into quark-gluon plasma. At the hadronic phase, quarks and gluons are confined inside hadrons. However as they go through the deconfinement phase transition, the hadrons would fuse together into a larger structure called the QGP where the quarks and gluons are no longer bound to baryons and mesons and can move freely past interbaryonic distances. [7]

There are two methods to cause the hadronic matter to undergo this deconfinement phase transition. The first method is to squeeze the hadrons very close together (high pressure). As the baryonic density increases, the distances between the hadrons become comparable or less than the hadron radius of around $1fm$, and they start overlapping. Individual hadrons are no longer well defined and the quarks and gluons move freely across the new state of QGP.

The second method is to heat up the hadronic matter to extremely high temperatures. As the temperature of the system increases, the added energy not only contributes to kinetic energy of the particles, but causes the creation of new particles. Due to the charge conservation the new particles are created in particle-antiparticle pairs, which increase the number of hadrons in the system, until they fill up the space between them and again the inter-nucleon separation becomes

less than $1fm$ causing the formation of QGP for temperatures higher than some critical temperature ($T \gg T_c$). The value of T_c cannot be calculated analytically using QCD, which is why other numerical methods had to be used.

2.1.2 Lattice QCD

When QCD was developed it was hoped to give many predictions about the internal structures of hadrons and their masses. When a quark-antiquark pairs are created, α_s has a small value and perturbative QCD (pQCD) is sufficient to study their behaviors. However as the distance between them increases, α_s becomes larger where the pQCD technique becomes inapplicable for such calculations.

Hence another numerical technique has been developed to perform such calculations. The Lattice QCD (LQCD) approach was proposed to perform the calculation using computer simulations. Lattice QCD uses a four-dimensional box of points to represent the values of the quark and gluon fields at the lattice points [8]. Using a discrete space-time model causes a cut off for momentum at an order of 1/a (a is the lattice size) which causes the theory to be mathematically well-defined.

A lattice QCD calculation starts by simulating a vacuum state, void of any hadrons, this vacuum state is filled with quarks, antiquarks and gluons continuously being created and destroyed. With these different vacuum configurations, a lot of calculations can be made. For example a quark-antiquark pair can be added to the lattice and their quantum fields can be obtained numerically for each vacuum configuration. The field's variation with time can tell us information about the meson's mass and energy.

The Lattice QCD calculations depend on some parameters which are the quark masses and the value of α_s. These parameters are adjusted within reasonable ranges until the calculated hadron masses from lattice QCD agree with the experiment, and then all the other values obtained would be predictions of LQCD.

In addition to the successful prediction of LQCD for the masses of several hadrons, LQCD predicted the QGP phase transition to occur at a critical temperature of $T_c \approx 170\ MeV$. Indeed, such temperature for the phase transition is consistent with energy required to disassociate the quarks inside the lightest hadrons (pions).

2.1.3 Phase Transition

Figure 2.1 shows the conjectured phase diagram of QCD matter, where μ represents the baryonic chemical potential. Chemical potential represents the imbalance

between quarks and antiquarks, with higher μ meaning a higher quark-antiquark ratio. At low temperatures, where only quarks exist, μ would represent the quark density. [7, 9]

At higher values of quark density (higher μ), the matter moves into a phase of more compressed nuclear matter, eventually transitioning into quark matter. At extreme densities, a color-flavor locked (CFL) phase of color-superconducting quark matter is expected. [10]

In a system where μ is near zero, increasing the temperature would eventually cause a smooth crossover to the QGP phase. At higher temperature, the system would mimic the state of the universe shortly after the big bang.

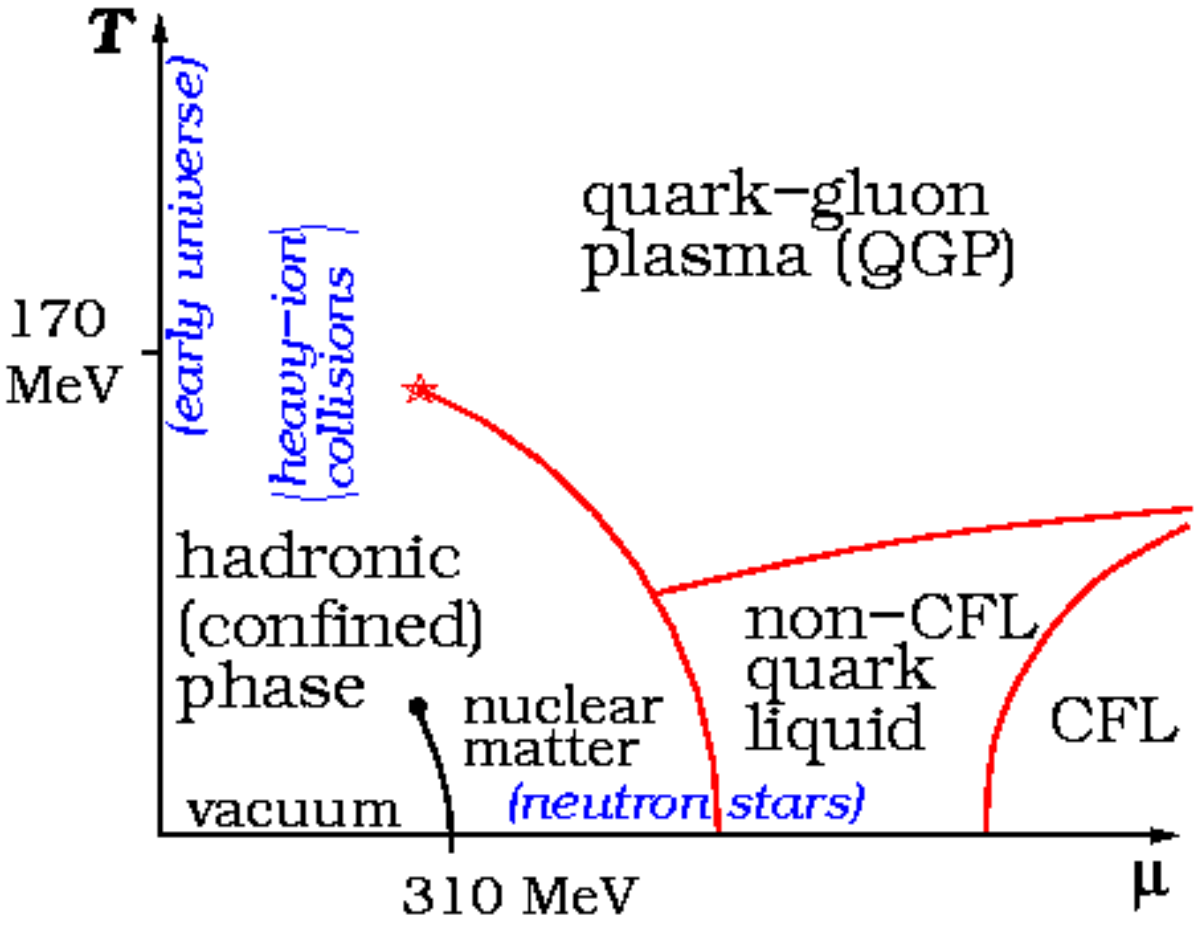

Figure 2.1: QCD Phase Diagram [11]

It is significant to note that the prediction of LQCD for the phase transition to occur at a temperature of $T_c \approx 170\ MeV$ is 6 orders of magnitude higher than temperature of the core of the solar system's sun, which makes it very hard to study QGP experimentally. However the extreme conditions achieved in heavy ion collision provide a rare chance where QGP could possibly be created and studied.

2.2 Quark-Gluon Plasma in the Lab - the "Little" Bang

Due to the previously mentioned facts about the phase transition temperature, it is impossible to form QGP on a lab bench. Therefore the Relativistic Heavy Ion Collider experiments were constructed. Currently, there are two high-energy colliders which are RHIC (Relativistic Heavy Ion Collider at Brookhaven National Lab) and LHC (Large Hadron Collider at CERN) running at center-of-mass energies of up to 200 GeV and 13 TeV respectively. The heavy ions used in these colliders are gold-gold (Au-Au) at RHIC and lead-lead (Pb-Pb) at LHC.

2.2.1 Heavy Ion Collisions

A heavy-ion collision can be classified into different centrality bins according to the value of the impact parameters between the two colliding nuclei. In peripheral collision where the impact parameter has a large value, the number of produced particles is smaller than in central collision where the impact parameter is zero.

In a non-central collision, not the whole nucleus interacts with the other nucleus. Instead, there is an overlapping region between the two nuclei. The nucleons inside the overlapping region are called the participants while the nucleons outside that region are called spectators.

2.2.2 Spacetime Evolution

As the two nuclei collide, the participants interact with each other forming a very hot and dense medium called the fireball. Shortly after the collision, highly excited matter is formed in a pre-equilibrium stage. The partons interact together very strongly and rapidly approach thermal equilibrium. This leads to the formation of QGP where quarks and gluons exist in an equilibrium phase.

As the partonic matter cools and expands, quarks and gluons can no longer remain deconfined and they eventually hadronize after the temperature drops below T_c. With the continuous decrease of temperature, the matter reaches a state where the type of hadrons doesn't change anymore. This is called a chemical freeze-out. The expansion continues until the density becomes low enough that hadrons no longer interact with each other and their momenta would remain unchanged, this transition is known as the kinetic freeze-out. [12, 13]

This whole process is known as spacetime evolution and a schematic is shown in figure 2.2.

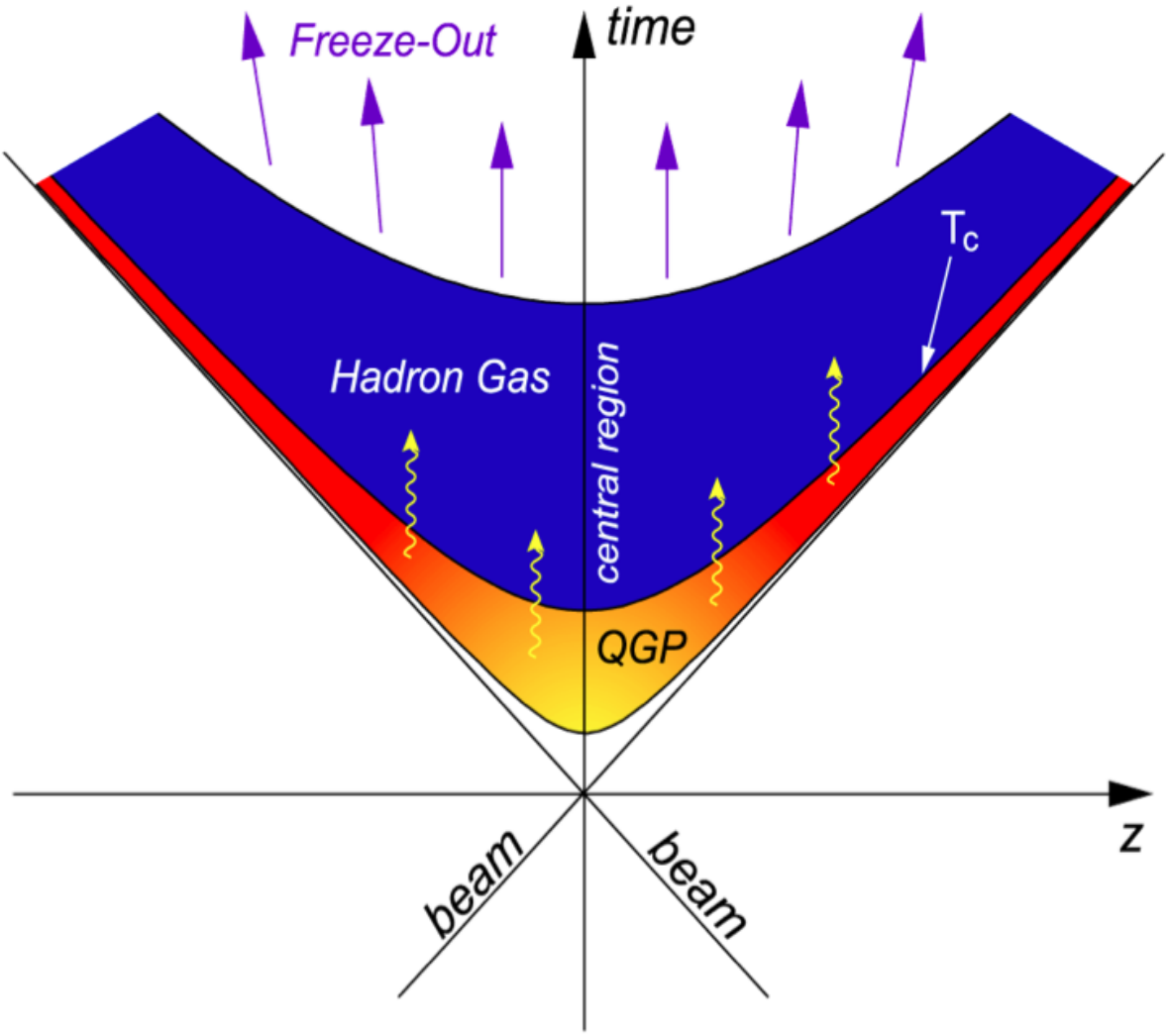

Figure 2.2: Space-time evolution schematic for nucleus-nucleus collision [14]

2.2.3 Collider Kinematics

The momentum components p_x and p_y are unchanged by a boost along z (the beam axis), so the transverse momentum of a particle is defined as

$$p_T \equiv \sqrt{p_x^2 + p_y^2} \tag{2.1}$$

For particles colliding with center-of-mass energy $\sqrt{s}$, the Lorentz invariable quantity x is an important kinematic variable defined as:

$$x = \frac{2p_T}{\sqrt{s}} \tag{2.2}$$

For two colliding particles, the distance perpendicular to the beam axis between them is called the impact parameter b, and the scattering angle θ is the angle by which the particle scatters away as shown in figure 2.3

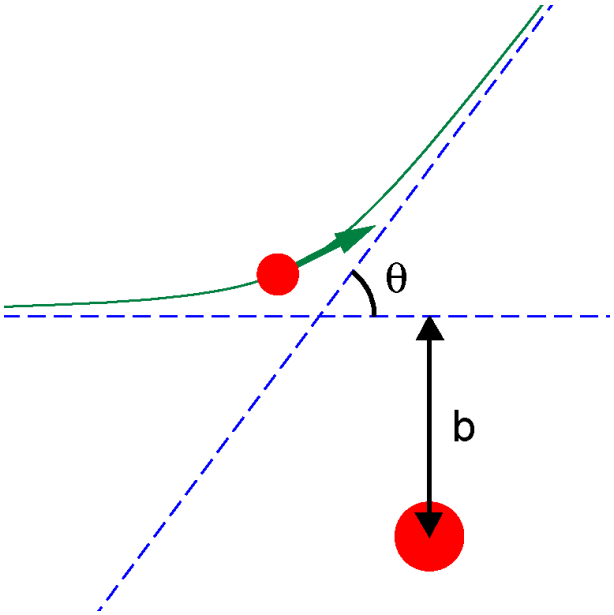

Figure 2.3: A diagram showing the Impact Parameter b and the scattering angle θ, shown in the lab frame. [15]

A convenient way to represent the angle of the particle relative to the beam axis is the pseudorapidity η, which is defined as:

$$\eta \equiv -\ln\left[\tan\left(\frac{\theta}{2}\right)\right] \tag{2.3}$$

A value of $\eta = 0$ represents a particle moving perpendicular to the beam axis.

The azimuthal angle ϕ represents the angle in the plane perpendicular to the beam axis, and it ranges in value from 0 to 2π.

2.3 QGP Signatures

The QGP created in the lab has a fleeting existence that it would exist only for a duration of $5 - 10 fm/c$, which makes the direct search extremely challenging. Among many proposed signatures for QGP such as strangeness enhancement and elliptic flow [16, 17], Jet Quenching is the most important and relevant one to the current study.

2.3.1 Jet Quenching

Jet quenching phenomena represent a parton losing energy while traversing a medium formed out of quarks and gluons. The amount of energy lost will depend on the energy density of the medium and the type of the propagating parton, e.g quarks (heavy and light) and gluons. The gluon will lose more energy than the quark traveling into the same medium due to the fact that the gluon is bicolored. The light quark should lose more energy while traveling the same medium compared to the heavy quark due to the dead-cone effect. [18, 19]

Experimentally the observable that represents the amount of energy lost inside the medium is called the nuclear modification factor (R_{AA}) and is defined by

$$R_{AA} = \frac{dN^h_{AA}}{< N_{coll} >_f \, dN^h_{NN}} \tag{2.4}$$

where dN^h_{AA} and dN^h_{NN} are the differential yields per event for a high-p_T particle h in nucleus-nucleus and nucleon-nucleon collisions respectively, and $< N_{coll} >_f$ represents the number of binary scaling as calculated by optical Glauber Model. [19, 20]

Technically, the single hadron spectra (the number of produced hadrons as a function of transverse momentum) is measured in nucleus-nucleus collisions and compared to that in nucleon-nucleon collisions after considering the number of binary scalings.

2.3.2 Experimental Evidence of Jet Quenching at RHIC and LHC

Many results from RHIC show remarkable evidence of jet quenching. Figures 2.4 and 2.5 shows the R_{AA} of hadrons as a function of the transverse momentum. As it is shown in the figures, the yield in nucleus-nucleus collision is suppressed by a factor of 5 compared to the yield in nucleon-nucleon collisions.

The electromagnetic interacting particles (direct photon) spectra is shown in figure 2.4 and the spectra of the weekly interacting particles (Z^0, $W^{\pm}$) are shown

in figure 2.5. The value of R_{AA} for direct photon is almost consistent with unity reflecting the negligibility of the interaction with the QCD medium.

The 2-particle correlation function in the azimuth direction is also measured at RHIC as shown in figure 2.6. As it is clearly shown, the near-side yield (around $\Delta\phi = 0$) is similar for both systems of collision (nucleus-nucleus and proton-proton collisions). However there is a strong suppression in the away-side (around $\Delta\phi = \pi$) for the nucleus-nucleus collision compared to the proton-proton collision. These results have indicated the surface bias emission from the overlapping zone of the colliding nuclei which explains the similarity for the near-side yields. The away-side parton travels through the medium losing energy represented as suppression for the peak at $\Delta\phi = \pi$. In order to quantify the suppression, a quantity called I_{AA} is defined as

$$I_{AA}^{near-side} = \frac{Y_{AA}^{near-side}}{Y_{pp}^{near-side}} \tag{2.5}$$

and

$$I_{AA}^{away-side} = \frac{Y_{AA}^{away-side}}{Y_{pp}^{away-side}} \tag{2.6}$$

where Y represents the yield of the measured particles.

2.4 Investigation of QGP Formation in Proton-Proton Collisions

The previous results have shown the suppression of hadron (strongly interacting particles) yields at high-p_T (jet quenching) in central AA collisions compared to pp collisions ($R_{AA}^{hadrons}(p_T) < 1$), while the yields of direct photons (electromagnetic interacting particles) and $W^{\pm}$ and Z^0 (weakly interacting particles) have similar values in AA and pp ($R_{AA}(p_T) = 1$). Also the two particles azimuthal correlations results have indicated the suppressions of the recoil jet in AA compared to pp ($I_{AA} < 1$). These results of R_{AA} and I_{AA} have been used to indicate the medium effects (QGP) and hence its formation in central AA collisions.

However, the similar level of yield suppressions of hadrons formed out from light quarks and of hadrons formed out from heavy quarks have raised the question of whether the energy loss takes place before or after the hadronizations stage i.e., whether it is QGP effects or hadronic absorptions [42]. Also the similar medium effect on the recoil jets of hadrons and direct photons (similar I_{AA} as

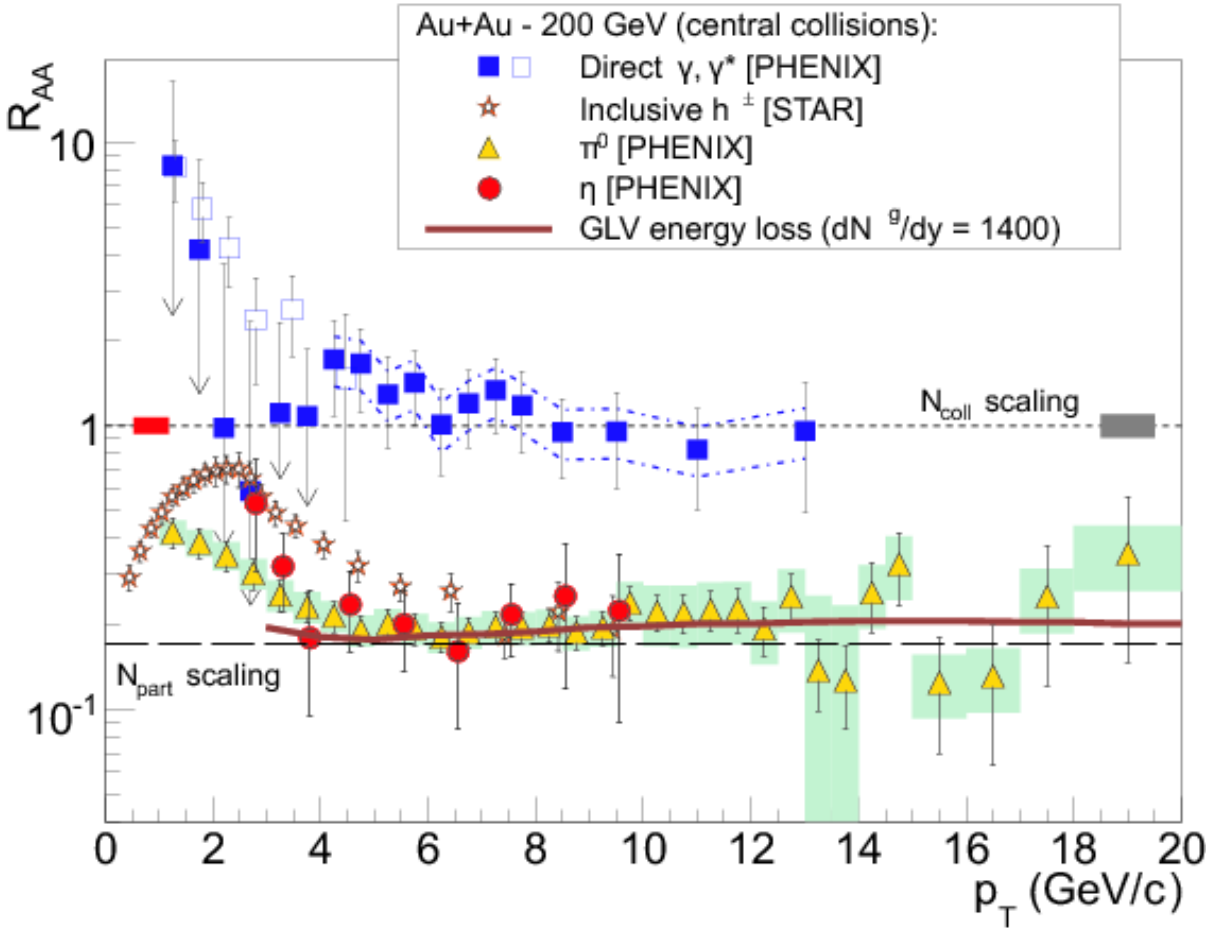

Figure 2.4: $R_{AA}(p_T)$ measured in central Au+Au collisions at $\sqrt{s_{NN}} = 200\ GeV$, taken from ref. [21], for direct photons [22], π^0 [23], η mesons [24] and charged hadrons [25, 26], compared to theoretical predictions [27, 28]

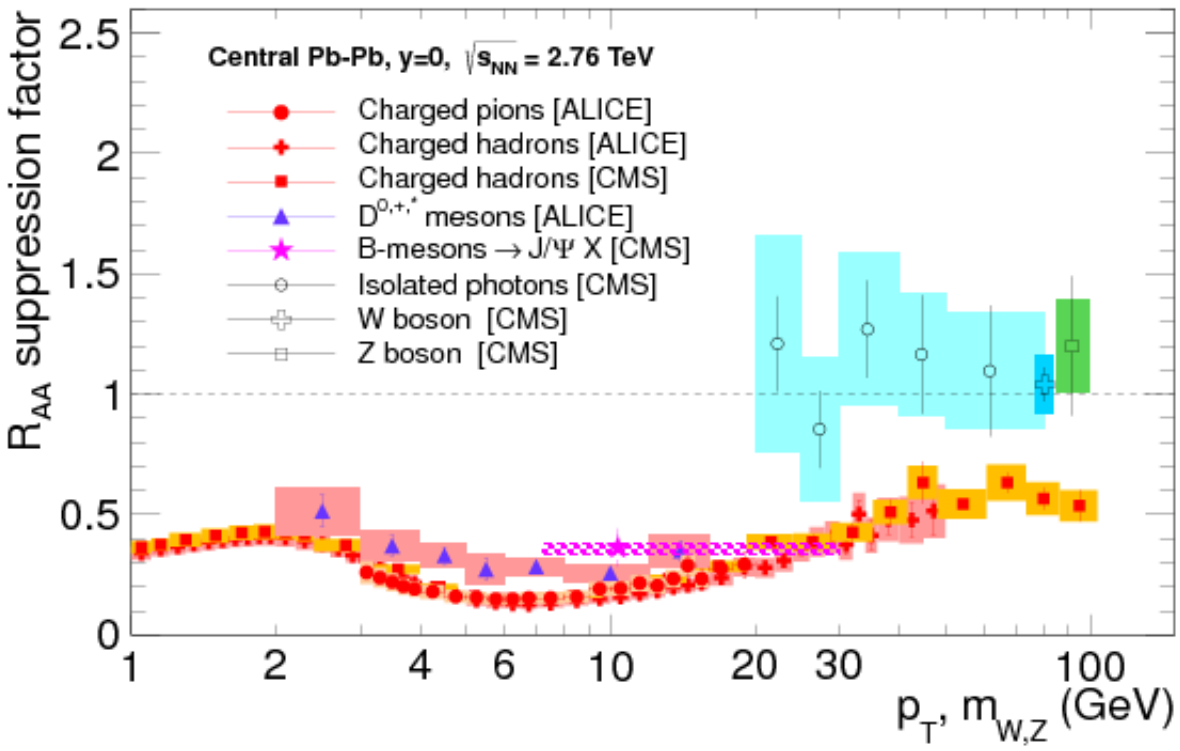

Figure 2.5: $R_{AA}(p_T)$ measured in central Pb+Pb collisions at LHC, taken from ref. [29], for charged hadrons [30, 31], $\pi^{\pm}$ [32], D meson [33], B meson [34], isolated-γ [35], W bosons [36] and Z bosons [37]

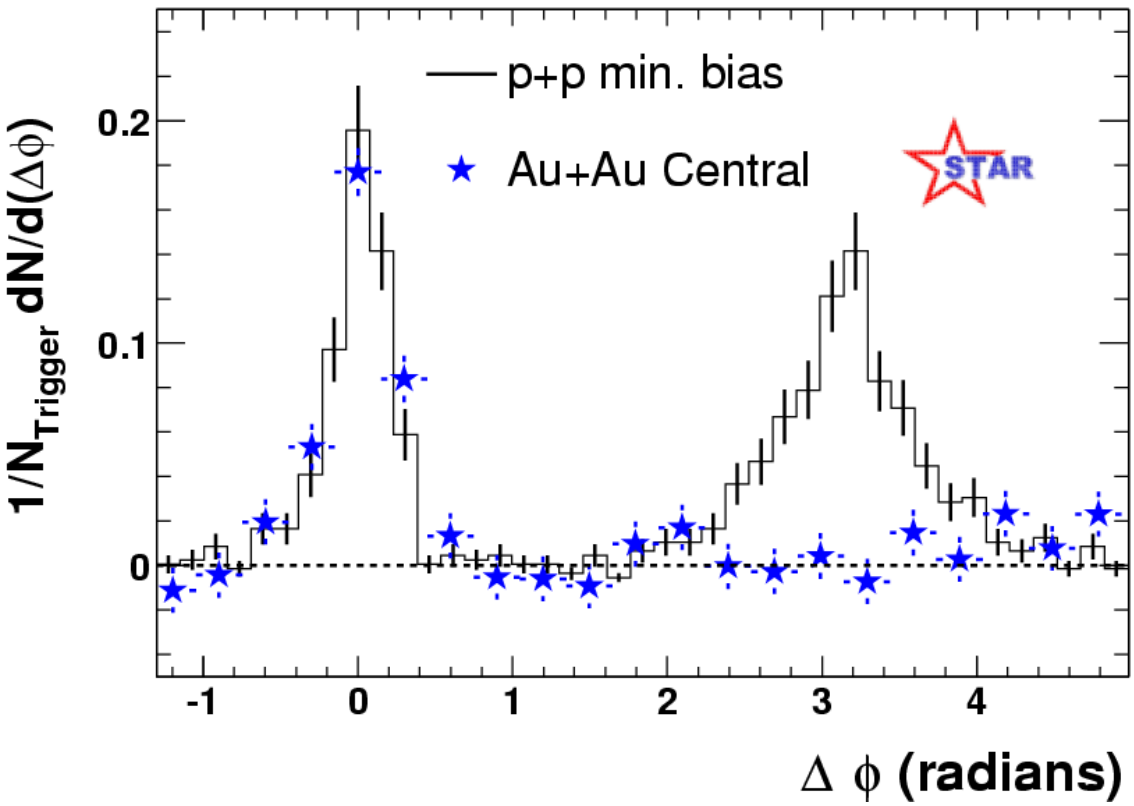

Figure 2.6: Di-hadron azimuthal correlations for p+p and central Au+Au from STAR. [38, 39]

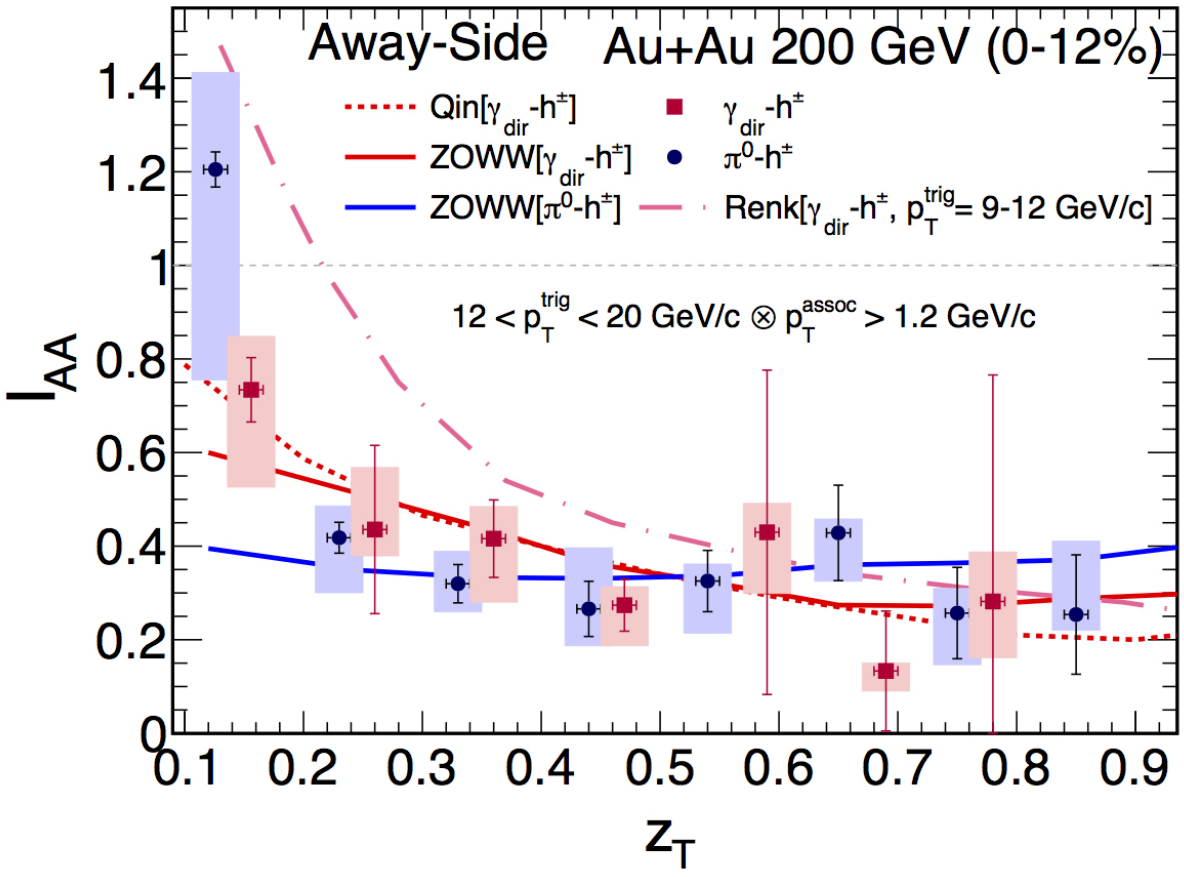

Figure 2.7: The IAA for direct-photon and neutral-pion triggers are plotted as a function of zT. [40]

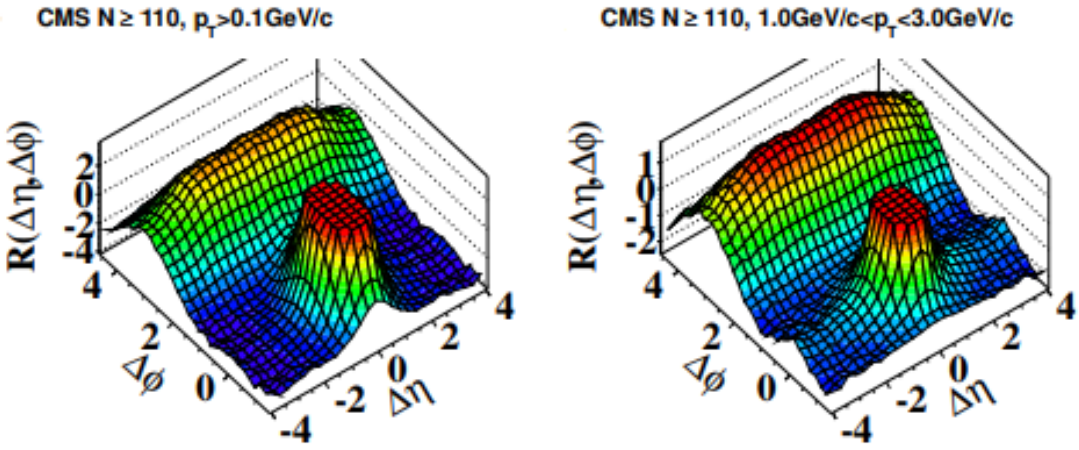

Figure 2.8: 2-D two-particle correlation functions for 7 TeV pp at high multiplicity events with $p_T > 0.1$ GeV/c (left) and $1 < p_T < 3$ GeV/C (right) [41]

shown in figure 2.7) [40, 43], has increased the challenge to constrain the formed medium parameters when compared with the jet quenching theoretical models [44]. Basically, such type of measurements requires very high statistics due to the technical details of subtracting the high level of background in nucleus-nucleus collision.

More recently [41], the two particles pseudorapidity correlations in the events of high multiplicity in pp collisions at LHC (shown in figure 2.8) show long correlations as in central AuAu collisions at RHIC. Then the question that remains to be addressed is whether the jet quenching phenomenon (hadronic yields suppressions) can be reproduced in the high multiplicity events in pp collisions. The two particle azimuthal correlations were proposed in order to search for the possibility of the QGP formation in the high multiplicity event of the pp collision. This analysis uses the PYTHIA simulations at the experimentally available center of mass energy (LHC and RHIC) to search for an answer to such question of medium effects in high multiplicity events of pp collisions using the low multiplicity events of the same colliding system as a reference.

Chapter 3

Analysis and Results

This chapter is dedicated to a detailed description of the analysis towards the final results. The proton-proton collisions were simulated using PYTHIA 8 (version 8.185) [45], with its default parameters, at two values of center of mass energy $\sqrt{s_{_{NN}}} = 200\ GeV$ and $\sqrt{s_{_{NN}}} = 13\ TeV$ corresponding to RHIC and LHC respectively. The center of mass energy is defined as the energy available to create particles.

The events selected for this work include high transverse momentum particles 'triggers' with $p_T > 3.0\ GeV/c$ that are produced within the kinematic region of pseudorapidity $-2 < \eta < 2$ and full azimuth $-\pi < \Delta\phi < \pi$.

3.1 Quality Assurance of the Accumulated Data

This section contains the basic figures which exhibit the raw data features and patterns in order to prove the quality assurance of the simulated collected data at similar RHIC and LHC energies. All of the following figures were made for the events that include a trigger particle with $p_T > 3\ GeV/c$ produced within the above-mentioned kinematics region of $|\eta| < 2$ and $|\Delta\phi| < \pi$

3.1.1 Multiplicities of Produced and Charged Particles

Figures 3.1 and 3.2 show the frequency distributions of the produced particles per event, i.e., the event multiplicities at RHIC and LHC center of mass energies respectively. The multiplicity is defined as the number of the produced particles per event. As expected, at higher energy more particles are produced according to the availability of phase space. It is worthy to mention that the recorded particles herewith are the stable ones, where the decay mode of PYTHIA was turned on in order to mimic the real data collected and analyzed at the real experiments.

The charged particles were filtered per each event and plotted in Figures 3.3 and 3.4 as well in order to compare with the real data, hence it is easier to detect the charged particles than to detect the neutral ones at the real experiments. The figures show the mean of the charged particles produced in each event is 95 at LHC, while those produced at RHIC is 22. It is noticeable that the number of the charged particles is 50% of the total produced particles in each event at the same energy. Up to the first order approximation, one might consider the pions (π^+,π^-, and π^0) are the major particle species due to their low masses. But due to the short life time of π^0 which decays electromagnetically to two photons, the number of the charged particles are expected to be 50% of the total produced particles.

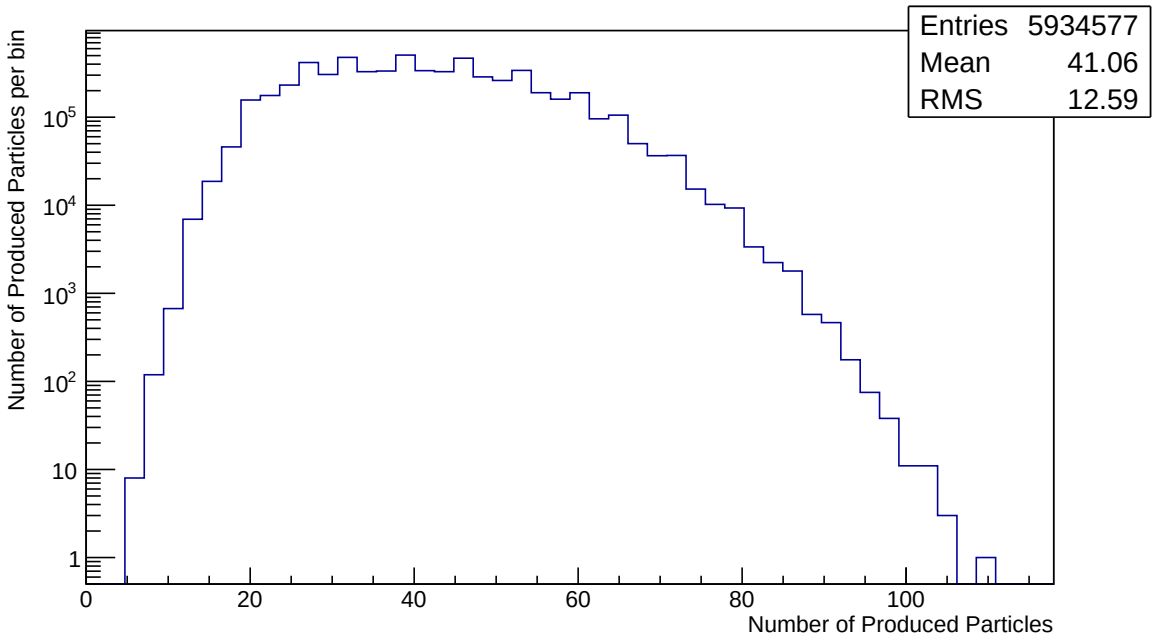

Figure 3.1: A histogram of the multiplicity of produced particles at $\sqrt{s_{NN}} = 200\ GeV$.

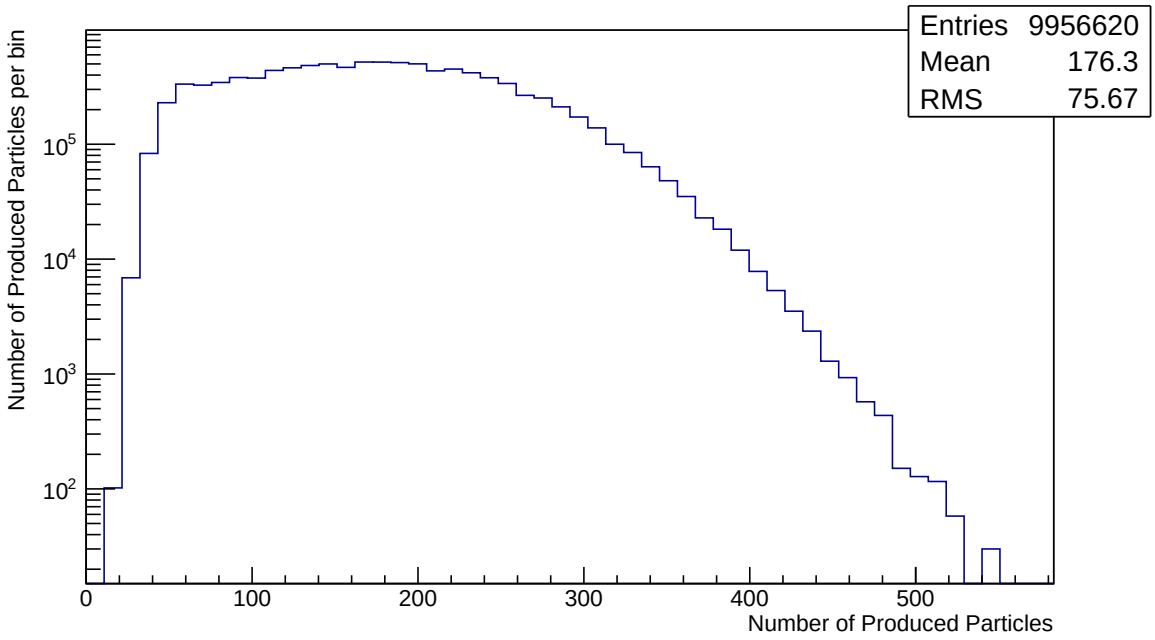

Figure 3.2: A histogram of the multiplicity of produced particles at $\sqrt{s_{NN}} = 13\ TeV$.

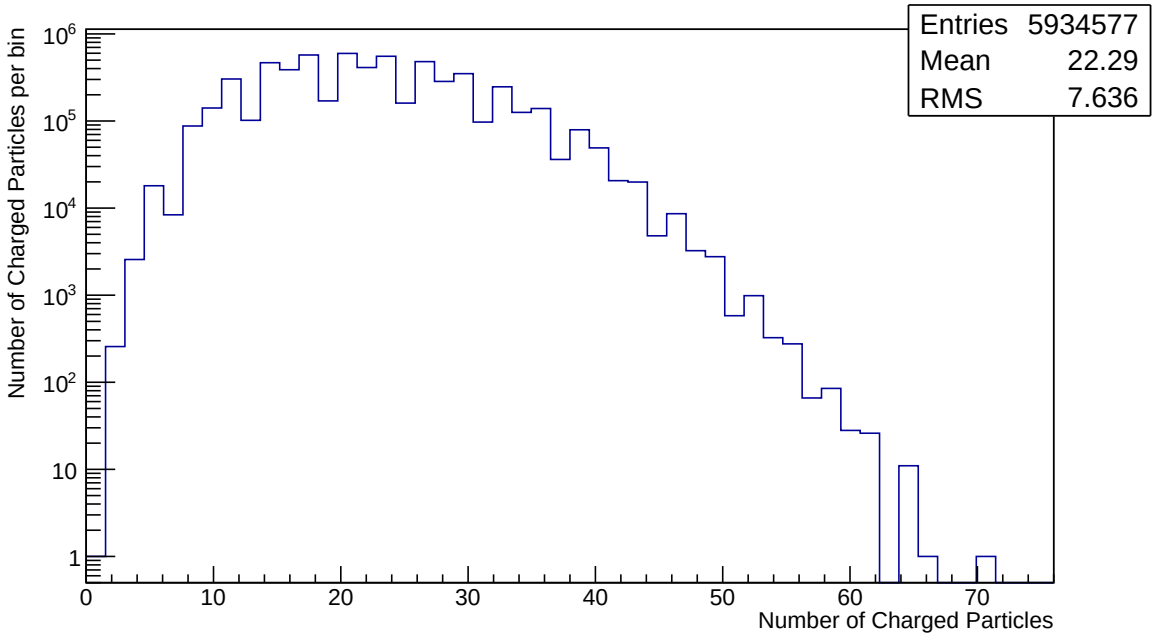

Figure 3.3: A histogram of the multiplicity of charged particles at $\sqrt{s_{NN}} = 200\ GeV$.

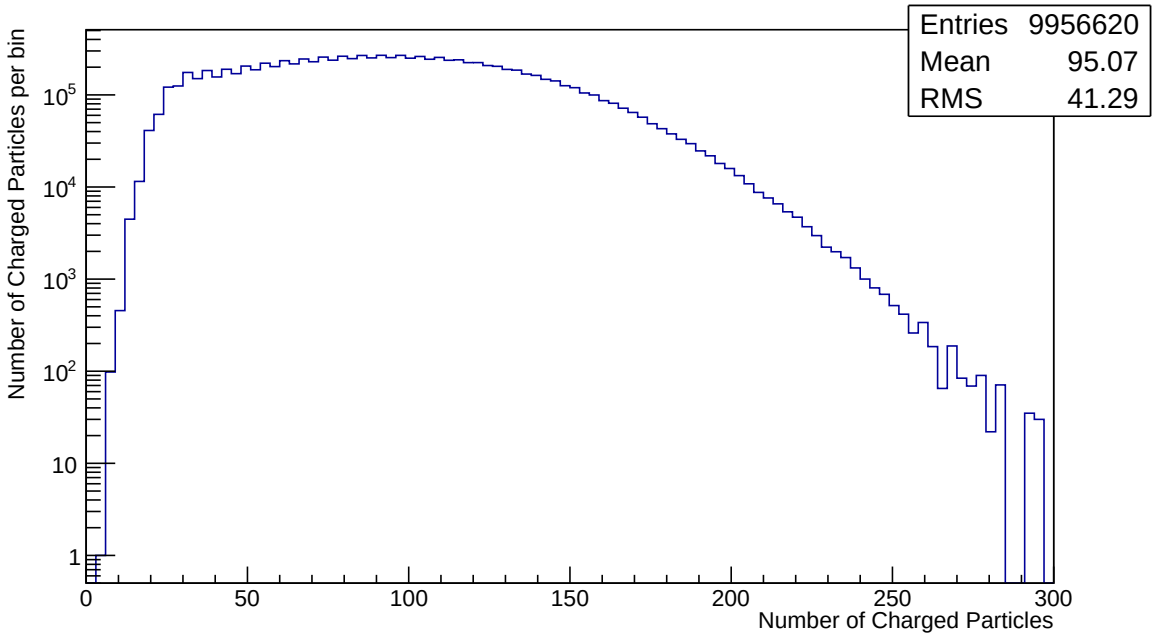

Figure 3.4: A histogram of the multiplicity of charged particles at $\sqrt{s_{NN}} = 13\ TeV$.

3.1.2 Multiplicity of Transverse Momentum Distribution

The following set of figures (3.5 - 3.8) show the number of produced particles (total and charged) per events as a function of the transverse momentum (p_T), i.e., the y-axis in each figure represents the number of produced particles per each p_T bin. The distributions look very similar to the published data of RHIC and LHC experiments [46, 47]. It is obvious from the mean of the transverse momentum that the soft particles (particles with low transverse momentum) are dominating the spectra, where the difference in the mean p_T between the two energies is small. This can be understood as a reflection of the deeply falling spectra of the parton distribution functions of the proton, where the gluons dominate the spectra over the quarks at low Bjorken x. $x_T \approx \frac{2p_T}{\sqrt{s_{NN}}}$. It is also noticeable from the figure that the kinematic reach in p_T is higher at LHC than at RHIC due to higher center of mass energy.

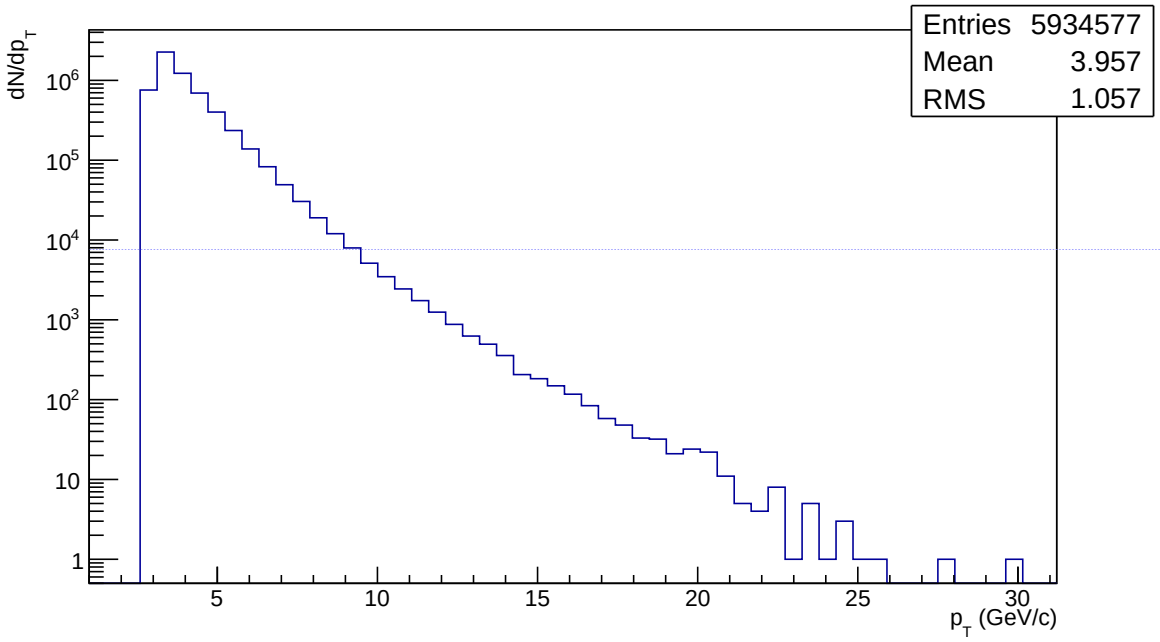

Figure 3.5: A histogram of the multiplicity of transverse momentum distribution of the produced particles at $\sqrt{s_{NN}} = 200\ GeV$.

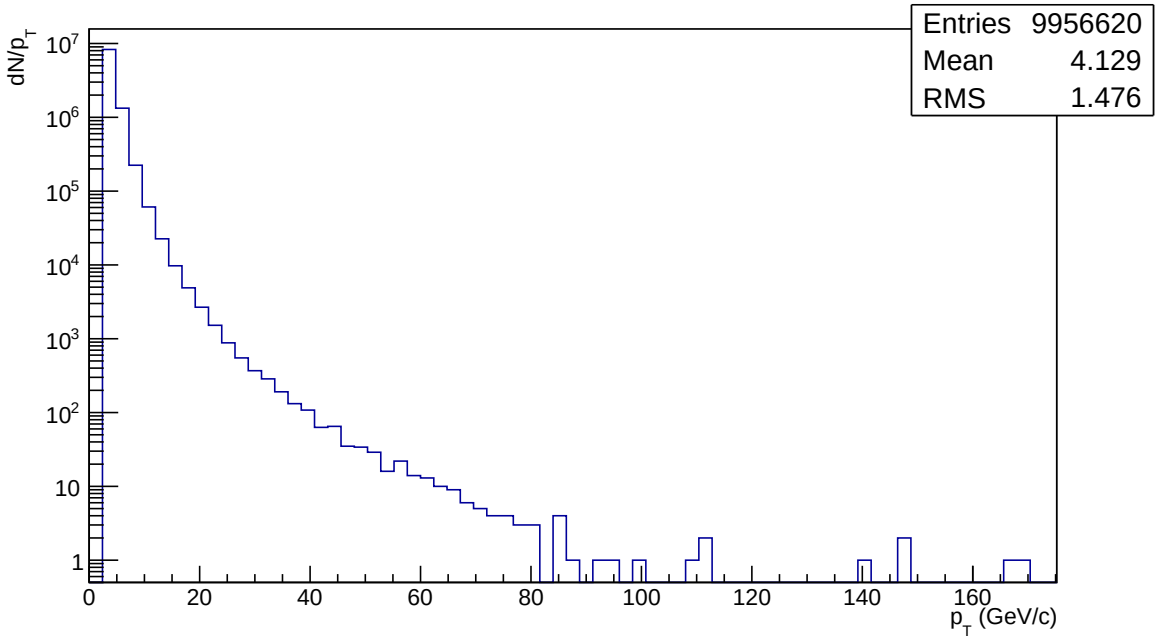

Figure 3.6: A histogram of the multiplicity of transverse momentum distribution of the produced particles at $\sqrt{s_{NN}} = 13\ TeV$.

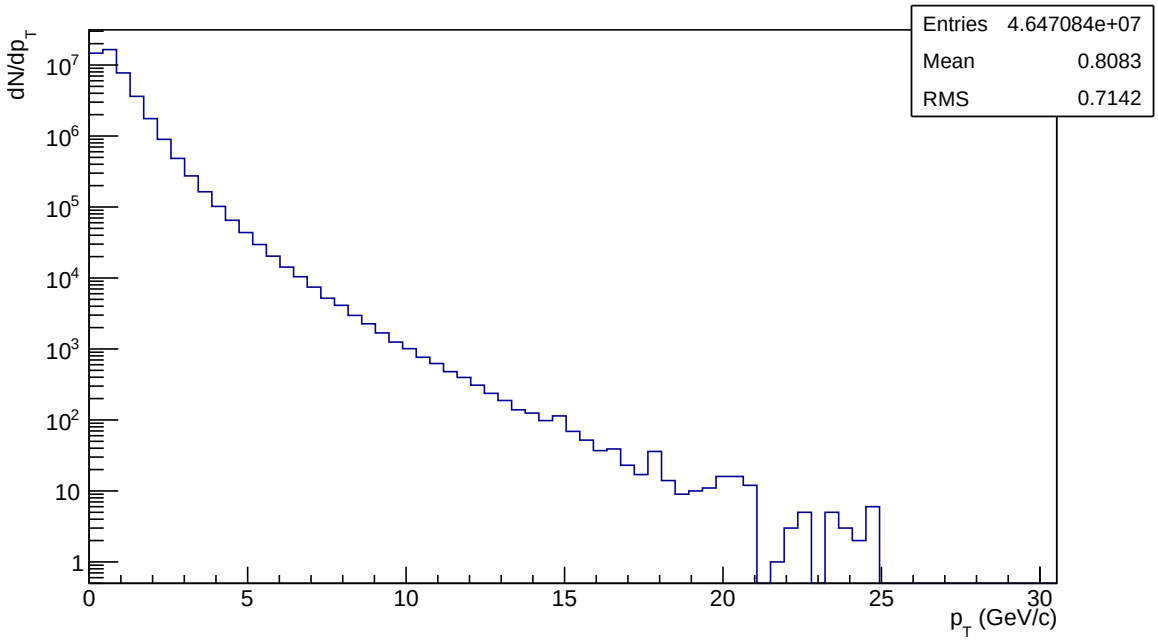

Figure 3.7: A histogram of the multiplicity of transverse momentum distribution of the charged particles at $\sqrt{s_{NN}} = 200\ GeV$.

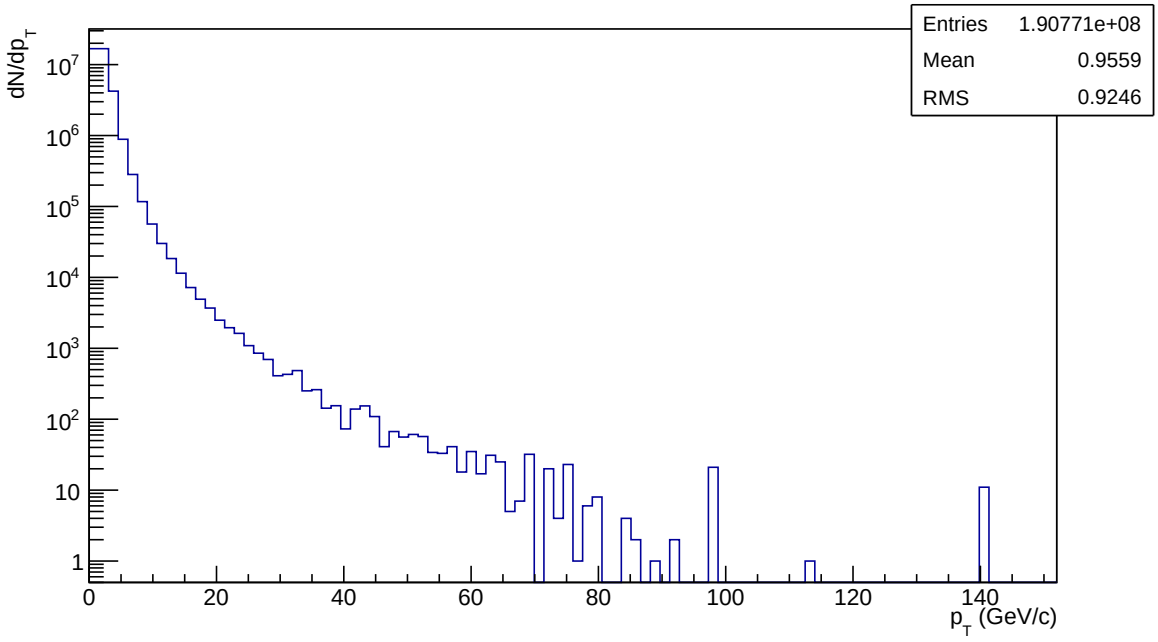

Figure 3.8: A histogram of the multiplicity of transverse momentum distribution of the charged particles at $\sqrt{s_{NN}} = 13\ TeV$.

3.1.3 Multiplicity of Pseudorapidity and Azimuthal Distributions

The pseudorapidity and azimuthal distributions of the produced (total and charged) particles are shown in figures (3.9 - 3.16). The distributions look pretty uniform in the azimuthal directions, and exhibit the p_T imposed criteria on the pseudorapridity distributions. The dip at mid-pseudorapidity of LHC results might be due to the different probed Bjorken x at RHIC and LHC energies. The most important features which is relevant to the current analysis is the uniformity in the azimuthal directions, since the current analysis probes the correlations in the azimuthal directions integrated over the selected pseudorapidity region.

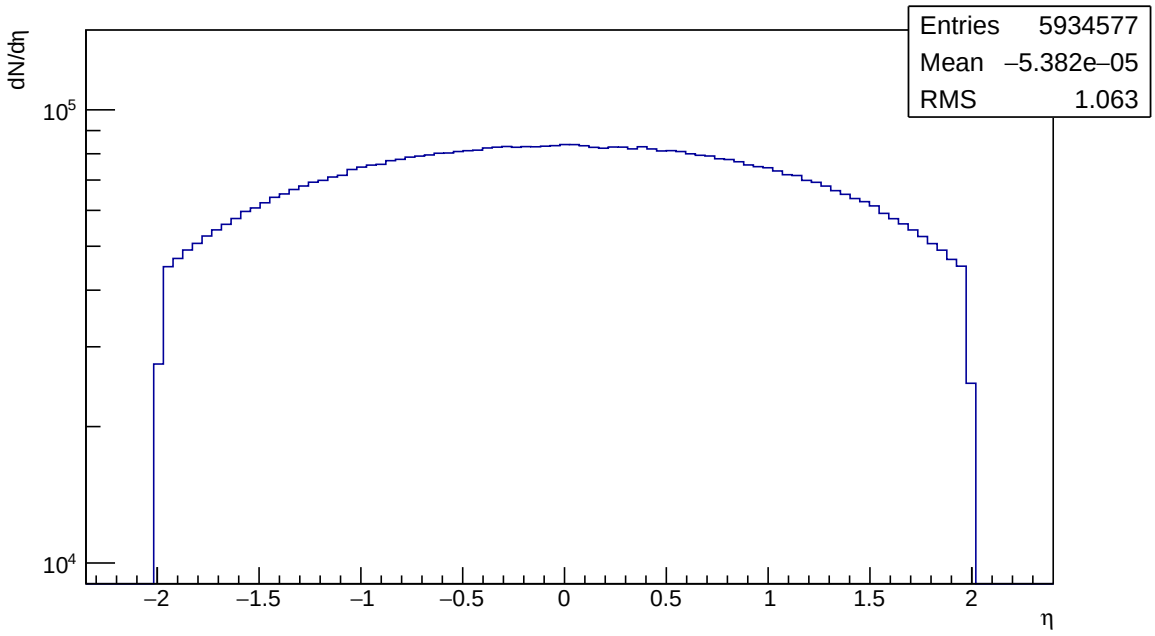

Figure 3.9: A histogram of the multiplicity of pseudorapidity distribution of the produced particles at $\sqrt{s_{_{NN}}} = 200\ GeV$.

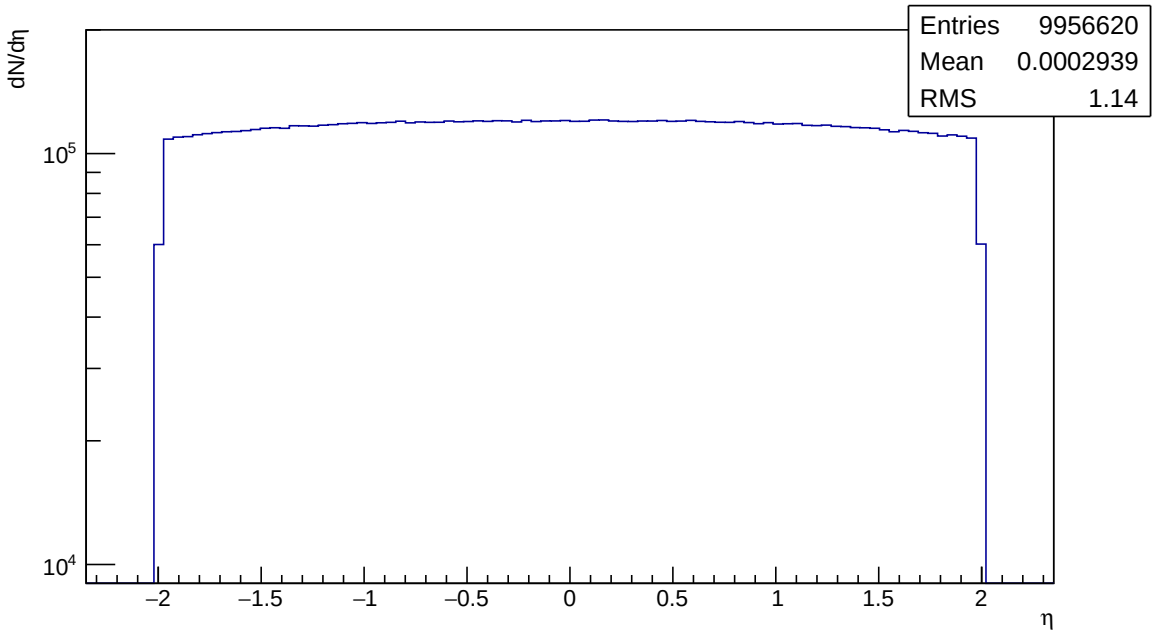

Figure 3.10: A histogram of the multiplicity of pseudorapidity distribution of the produced particles at $\sqrt{s_{NN}} = 13\ TeV$.

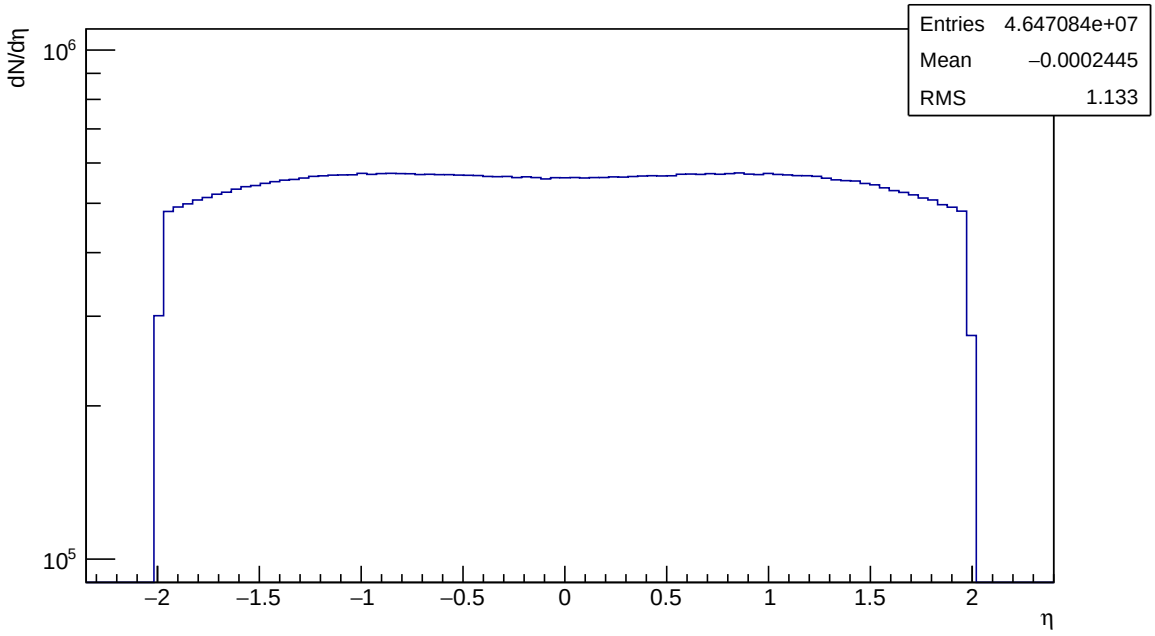

Figure 3.11: A histogram of the multiplicity of pseudorapidity distribution of the charged particles at $\sqrt{s_{NN}} = 200\ GeV$.

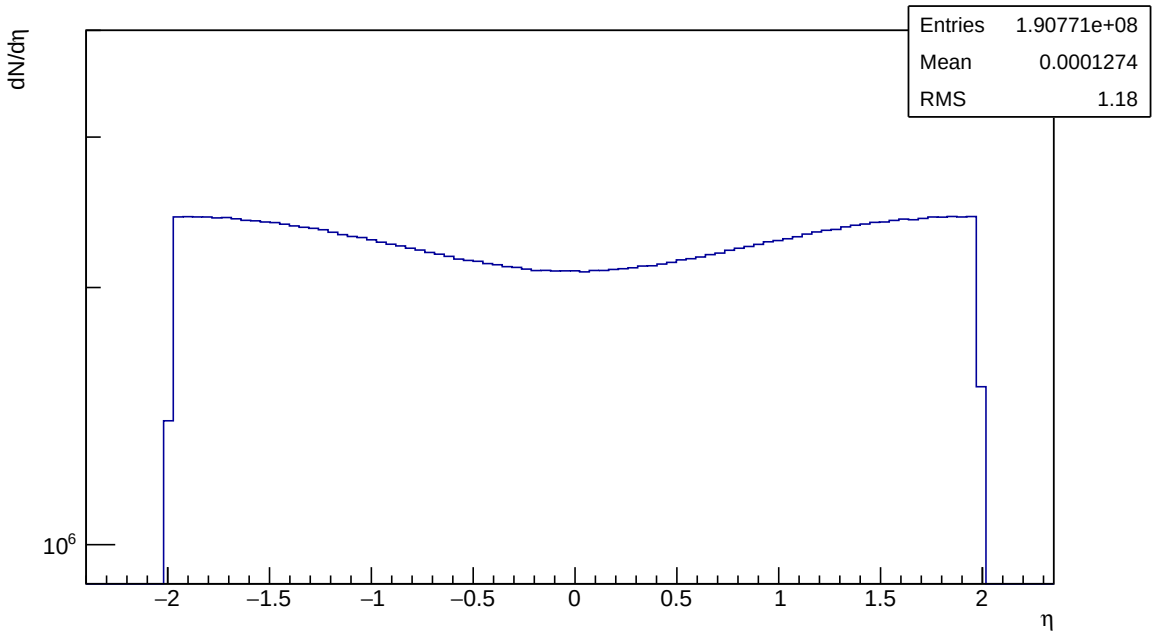

Figure 3.12: A histogram of the multiplicity of pseudorapidity distribution of the charged particles at $\sqrt{s_{NN}} = 13\ TeV$.

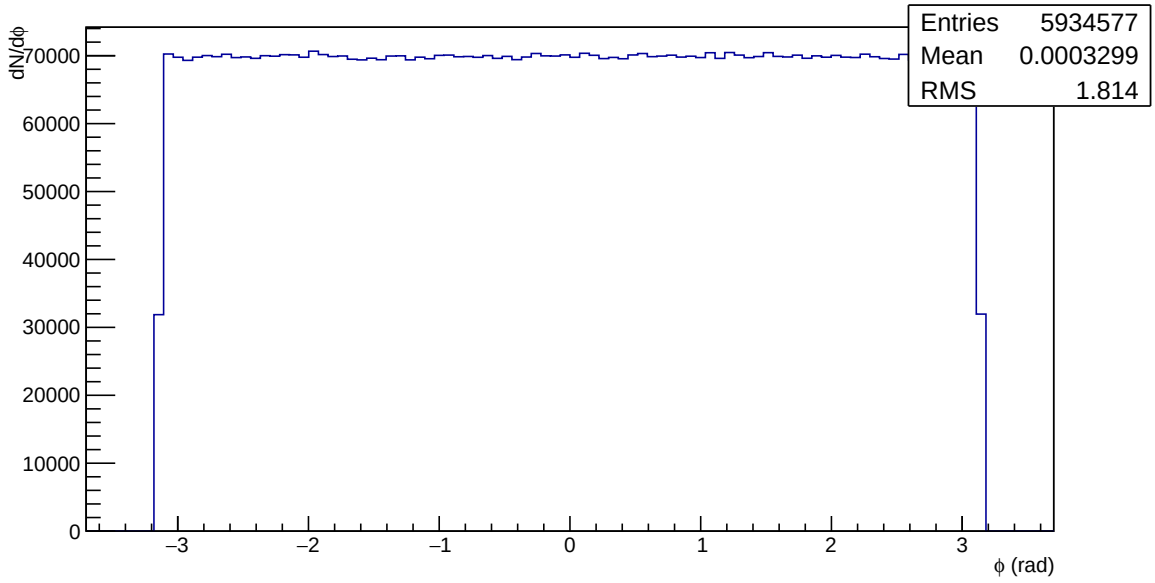

Figure 3.13: A histogram of the multiplicity of azimuthal distribution of the produced particles at $\sqrt{s_{NN}} = 200\ GeV$.

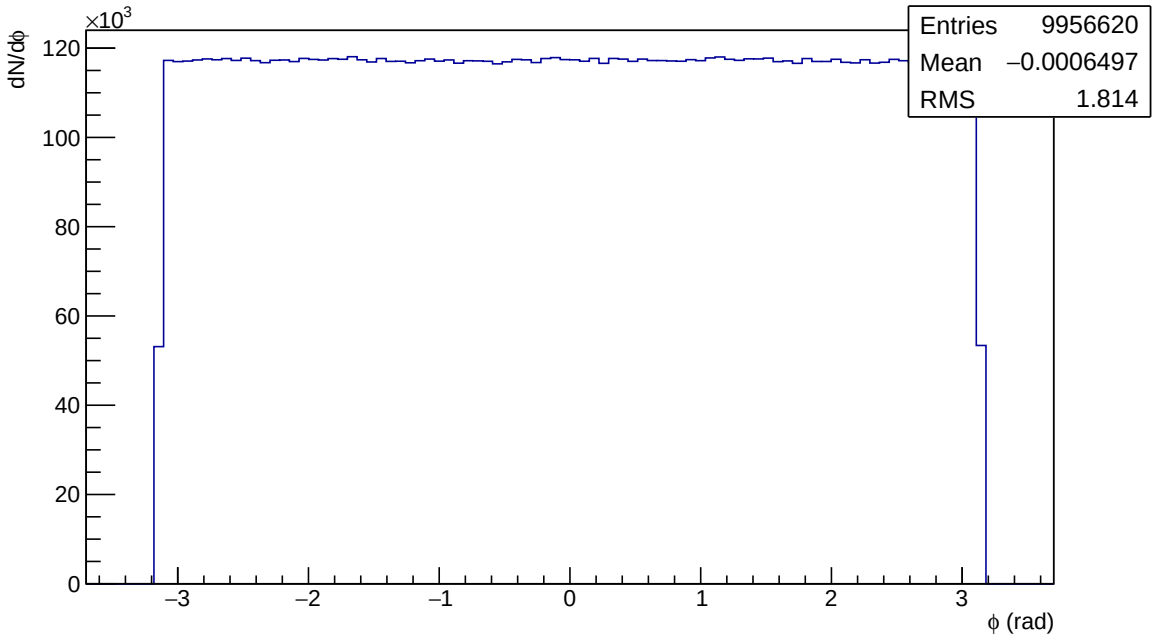

Figure 3.14: A histogram of the multiplicity of azimuthal distribution of the produced particles at $\sqrt{s_{NN}} = 13\ TeV$.

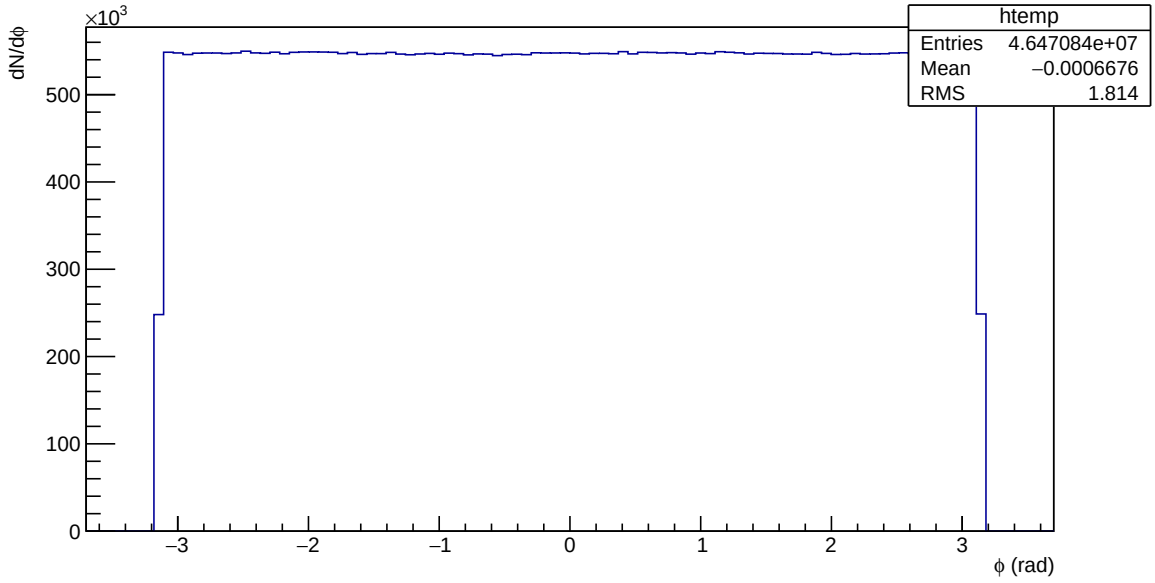

Figure 3.15: A histogram of the multiplicity of azimuthal distribution of the charged particles at $\sqrt{s_{NN}} = 200\ GeV$.

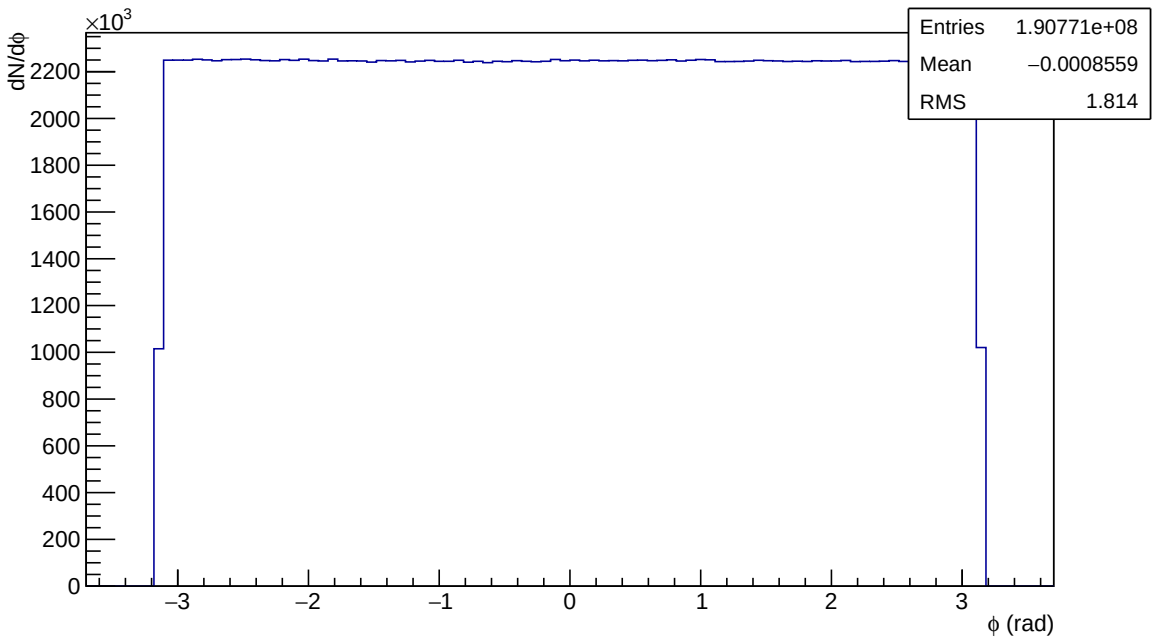

Figure 3.16: A histogram of the multiplicity of azimuthal distribution of the charged particles at $\sqrt{s_{NN}} = 13\ TeV$.

3.2 Two-Particles Azimuthal Correlations

This section includes the details of the analysis in order to extract the yields associated with each trigger particle in different event classes. The event classes refer to the low and high number of produced particles per event. The performed measurements carry the required information about the parton fragmentation function and its evolution for the purpose of the current study.

3.2.1 Azimuthal Correlation Functions

For each one of the produced particles within $|\eta| < 2$ and with transverse momentum $p_T > 3GeV/c$, the difference in azimuthal angle ϕ of this particle (trigger particle) and all other produced particles (associated particles), within $|\eta| < 2$ and with transverse momentum less than trigger particle's transverse momentum ($p_T^{assoc} < p_T^{trg}$) in the same event is calculated and recorded as $\Delta\phi$, where $\Delta\phi = \phi^{trg} - \phi^{assoc}$. As expected from the basic principles of quantum chromodynamics and its confinement features, in each event, few of these associated particles are originated from the same parent parton, and are accordingly correlated, while the rest of the produced particles in the same event are a product of other fragmenting partons. The two particles (trigger and associated) azimuthal correlation

functions are plotted in figures 3.17 and 3.18 for the RHIC and LHC simulated data respectively. The pattern of the two particles azimuthal correlation functions show two peaks around $\Delta\phi = 0$ and around $\Delta\phi = \pi$. The peak around $\Delta\phi = 0$ "near side" results from the strong correlations between the particles produced from the same parent parton. While the "away side" peak around $\Delta\phi = \pi$ is a consequence of the energy-momentum conservations. The other entries in the histogram reflect the complexity of the underlying event in the strong interactions. The level of background "azimuthally uncorrelated particles" is higher at LHC, as shown in the figures, due to a higher available energy used for the particle productions.

The relative strength between the near and away side peaks at RHIC and LHC are different which might reflect the different physics for the underlying mechanism of the produced particles and their transverse momenta.

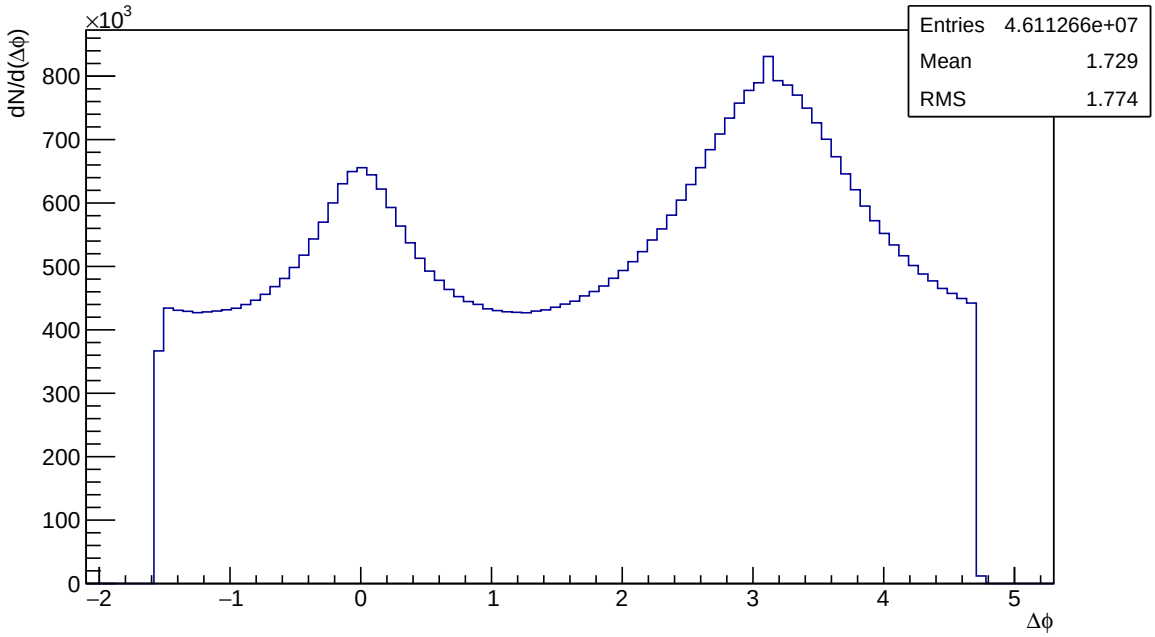

Figure 3.17: A histogram of the multiplicity of the difference in azimuthal angle $\Delta\phi$ at $\sqrt{s_{NN}} = 200$ GeV.

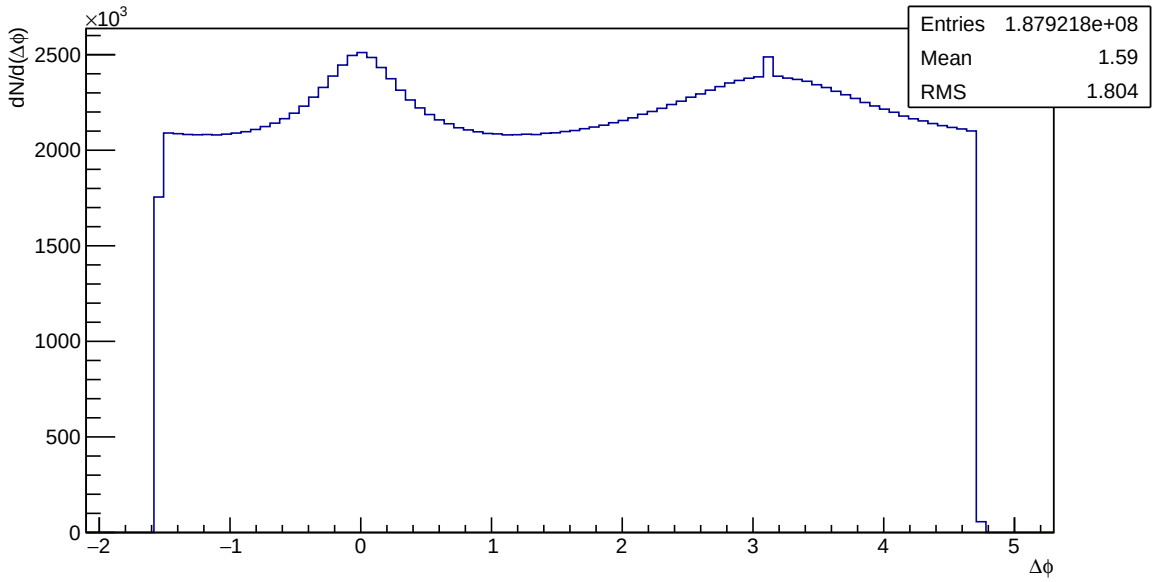

Figure 3.18: A histogram of the multiplicity of the difference in azimuthal angle $\Delta\phi$ at $\sqrt{s_{NN}} = 200$ GeV.

3.2.2 Fragmentation Functions

In order to find how the correlated particles share the total energy of the original parent parton (fragmentation function), each $\Delta\phi$ figure (3.17 and 3.18) is divided into eight different z_T bins at each center-of-mass energy as shown in figures 3.19 to 3.33, where z_T is defined as the ratio between the transverse momenta of the associated particle and the trigger particle.

$$z_T \equiv p_T^{assoc}/p_T^{trig} \tag{3.1}$$

The defined z_T measures the relative energy in terms of the trigger particle, since this analysis doesn't reconstruct the full jet. For the purpose of studying how the fragmentation functions $D(z_T)$ depend on the event multiplicity classes (number of produced particles in each event), the normalized (per number of trigger particles) $\Delta\phi$ figure is made for each z_T bin for 2 multiplicity classes (low and high) at each one of the available center-of-mass energy. The data is also further divided into low multiplicity and high multiplicity events. For RHIC energy, events with $0 < n_{ch} \leq 20$ were considered as low multiplicity, while events with $40 \leq n_{ch} \leq 80$ were considered as high multiplicity. For LHC energy, events with $0 < n_{ch} \leq 20$ were considered as low multiplicity, while runs with $40 \leq n_{ch} \leq 120$ were considered as high multiplicity.

One of the most important features of all correlation functions for each z_T

bins, for low and high multiplicity events at the different center-of-mass energies, is the level of background "uncorrelated particles" are strongly suppressed with increasing the z_T values as expected.

In order to estimate the level of background each correlation function is fitted with two Gaussian peaks and straight line. The fitted fragmentation functions are shown in figures 3.34 to 3.48. The level of background is extracted from the straight line of the fit, and so the fitting failure of the peaks in some figures such as 3.34(c) does not significantly affect the analysis.

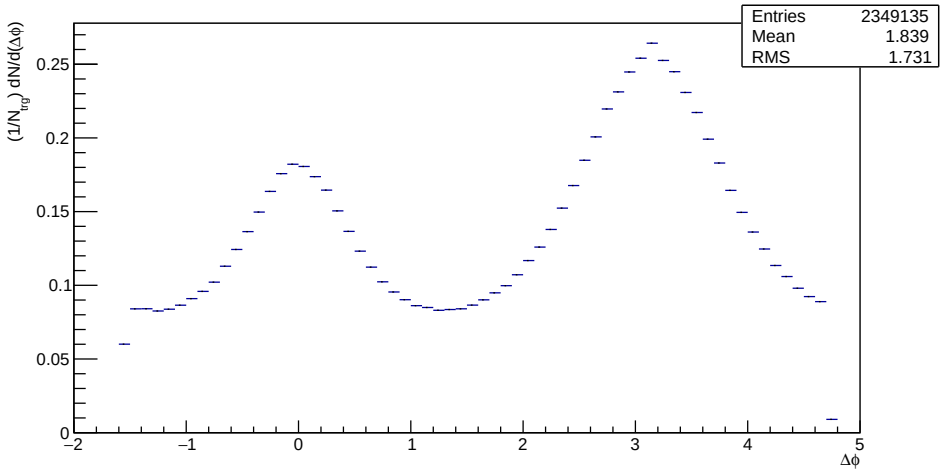

(a) $0.2 < z_T \leq 0.3$

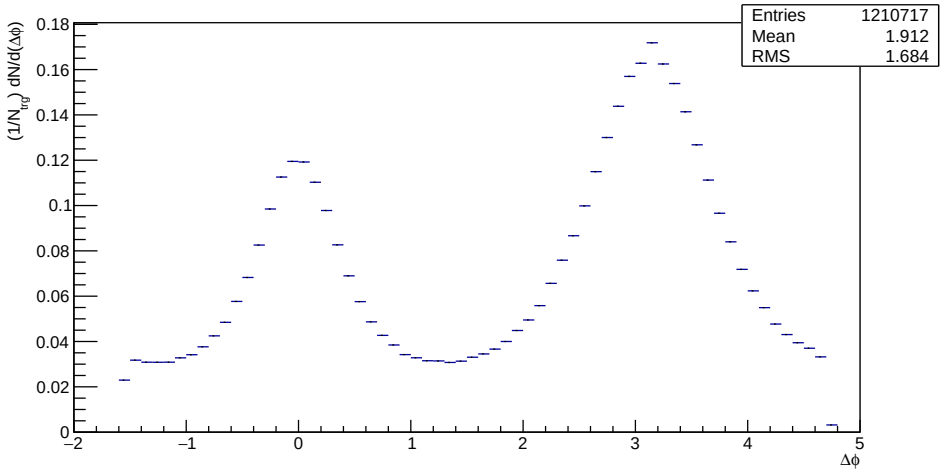

(b) $0.3 < z_T \leq 0.4$

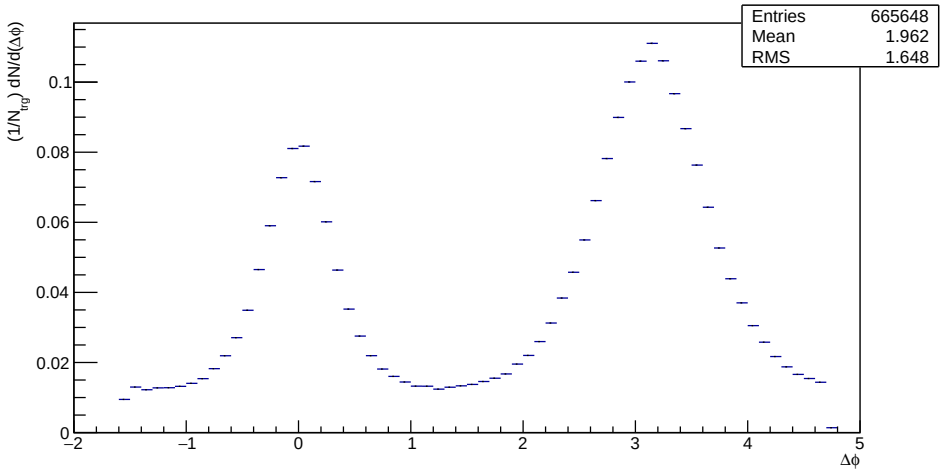

(c) $0.4 < z_T \leq 0.5$

Figure 3.19: A histogram of $\Delta\phi$ for the range $0.2 < z_T \leq 0.5$ at low multiplicity $(0 < N_{ch} \leq 20)$ for $\sqrt{s_{NN}} = 200\ GeV$.

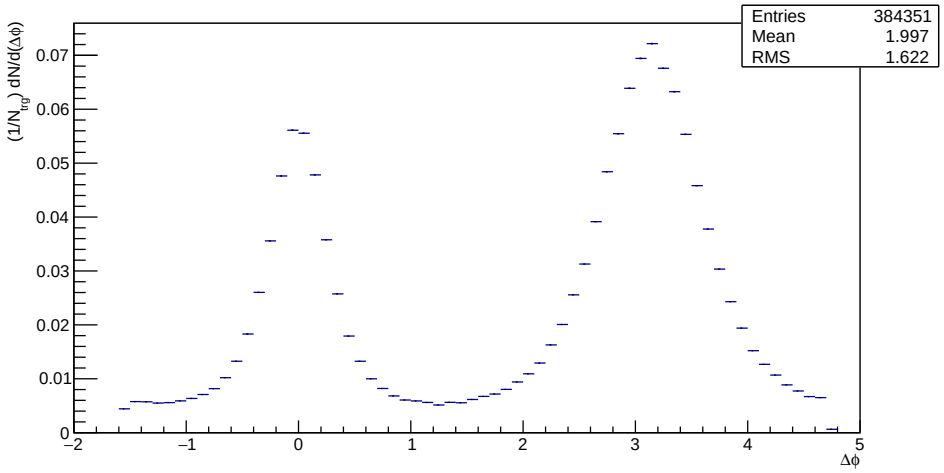

(a) $0.5 < z_T \leq 0.6$

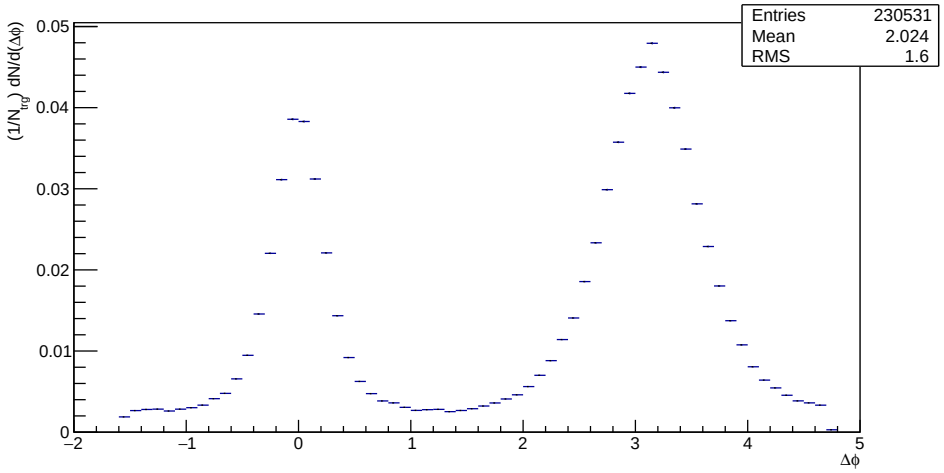

(b) $0.6 < z_T \leq 0.7$

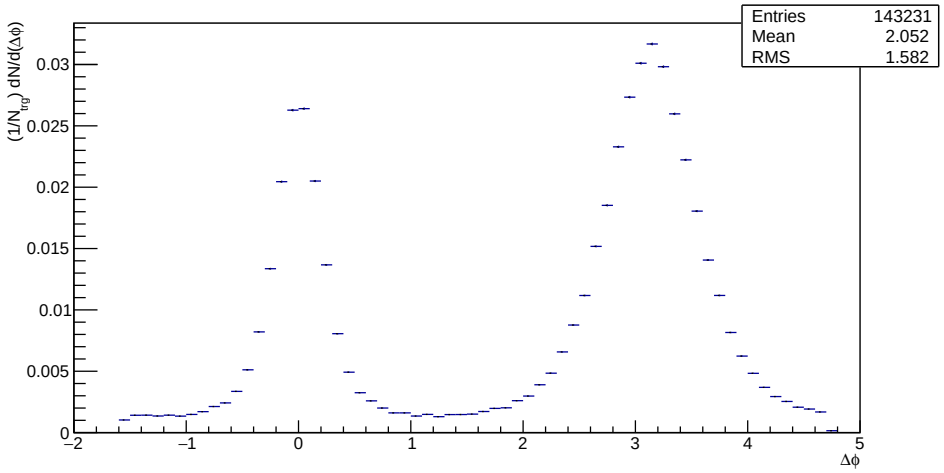

(c) $0.7 < z_T \leq 0.8$

Figure 3.20: A histogram of $\Delta\phi$ for the range $0.5 < z_T \leq 0.8$ at low multiplicity $(0 < N_{ch} \leq 20)$ for $\sqrt{s_{NN}} = 200\ GeV$.

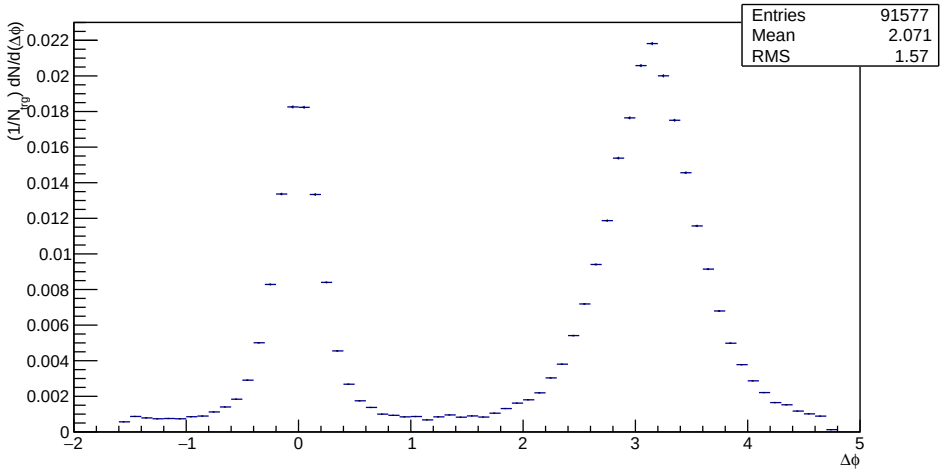

(a) $0.8 < z_T \leq 0.9$

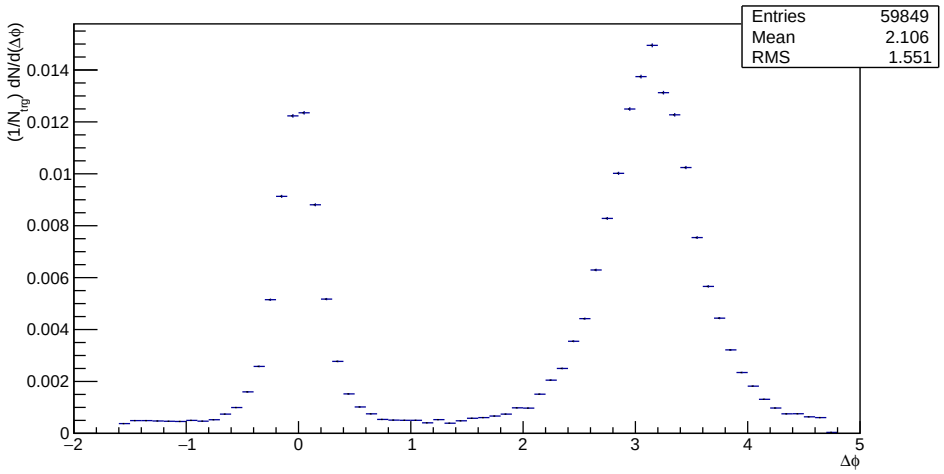

(b) $0.9 < z_T \leq 1.0$

Figure 3.21: A histogram of $\Delta\phi$ for the range $0.8 < z_T \leq 1.0$ at low multiplicity ($0 < N_{ch} \leq 20$) for $\sqrt{s_{NN}} = 200\ GeV$.

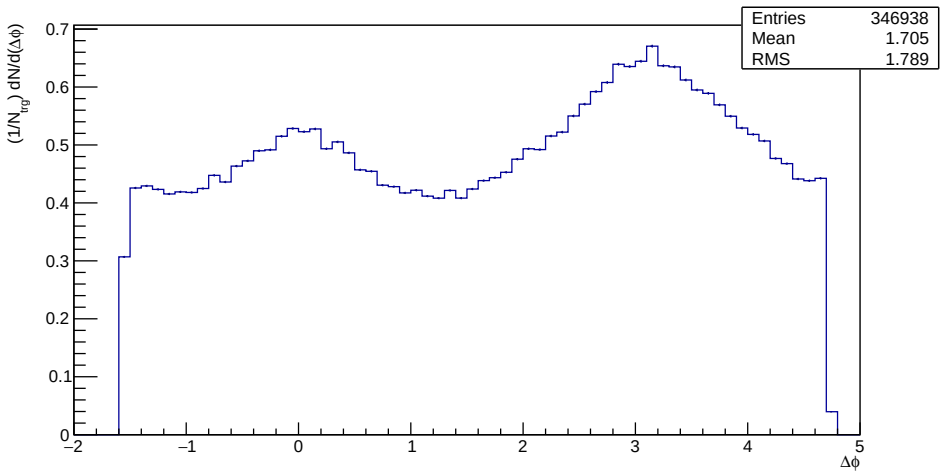

(a) $0.2 < z_T \leq 0.3$

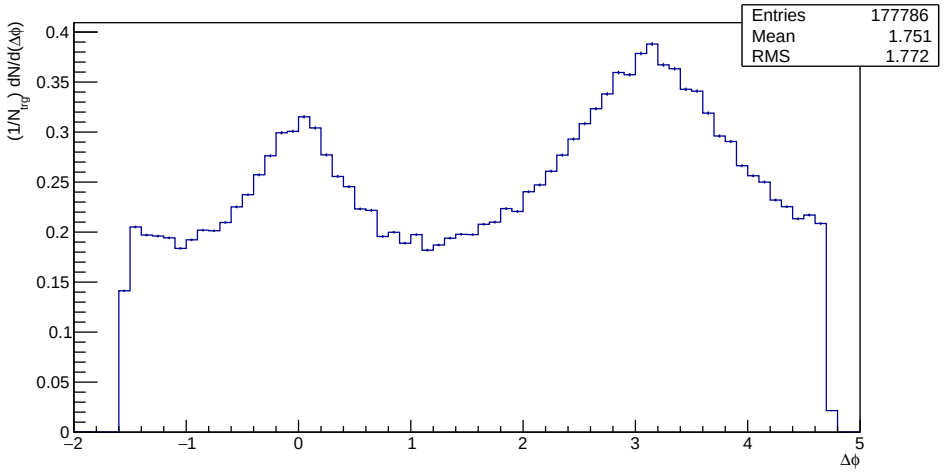

(b) $0.3 < z_T \leq 0.4$

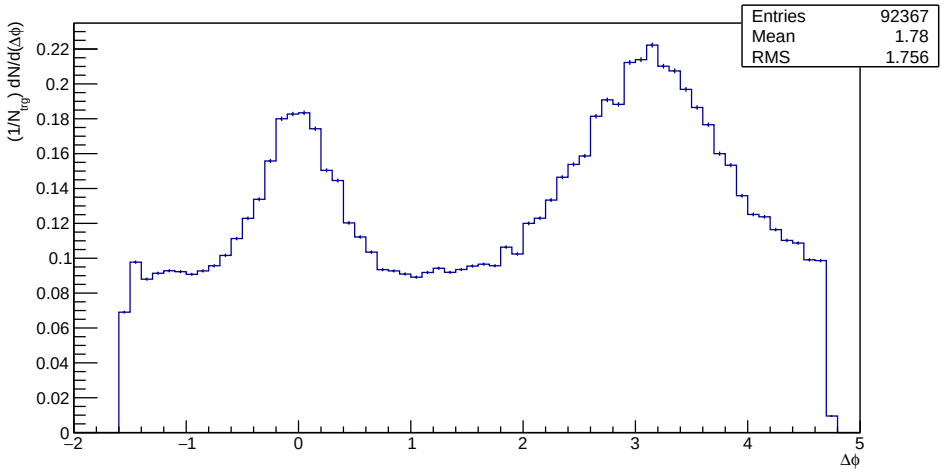

(c) $0.4 < z_T \leq 0.5$

Figure 3.22: A histogram of $\Delta\phi$ for the range $0.2 < z_T \leq 0.5$ at high multiplicity ($40 < N_{ch} \leq 80$) for $\sqrt{s_{NN}} = 200\ GeV$.

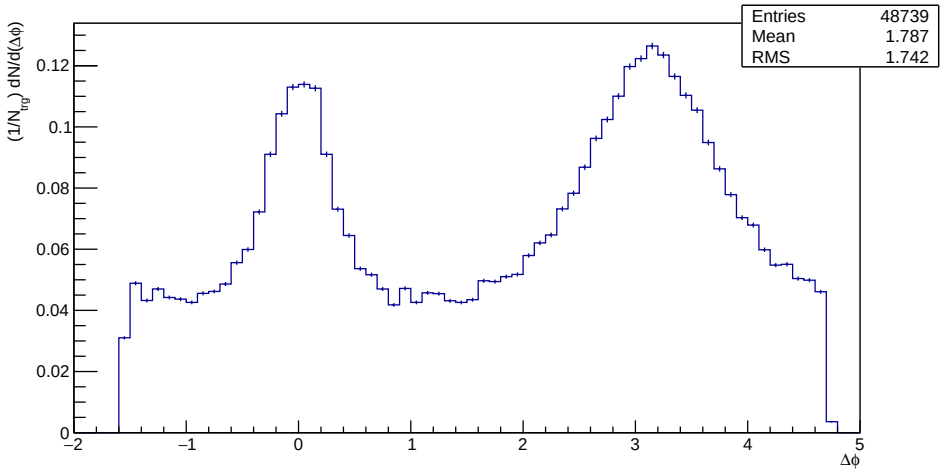

(a) $0.5 < z_T \leq 0.6$

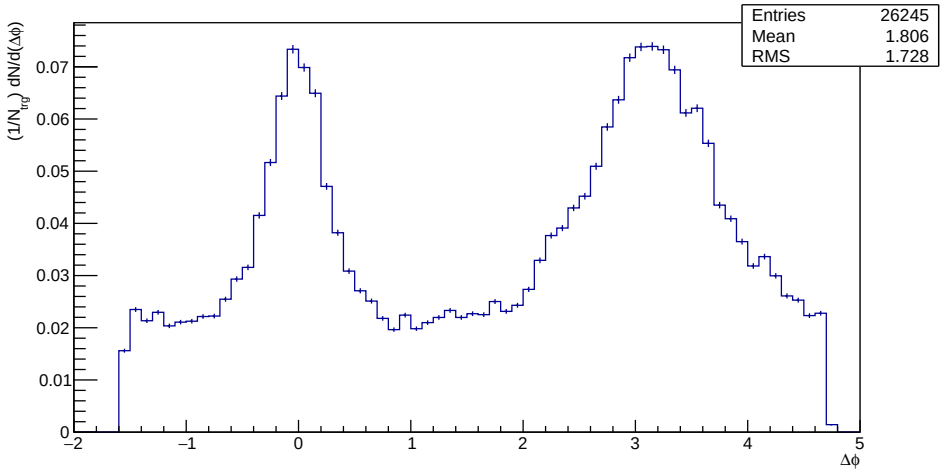

(b) $0.6 < z_T \leq 0.7$

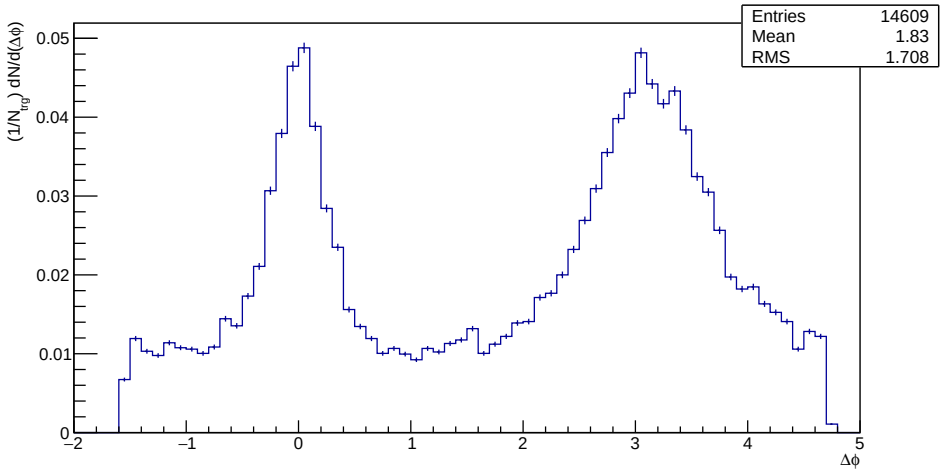

(c) $0.7 < z_T \leq 0.8$

Figure 3.23: A histogram of $\Delta\phi$ for the range $0.5 < z_T \leq 0.8$ at high multiplicity ($40 < N_{ch} \leq 80$) for $\sqrt{s_{NN}} = 200\ GeV$.

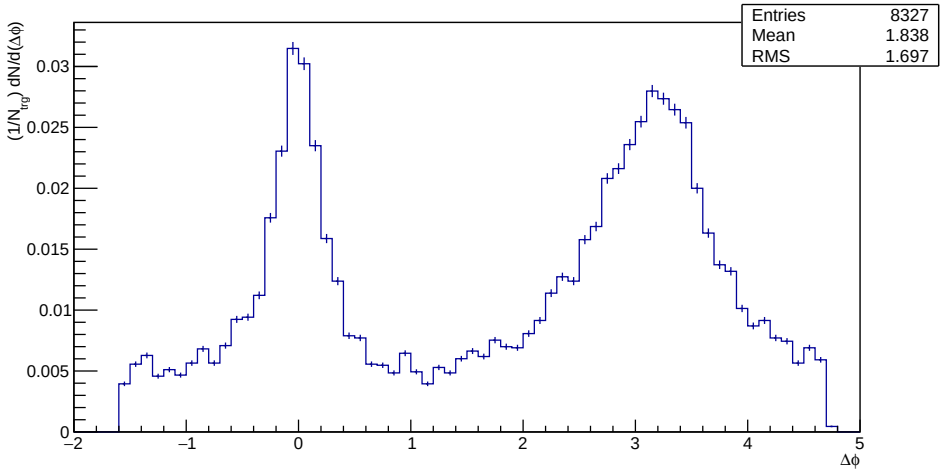

(a) $0.8 < z_T \leq 0.9$

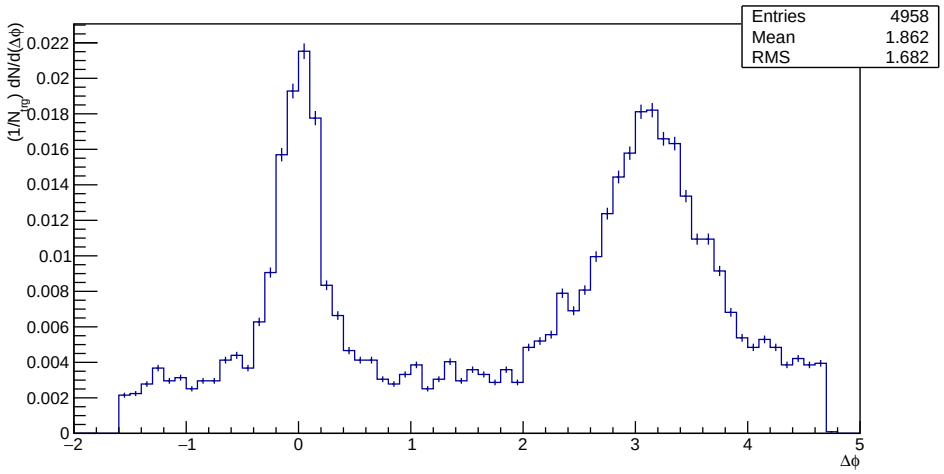

(b) $0.9 < z_T \leq 1.0$

Figure 3.24: A histogram of $\Delta\phi$ for the range $0.8 < z_T \leq 1.0$ at high multiplicity $(40 < N_{ch} \leq 80)$ for $\sqrt{s_{NN}} = 200\ GeV$.

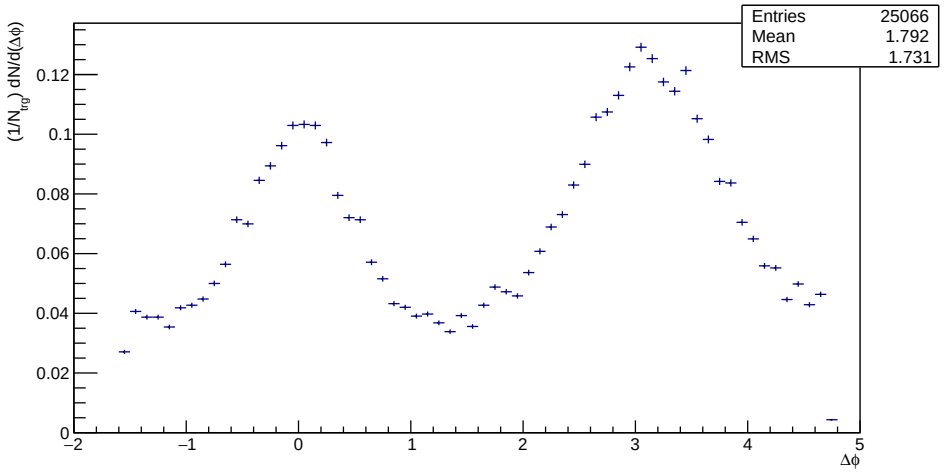

(a) $0.2 < z_T \leq 0.3$

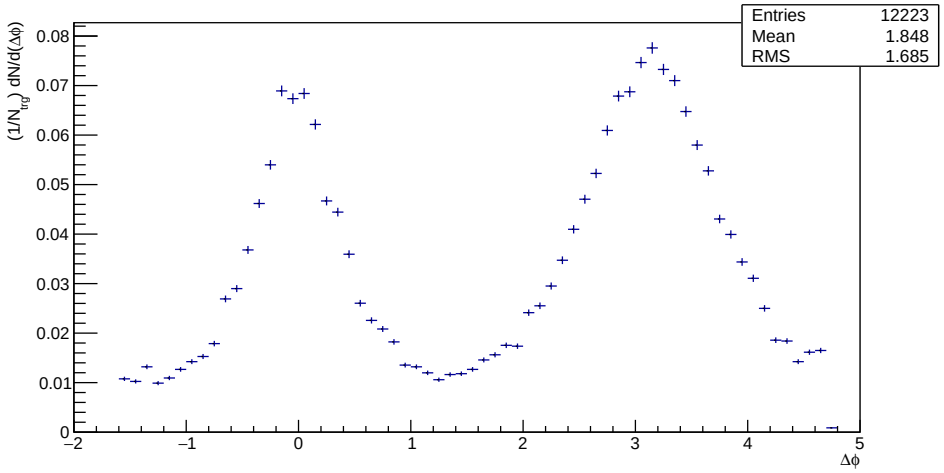

(b) $0.3 < z_T \leq 0.4$

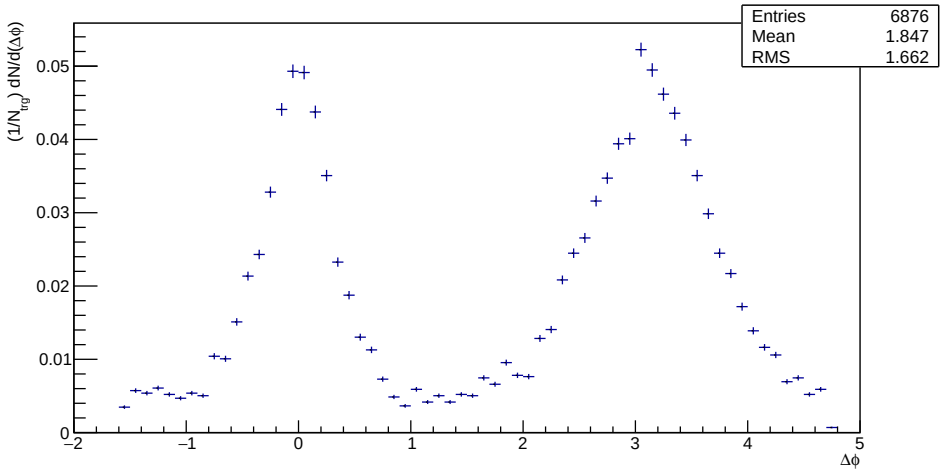

(c) $0.4 < z_T \leq 0.5$

Figure 3.25: A histogram of $\Delta\phi$ for the range $0.2 < z_T \leq 0.5$ at low multiplicity $(0 < N_{ch} \leq 20)$ for $\sqrt{s_{NN}} = 13\ TeV$.

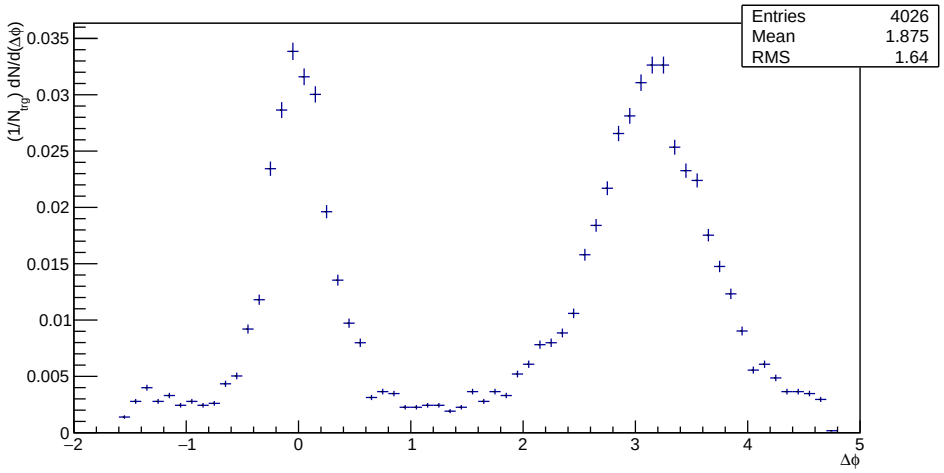

(a) $0.5 < z_T \leq 0.6$

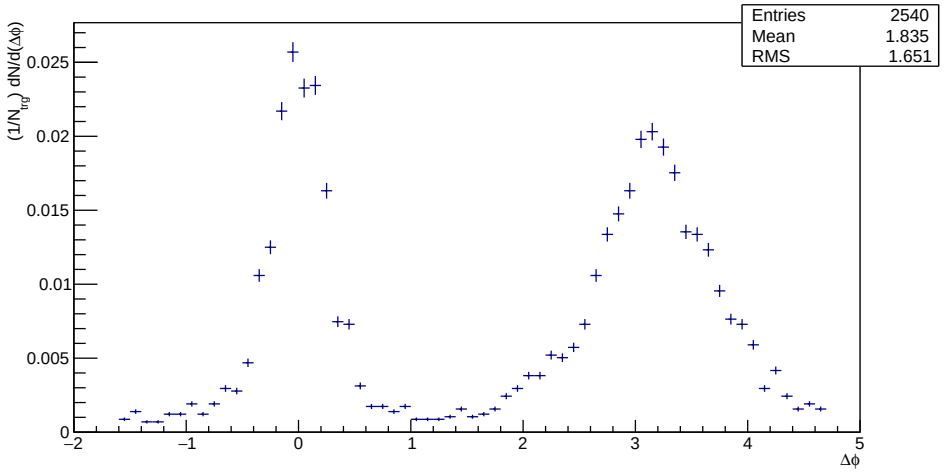

(b) $0.6 < z_T \leq 0.7$

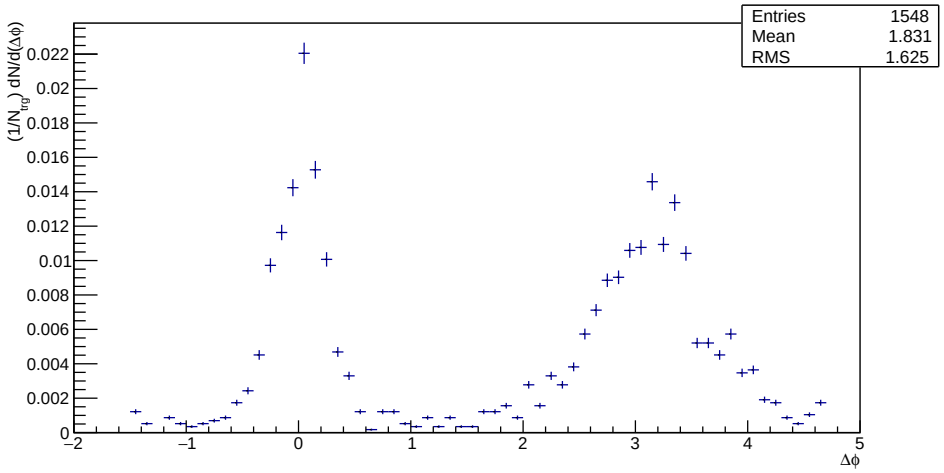

(c) $0.7 < z_T \leq 0.8$

Figure 3.26: A histogram of $\Delta\phi$ for the range $0.5 < z_T \leq 0.8$ at low multiplicity $(0 < N_{ch} \leq 20)$ for $\sqrt{s_{_{NN}}} = 13\ TeV$.

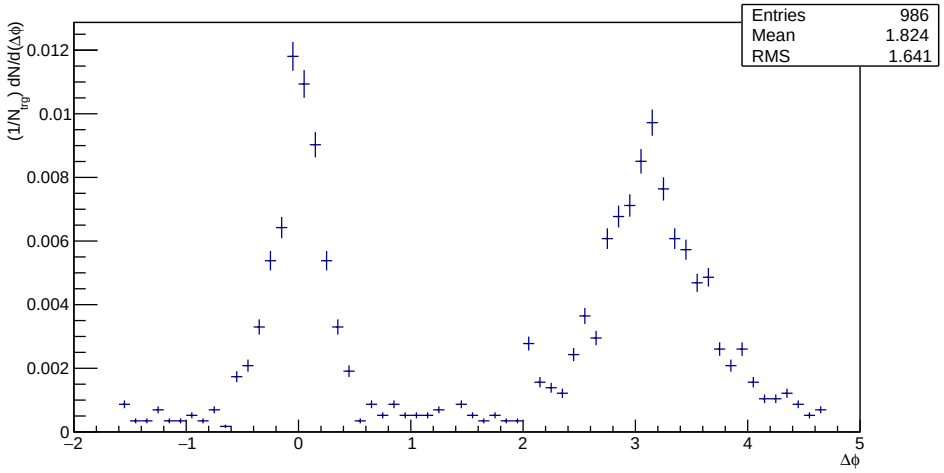

(a) $0.8 < z_T \leq 0.9$

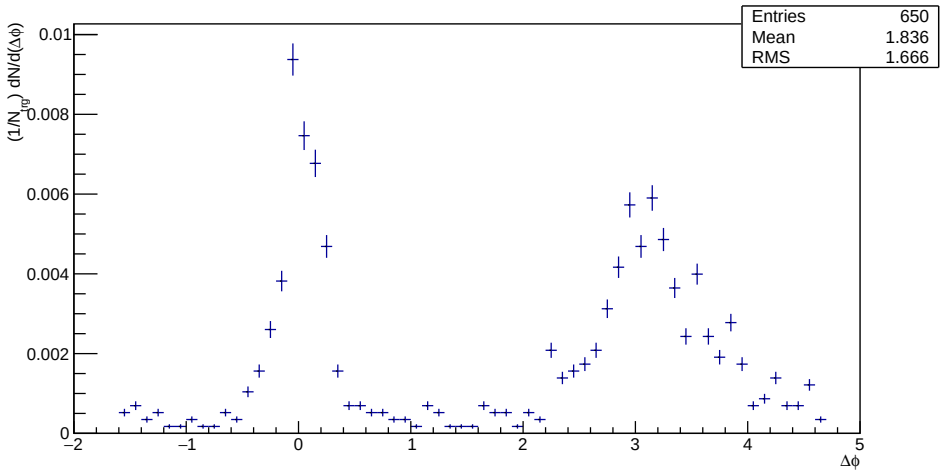

(b) $0.9 < z_T \leq 1.0$

Figure 3.27: A histogram of $\Delta\phi$ for the range $0.8 < z_T \leq 1.0$ at low multiplicity $(0 < N_{ch} \leq 20)$ for $\sqrt{s_{NN}} = 13\ TeV$.

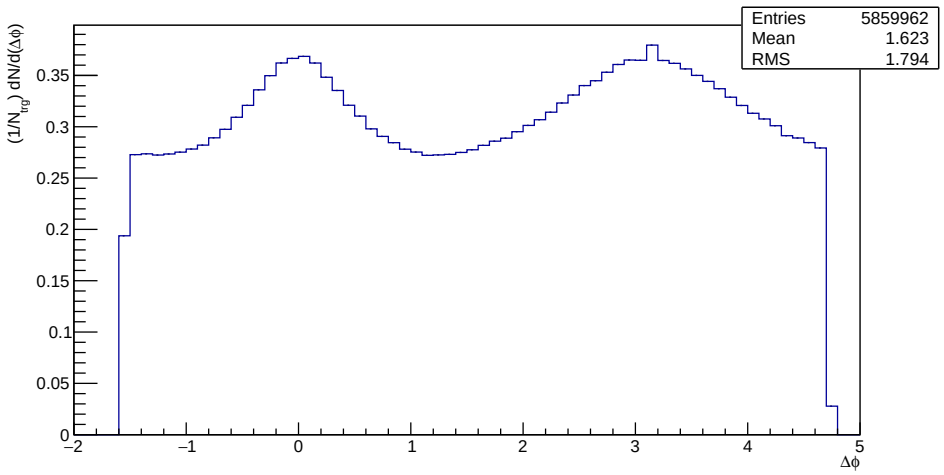

(a) $0.2 < z_T \leq 0.3$

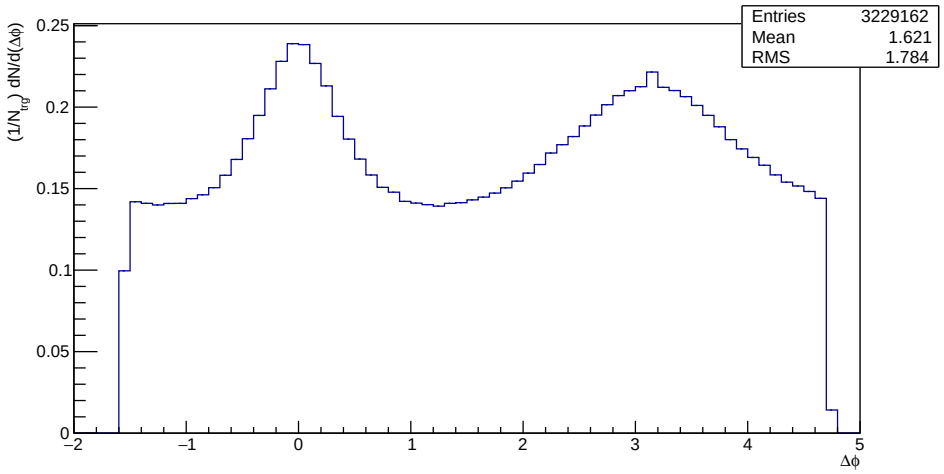

(b) $0.3 < z_T \leq 0.4$

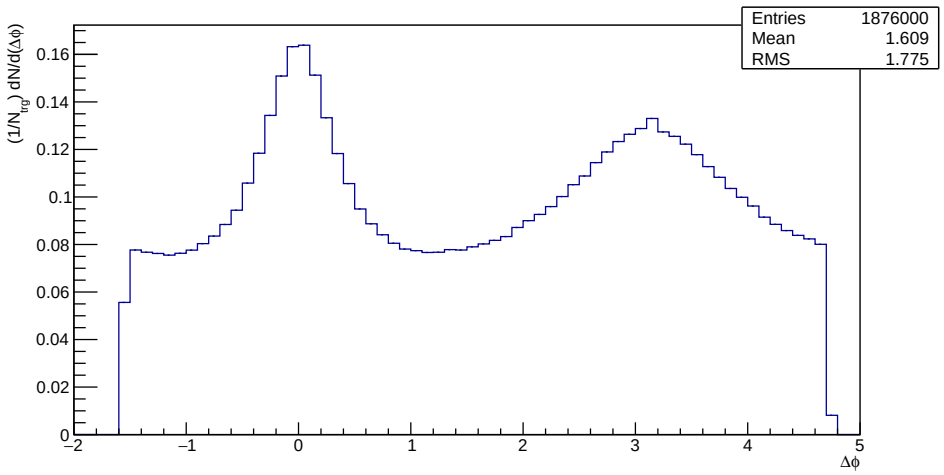

(c) $0.4 < z_T \leq 0.5$

Figure 3.28: A histogram of $\Delta\phi$ for the range $0.2 < z_T \leq 0.5$ at high multiplicity ($40 < N_{ch} \leq 80$) for $\sqrt{s_{NN}} = 13\ TeV$.

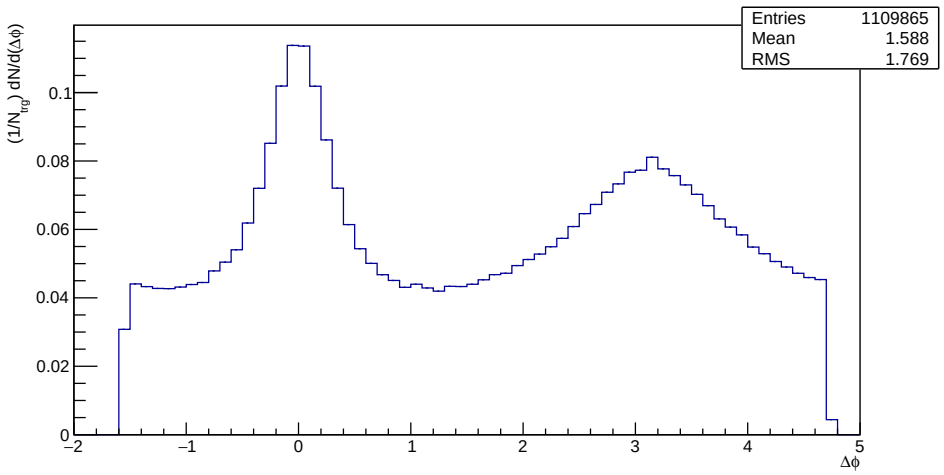

(a) $0.5 < z_T \leq 0.6$

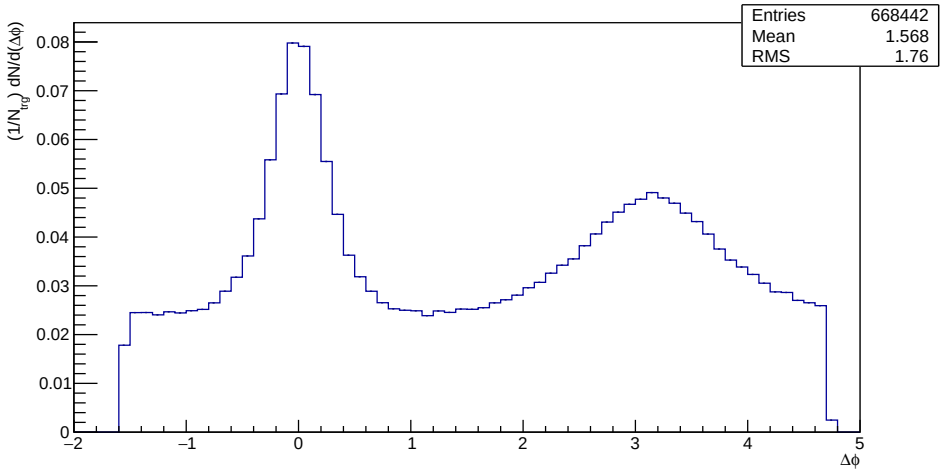

(b) $0.6 < z_T \leq 0.7$

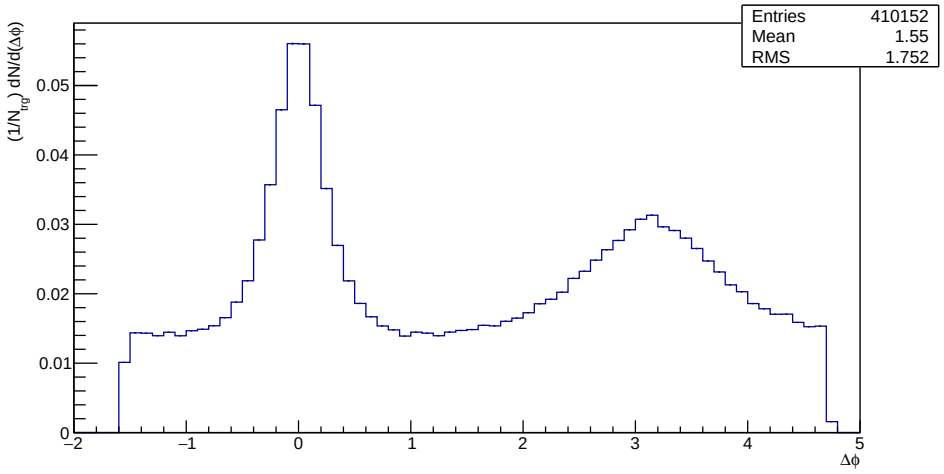

(c) $0.7 < z_T \leq 0.8$

Figure 3.29: A histogram of $\Delta\phi$ for the range $0.5 < z_T \leq 0.8$ at high multiplicity ($40 < N_{ch} \leq 80$) for $\sqrt{s_{NN}} = 13\ TeV$.

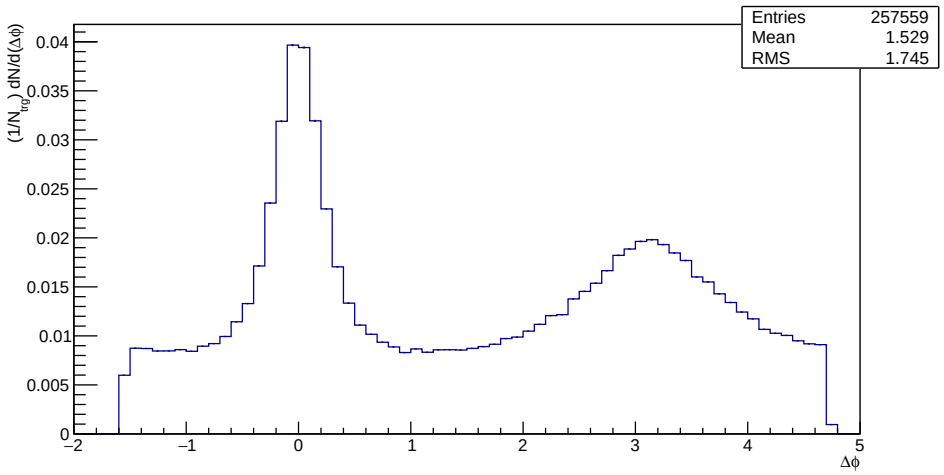

(a) $0.8 < z_T \leq 0.9$

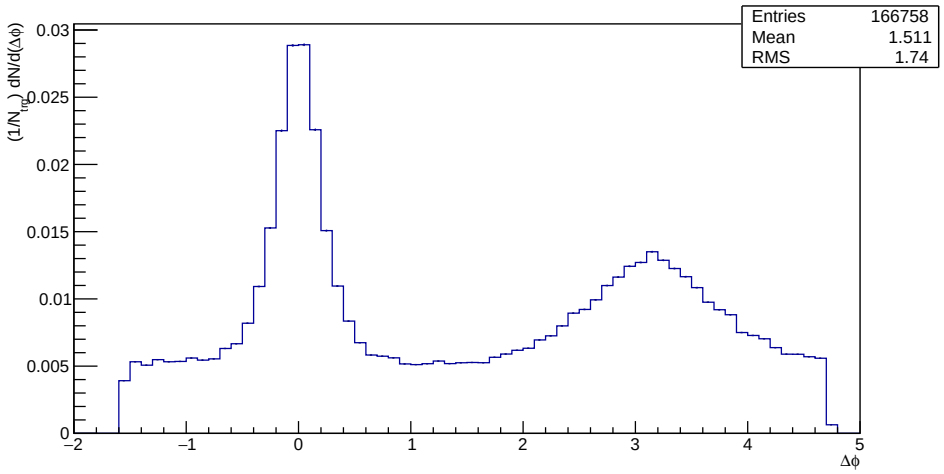

(b) $0.9 < z_T \leq 1.0$

Figure 3.30: A histogram of $\Delta\phi$ for the range $0.8 < z_T \leq 1.0$ at high multiplicity ($40 < N_{ch} \leq 80$) for $\sqrt{s_{_{NN}}} = 13\ TeV$.

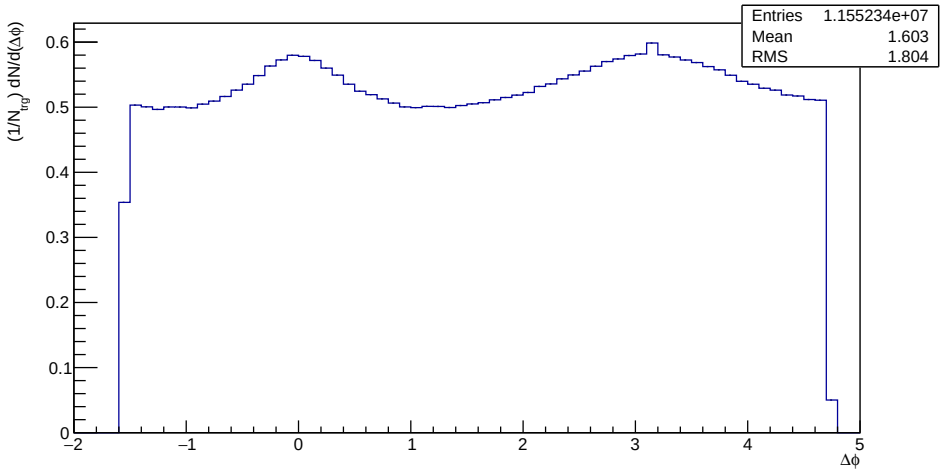

(a) $0.2 < z_T \leq 0.3$

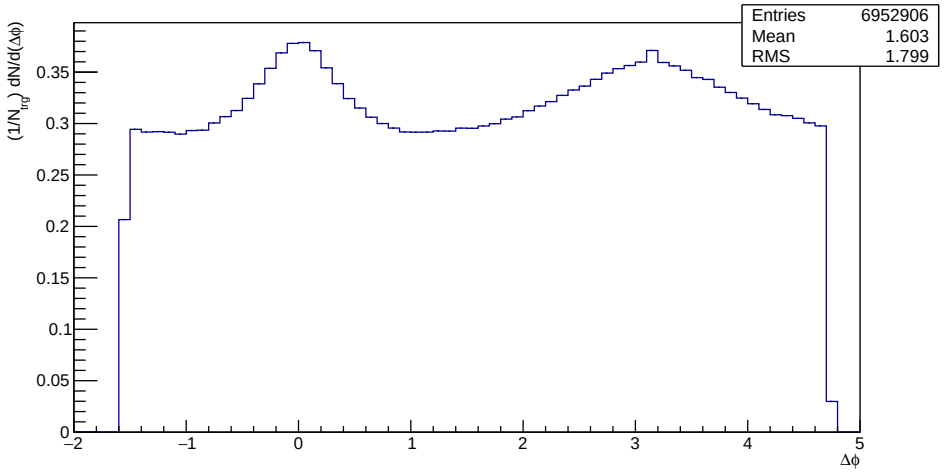

(b) $0.3 < z_T \leq 0.4$

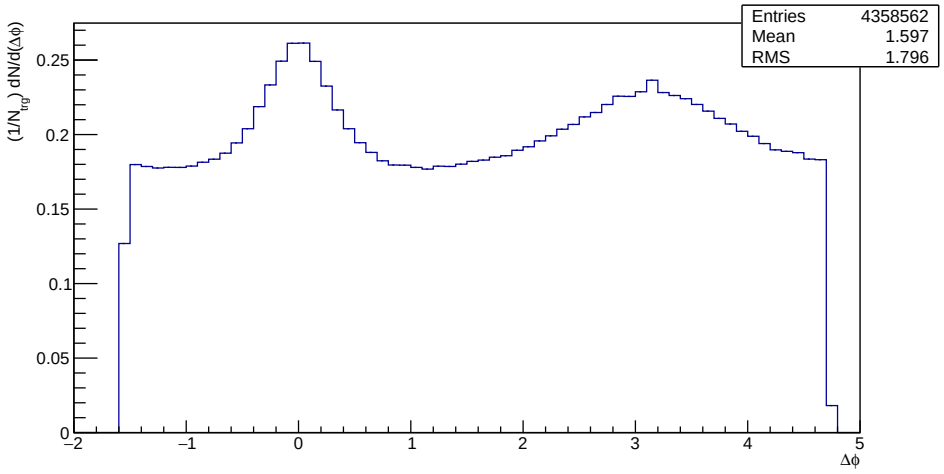

(c) $0.4 < z_T \leq 0.5$

Figure 3.31: A histogram of $\Delta\phi$ for the range $0.2 < z_T \leq 0.5$ at high multiplicity ($80 < N_{ch} \leq 120$) for $\sqrt{s_{NN}} = 13\ TeV$.

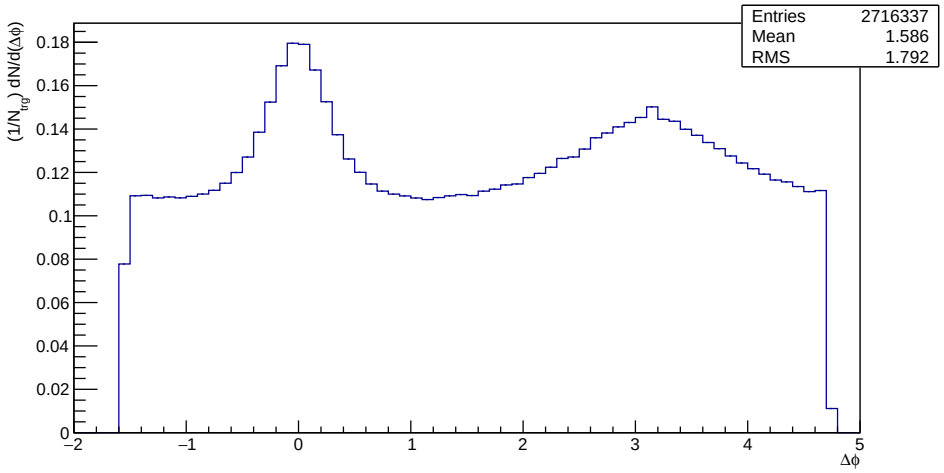

(a) $0.5 < z_T \leq 0.6$

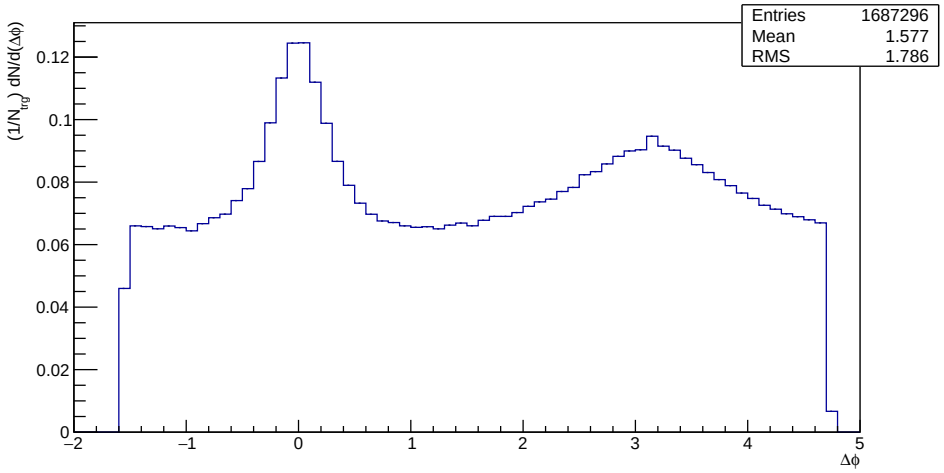

(b) $0.6 < z_T \leq 0.7$

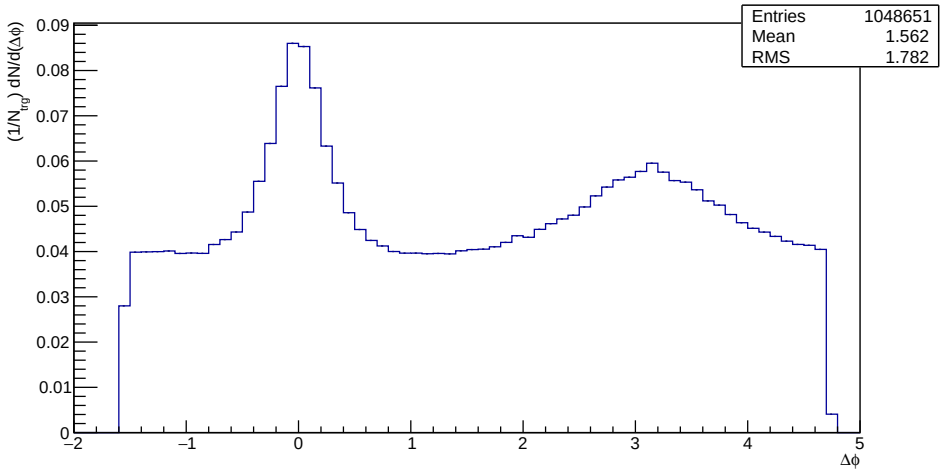

(c) $0.7 < z_T \leq 0.8$

Figure 3.32: A histogram of $\Delta\phi$ for the range $0.5 < z_T \leq 0.8$ at high multiplicity ($80 < N_{ch} \leq 120$) for $\sqrt{s_{NN}} = 13\ TeV$.

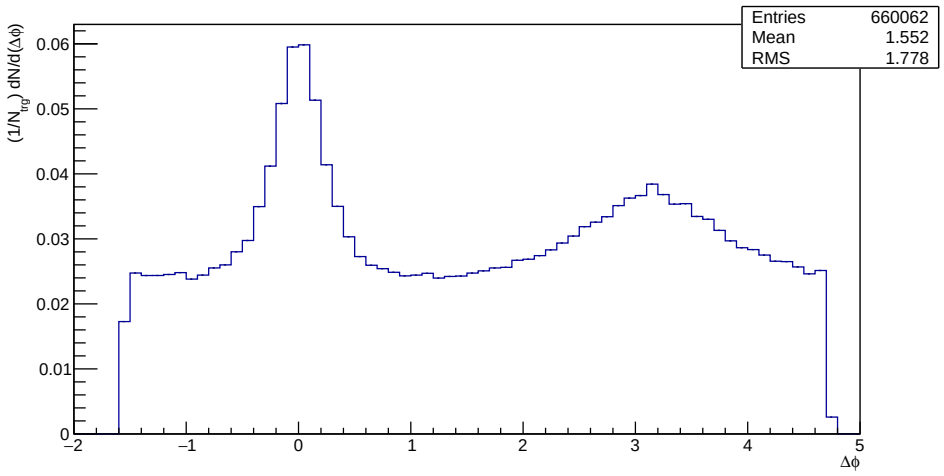

(a) $0.8 < z_T \leq 0.9$

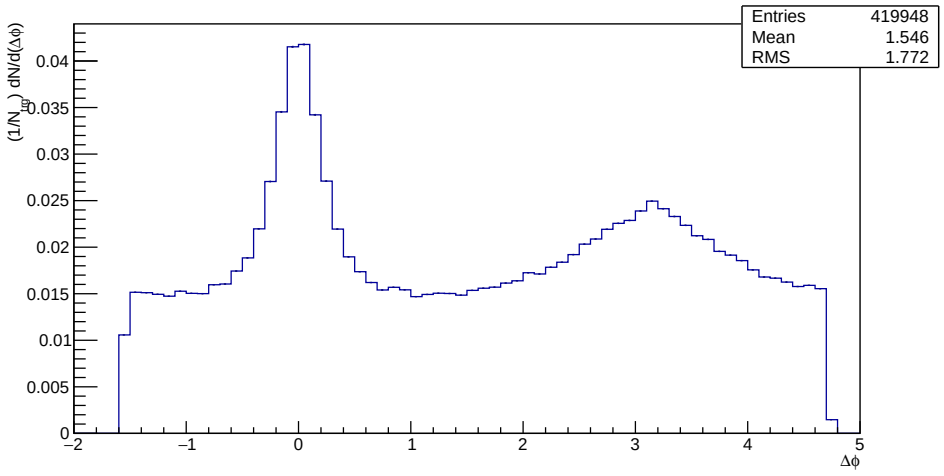

(b) $0.9 < z_T \leq 1.0$

Figure 3.33: A histogram of $\Delta\phi$ for the range $0.8 < z_T \leq 1.0$ at high multiplicity ($80 < N_{ch} \leq 120$) for $\sqrt{s_{_{NN}}} = 13\ TeV$.

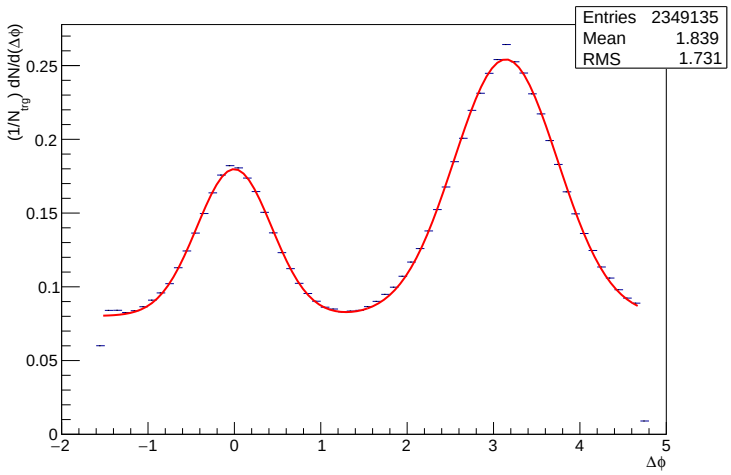

(a) $0.2 < z_T \leq 0.3$

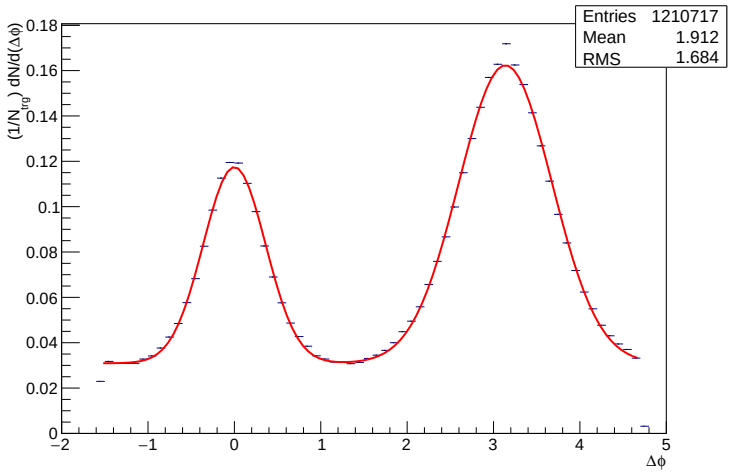

(b) $0.3 < z_T \leq 0.4$

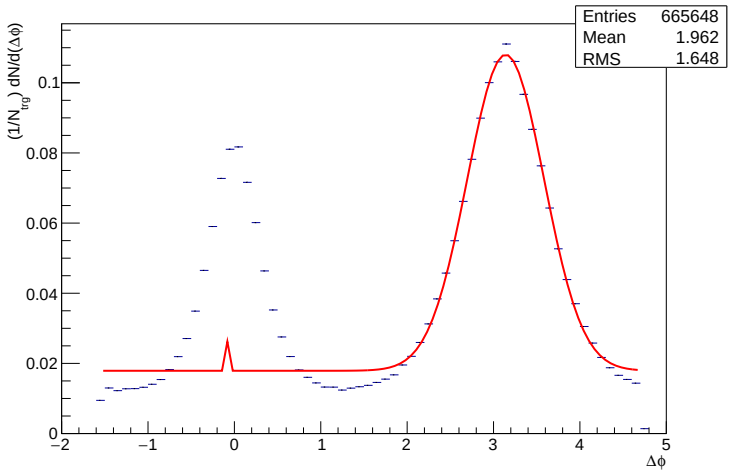

(c) $0.4 < z_T \leq 0.5$

Figure 3.34: A histogram of $\Delta\phi$ for the range $0.2 < z_T \leq 0.5$ at low multiplicity $(0 < N_{ch} \leq 20)$ for $\sqrt{s_{NN}} = 200\ GeV$.

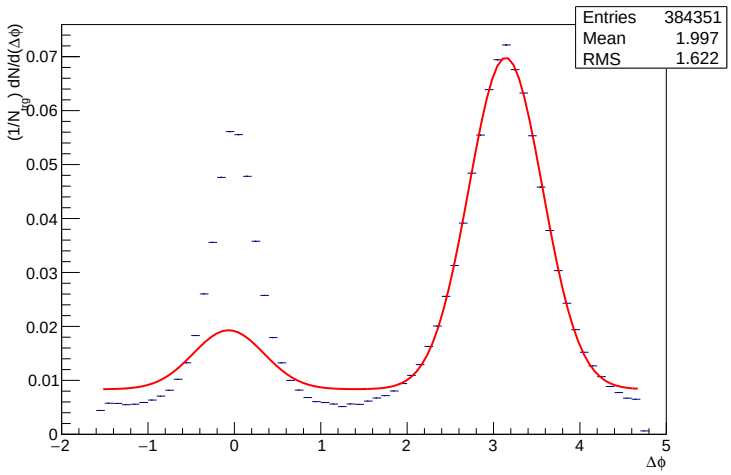

(a) $0.5 < z_T \leq 0.6$

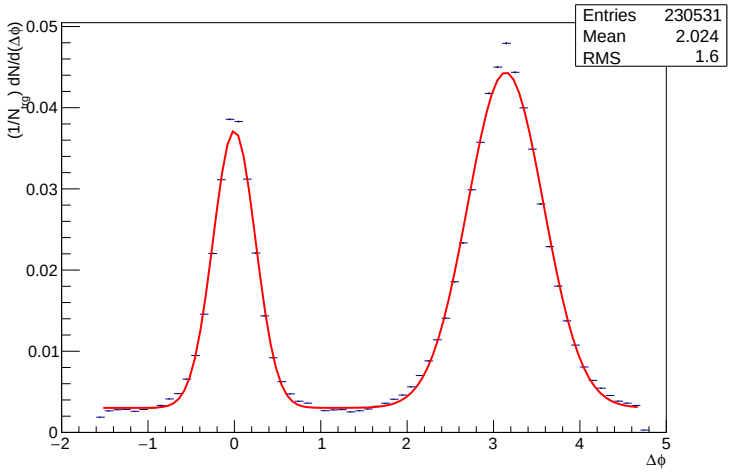

(b) $0.6 < z_T \leq 0.7$

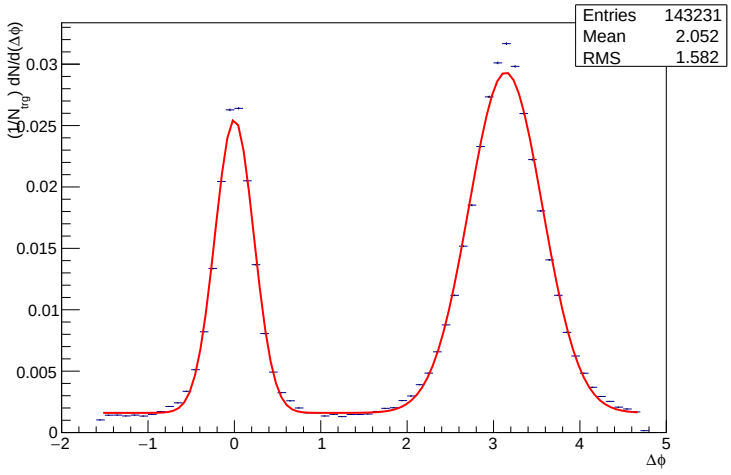

(c) $0.7 < z_T \leq 0.8$

Figure 3.35: A histogram of $\Delta\phi$ for the range $0.5 < z_T \leq 0.8$ at low multiplicity $(0 < N_{ch} \leq 20)$ for $\sqrt{s_{NN}} = 200\ GeV$.

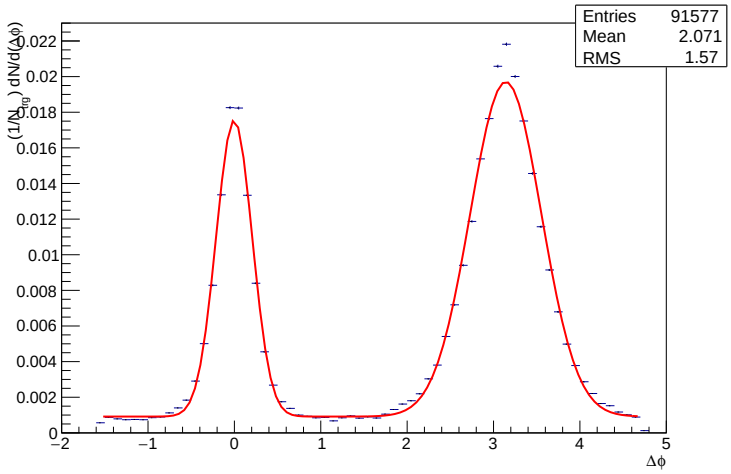

(a) $0.8 < z_T \leq 0.9$

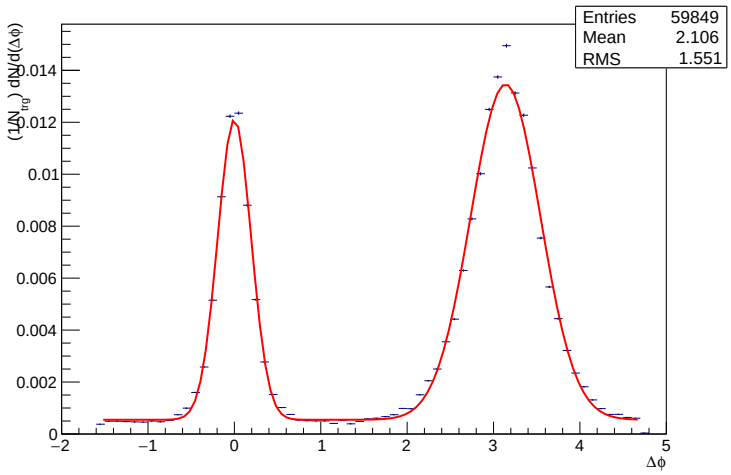

(b) $0.9 < z_T \leq 1.0$

Figure 3.36: A histogram of $\Delta\phi$ for the range $0.8 < z_T \leq 1.0$ at low multiplicity $(0 < N_{ch} \leq 20)$ for $\sqrt{s_{NN}} = 200\ GeV$.

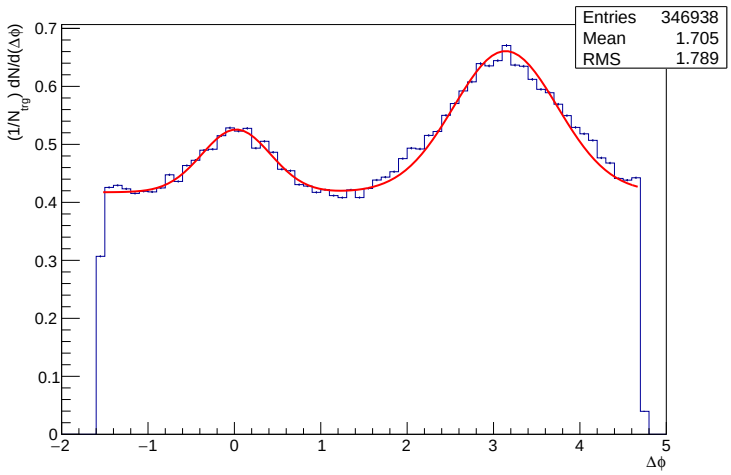

(a) $0.2 < z_T \leq 0.3$

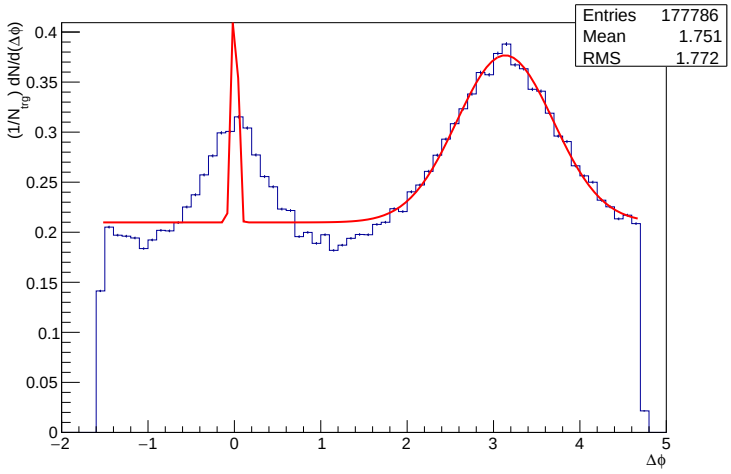

(b) $0.3 < z_T \leq 0.4$

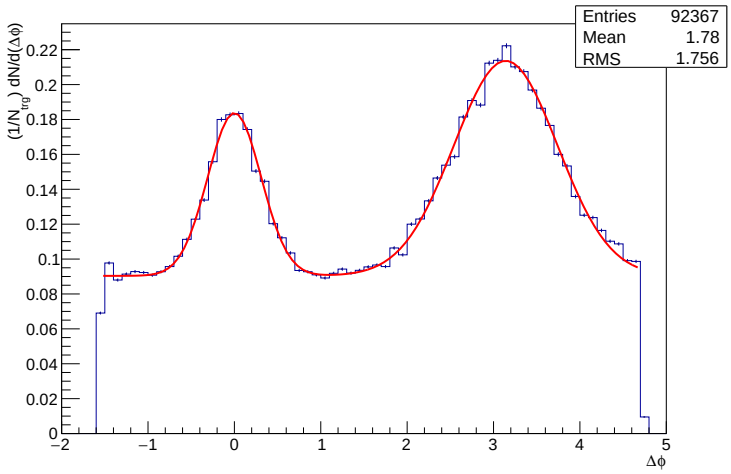

(c) $0.4 < z_T \leq 0.5$

Figure 3.37: A histogram of $\Delta\phi$ for the range $0.2 < z_T \leq 0.5$ at high multiplicity $(40 < N_{ch} \leq 80)$ for $\sqrt{s_{NN}} = 200\ GeV$.

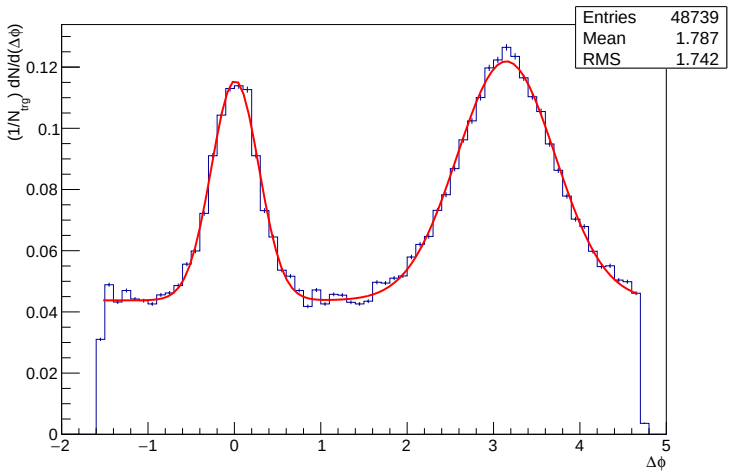

(a) $0.5 < z_T \leq 0.6$

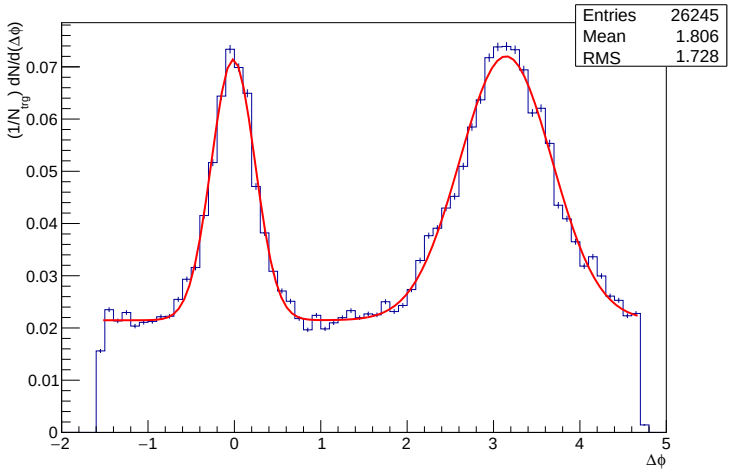

(b) $0.6 < z_T \leq 0.7$

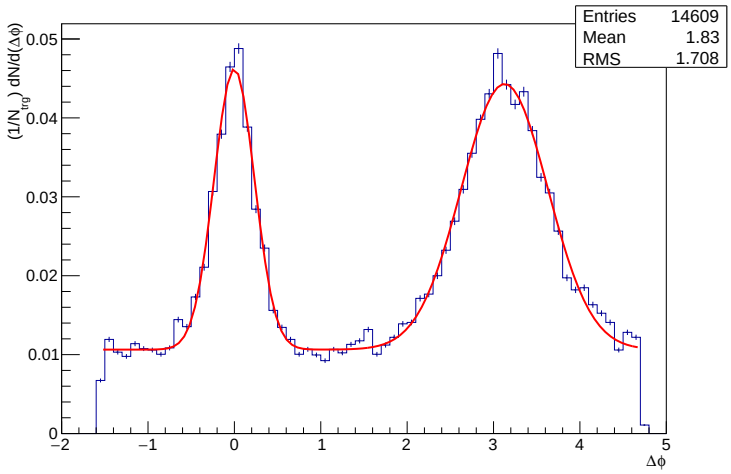

(c) $0.7 < z_T \leq 0.8$

Figure 3.38: A histogram of $\Delta\phi$ for the range $0.5 < z_T \leq 0.8$ at high multiplicity $(40 < N_{ch} \leq 80)$ for $\sqrt{s_{NN}} = 200\ GeV$.

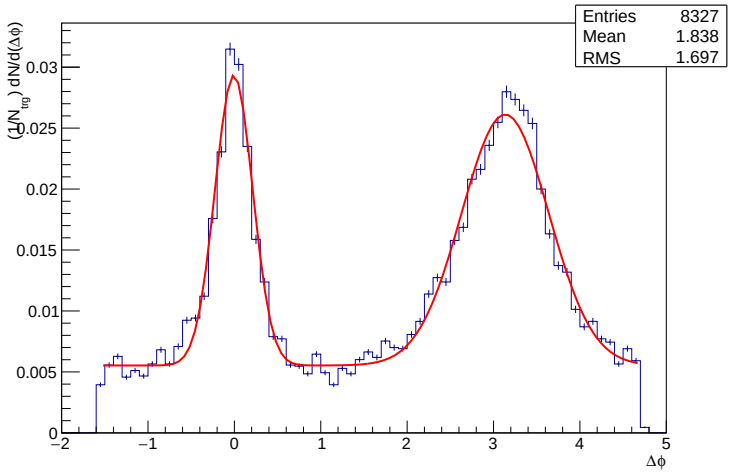

(a) $0.8 < z_T \leq 0.9$

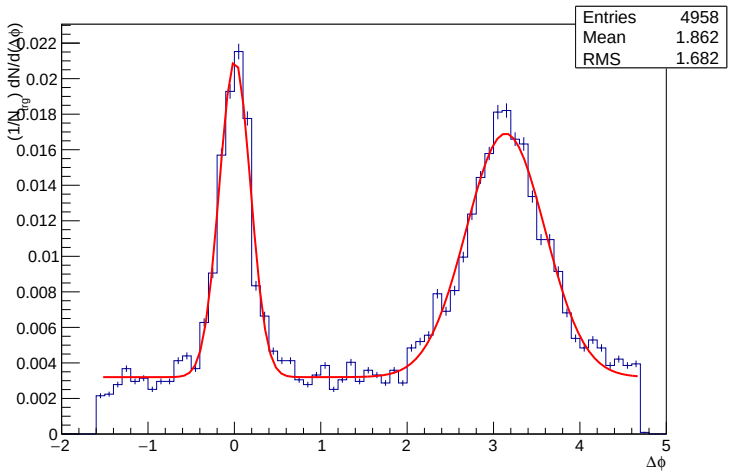

(b) $0.9 < z_T \leq 1.0$

Figure 3.39: A histogram of $\Delta\phi$ for the range $0.8 < z_T \leq 1.0$ at high multiplicity $(40 < N_{ch} \leq 80)$ for $\sqrt{s_{NN}} = 200\ GeV$.

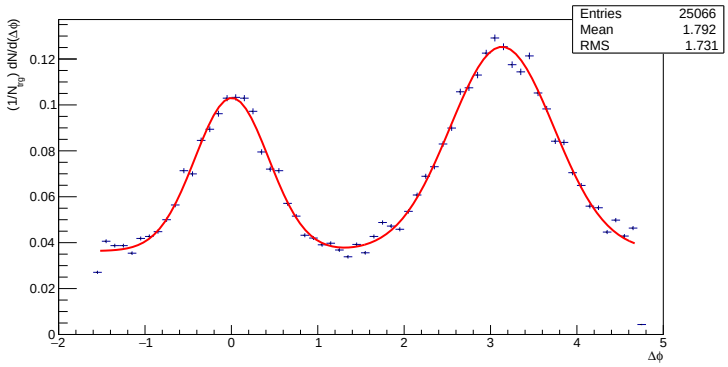

(a) $0.2 < z_T \leq 0.3$

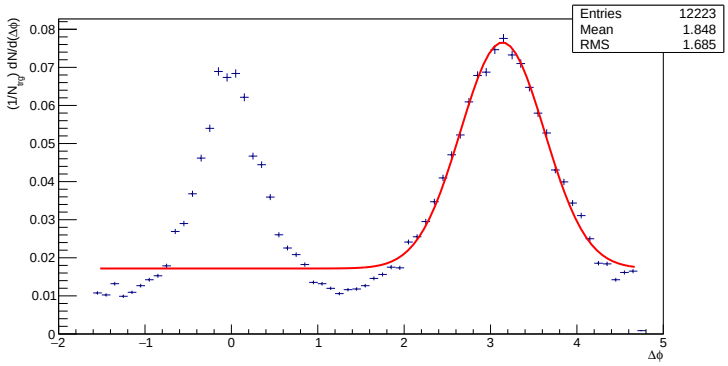

(b) $0.3 < z_T \leq 0.4$

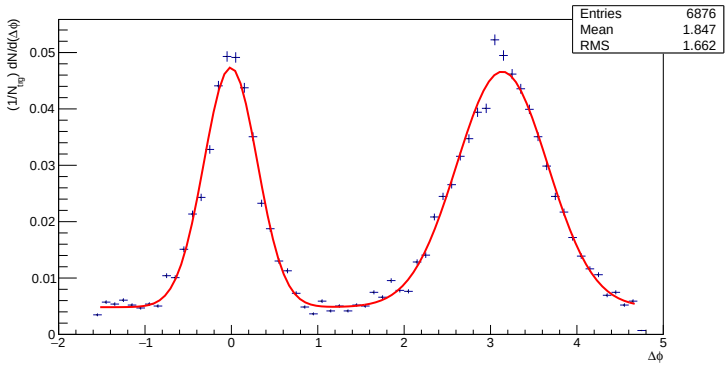

(c) $0.4 < z_T \leq 0.5$

Figure 3.40: A histogram of $\Delta\phi$ for the range $0.2 < z_T \leq 0.5$ at low multiplicity $(0 < N_{ch} \leq 20)$ for $\sqrt{s_{NN}} = 13\ TeV$.

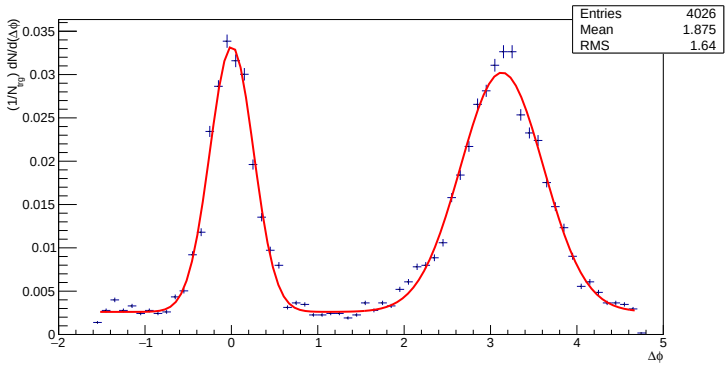

(a) $0.5 < z_T \leq 0.6$

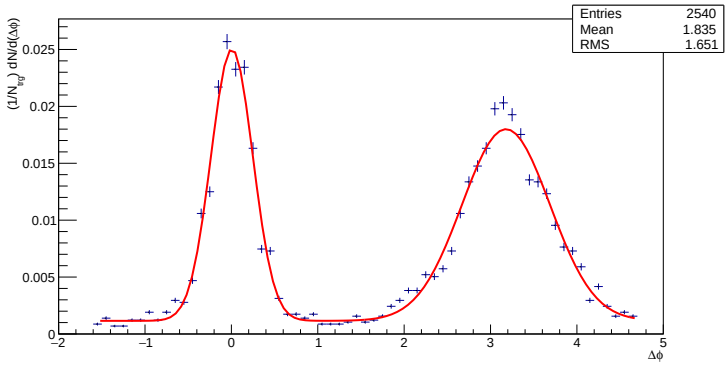

(b) $0.6 < z_T \leq 0.7$

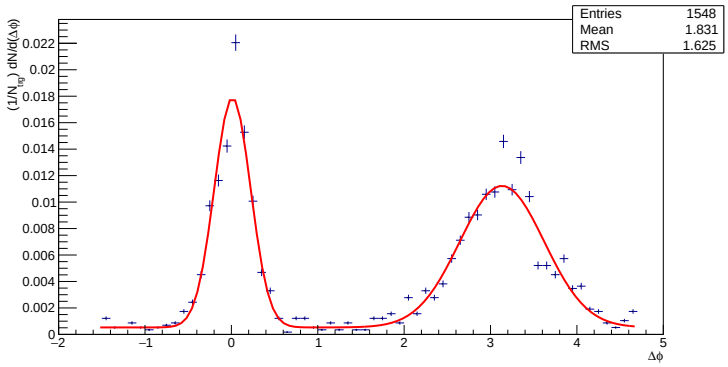

(c) $0.7 < z_T \leq 0.8$

Figure 3.41: A histogram of $\Delta\phi$ for the range $0.5 < z_T \leq 0.8$ at low multiplicity $(0 < N_{ch} \leq 20)$ for $\sqrt{s_{NN}} = 13\ TeV$.

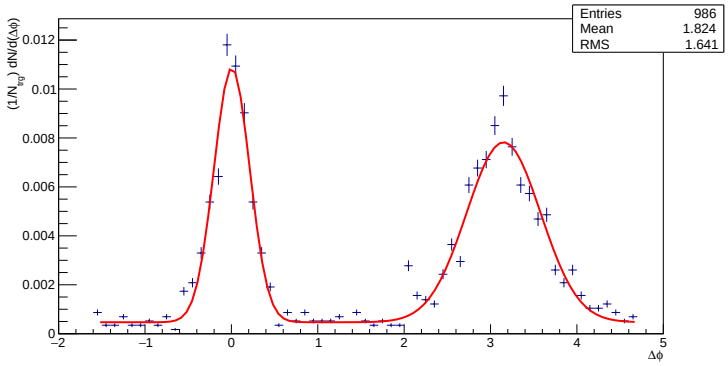

(a) $0.8 < z_T \leq 0.9$

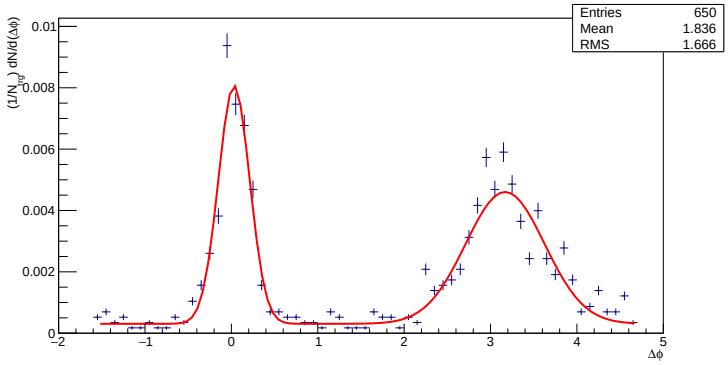

(b) $0.9 < z_T \leq 1.0$

Figure 3.42: A histogram of $\Delta\phi$ for the range $0.8 < z_T \leq 1.0$ at low multiplicity $(0 < N_{ch} \leq 20)$ for $\sqrt{s_{_{NN}}} = 13\ TeV$.

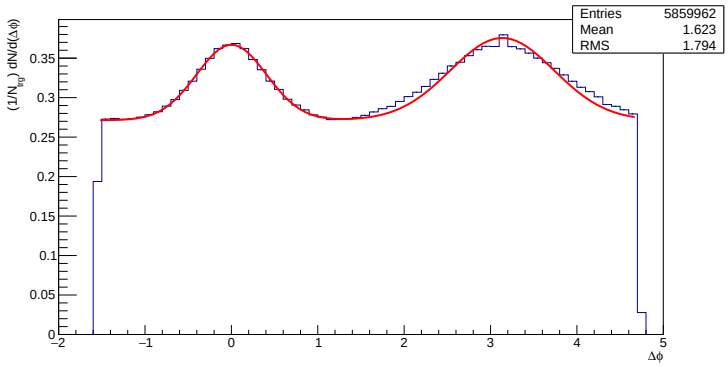

(a) $0.2 < z_T \leq 0.3$

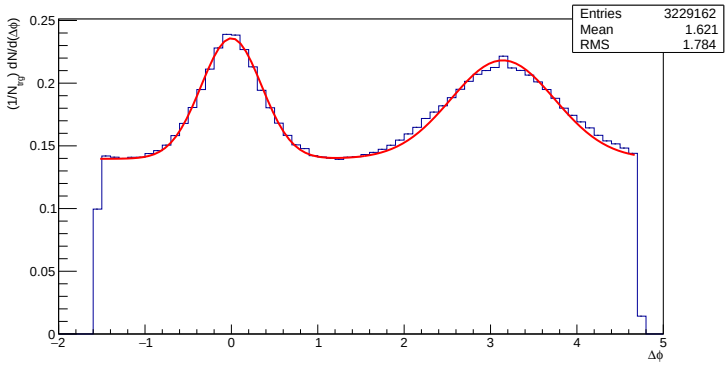

(b) $0.3 < z_T \leq 0.4$

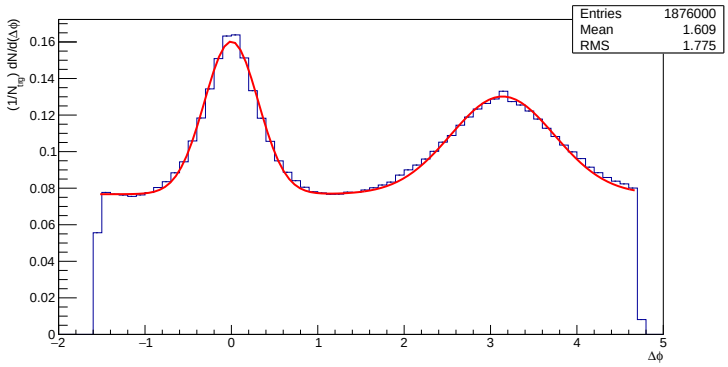

(c) $0.4 < z_T \leq 0.5$

Figure 3.43: A histogram of $\Delta\phi$ for the range $0.2 < z_T \leq 0.5$ at high multiplicity ($40 < N_{ch} \leq 80$) for $\sqrt{s_{NN}} = 13\ TeV$.

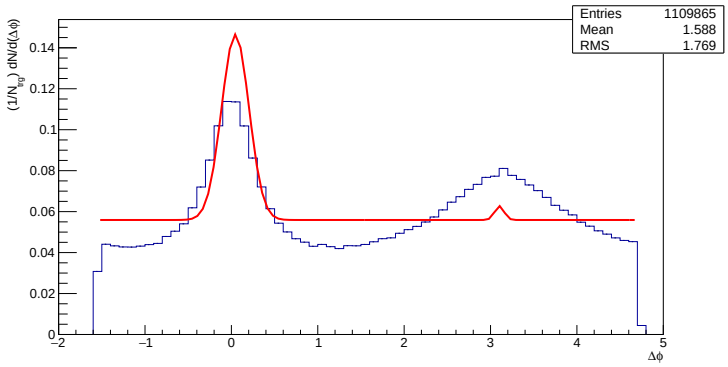

(a) $0.5 < z_T \leq 0.6$

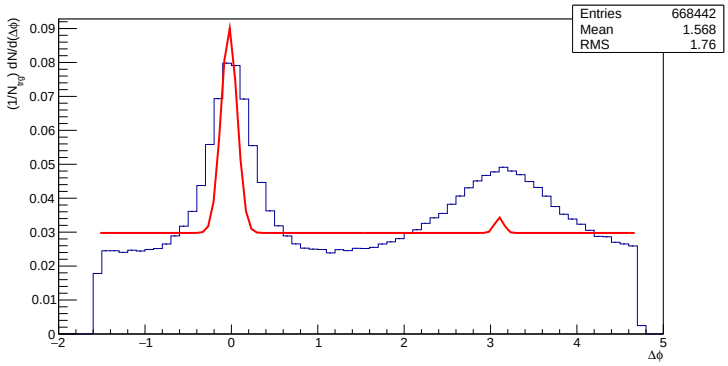

(b) $0.6 < z_T \leq 0.7$

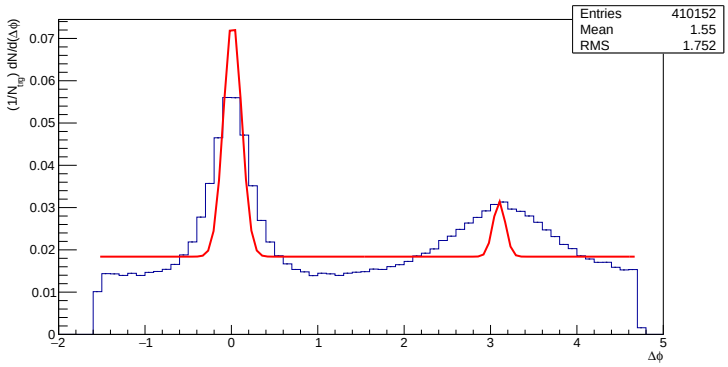

(c) $0.7 < z_T \leq 0.8$

Figure 3.44: A histogram of $\Delta\phi$ for the range $0.5 < z_T \leq 0.8$ at high multiplicity ($40 < N_{ch} \leq 80$) for $\sqrt{s_{NN}} = 13\ TeV$.

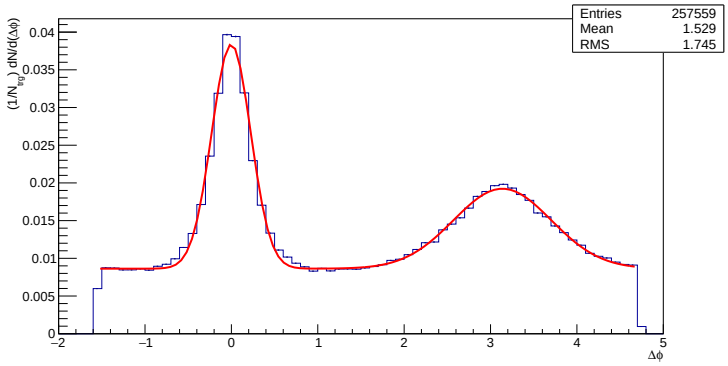

(a) $0.8 < z_T \leq 0.9$

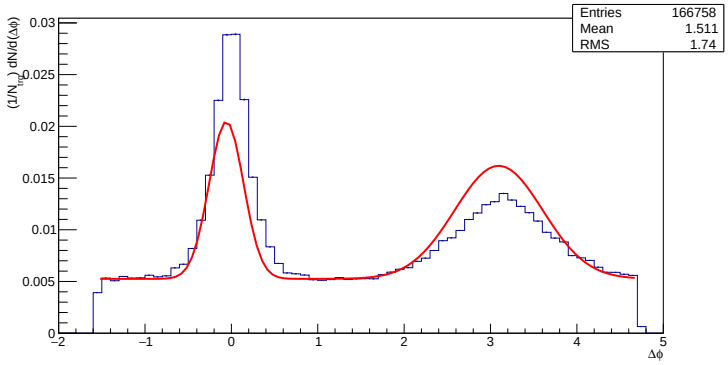

(b) $0.9 < z_T \leq 1.0$

Figure 3.45: A histogram of $\Delta\phi$ for the range $0.8 < z_T \leq 1.0$ at high multiplicity ($40 < N_{ch} \leq 80$) for $\sqrt{s_{_{NN}}} = 13\ TeV$.

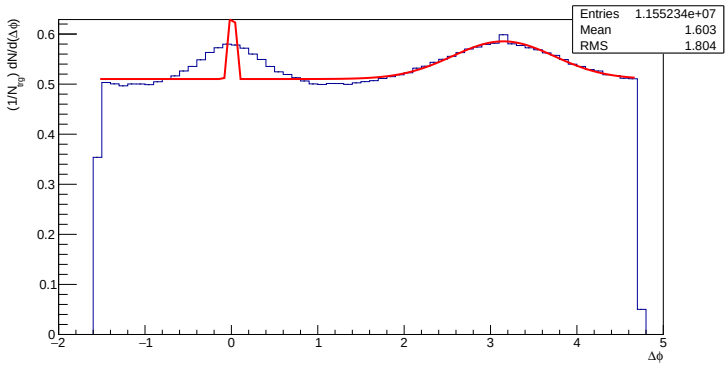

(a) $0.2 < z_T \leq 0.3$

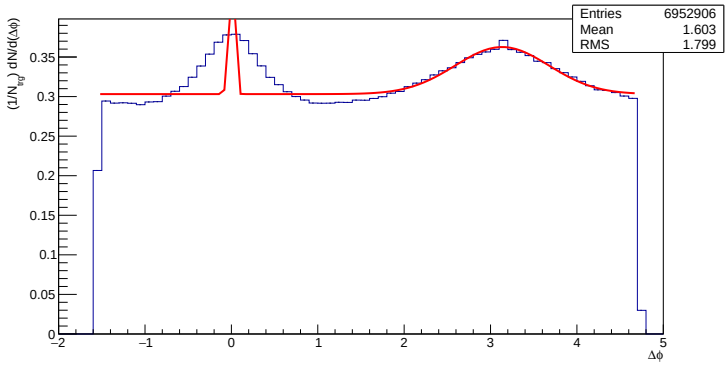

(b) $0.3 < z_T \leq 0.4$

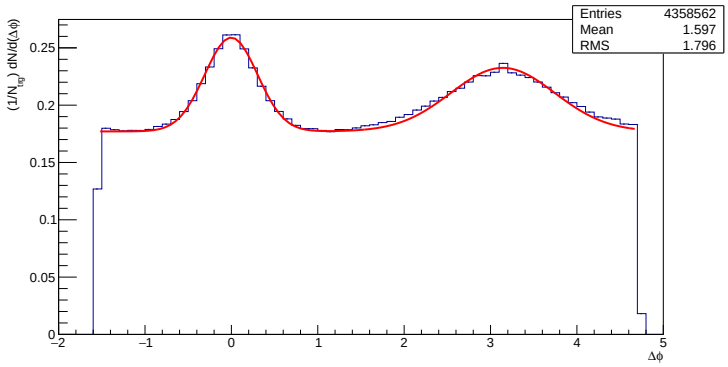

(c) $0.4 < z_T \leq 0.5$

Figure 3.46: A histogram of $\Delta\phi$ for the range $0.2 < z_T \leq 0.5$ at high multiplicity ($80 < N_{ch} \leq 120$) for $\sqrt{s_{NN}} = 13\ TeV$.

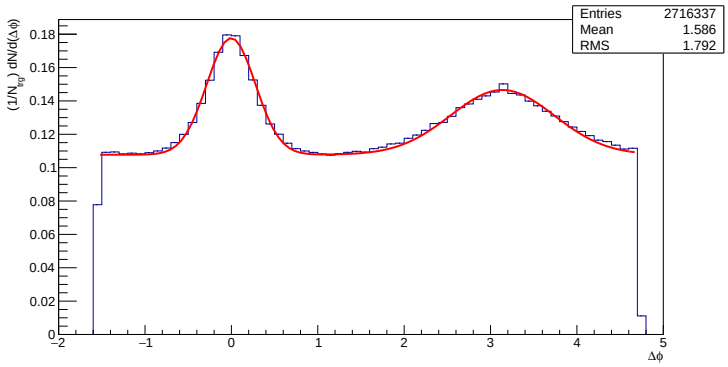

(a) $0.5 < z_T \leq 0.6$

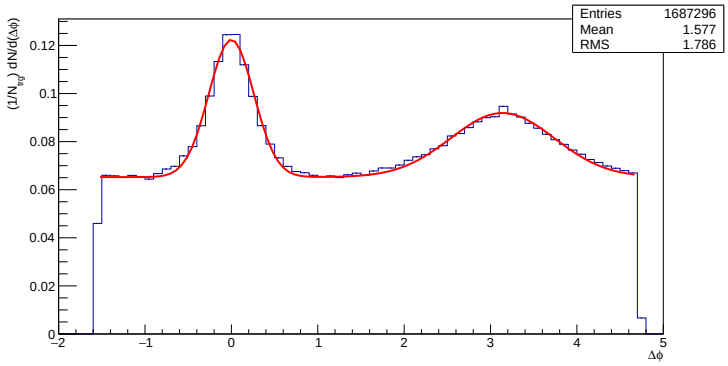

(b) $0.6 < z_T \leq 0.7$

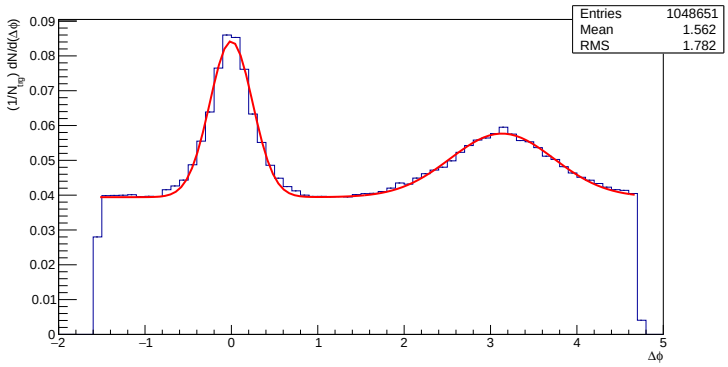

(c) $0.7 < z_T \leq 0.8$

Figure 3.47: A histogram of $\Delta\phi$ for the range $0.5 < z_T \leq 0.8$ at high multiplicity ($80 < N_{ch} \leq 120$) for $\sqrt{s_{NN}} = 13\ TeV$.

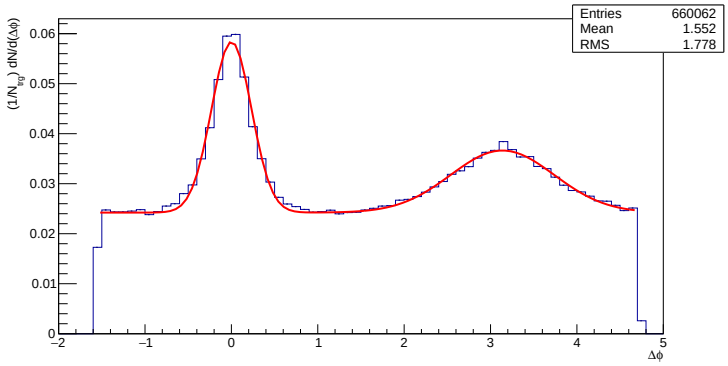

(a) $0.8 < z_T \leq 0.9$

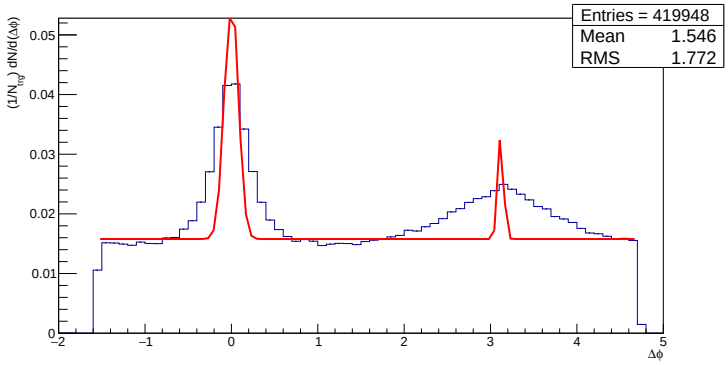

(b) $0.9 < z_T \leq 1.0$

Figure 3.48: A histogram of $\Delta\phi$ for the range $0.8 < z_T \leq 1.0$ at high multiplicity ($80 < N_{ch} \leq 120$) for $\sqrt{s_{_{NN}}} = 13\ TeV$.

3.3 Yields Extractions

The number of associated particles per trigger, the yield per trigger $(\frac{1}{N_{trg}})\frac{dN}{d(\Delta\phi)}$ is found by counting the entries underneath the peaks within certain $|\Delta\phi|$ window after subtracting the background as determined from the straight line of the fit at the near side and the away side. The integrating region for near side yield was $|\Delta\phi| < 0.63$ and for the away side was $|\Delta\phi – \pi| < 0.63$. For each z_T bin, the normalized near side and away sides yields were extracted at the RHIC and LHC corresponding energies for the low and high multiplicity classes, and shown in figures 3.49 to 3.52.

As clearly shown from the figures, the near side yields at RHIC and LHC for the low and high multiplicity events are approximately similar. However the yield at RHIC is harder than that at LHC in the away side. This might be due to the effect of two reasons, different probed parton distribution functions (x_T) regions and medium effects. First, the probed x_T at RHIC is higher than the probed x_T at LHC. From the deep inelastic scattering measurements [48], it is already known that the gluons significantly dominate the parton distribution functions at low x_T for the selected kinematic region for this analysis. Since the fragmentation function of the gluon jets is softer than that of the quark jets, then it is expected the yield at RHIC to be harder than LHC within the same kinematic region. Second, the suppression of the far side at LHC with respect to RHIC for the same classes of events might also be due to the medium effect, where the energy density of the formed medium at LHC is expected to be higher than that at RHIC. Accordingly the propagated parton loses more energy traversing the medium at LHC than at RHIC.

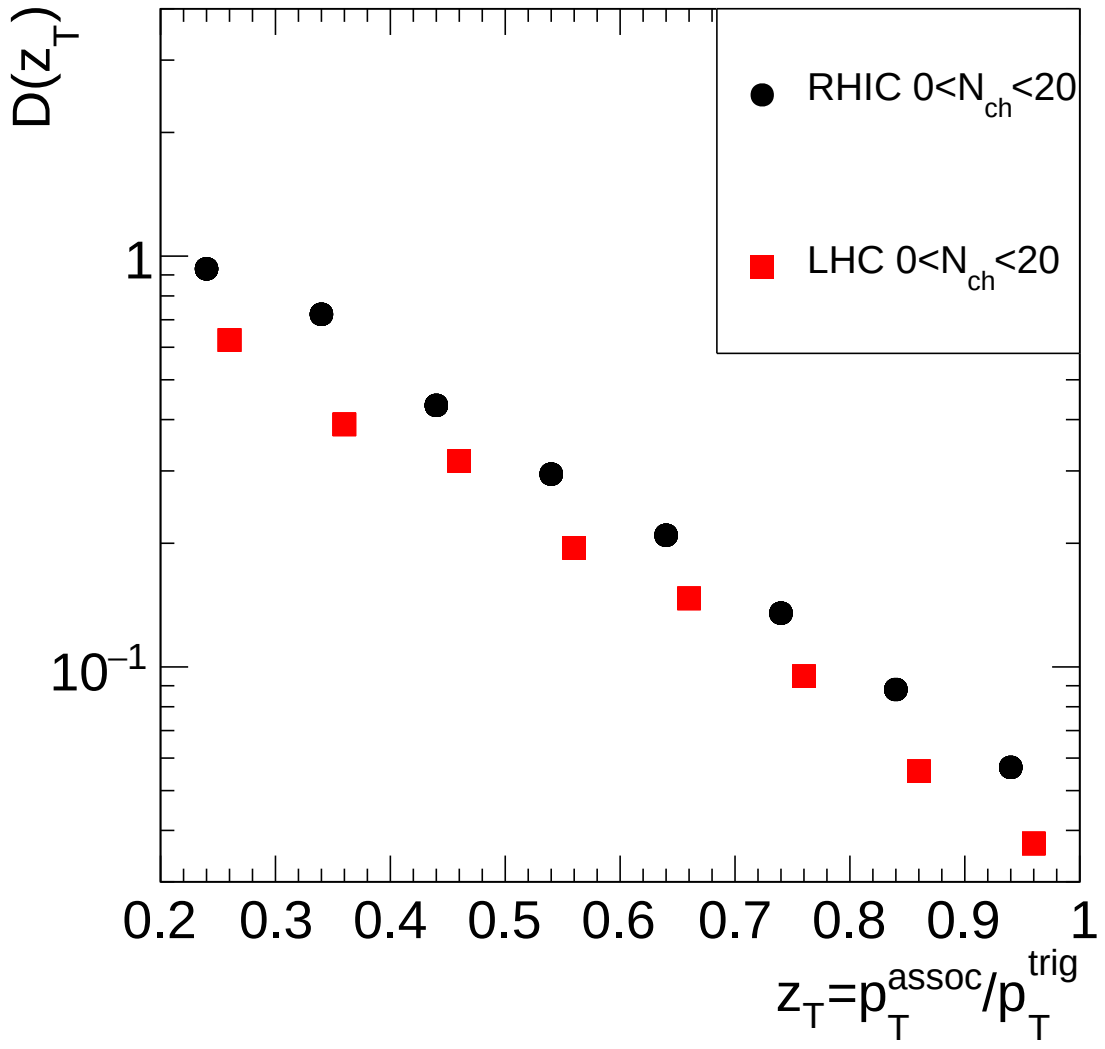

Figure 3.49: Near side yield for both RHIC and LHC energies at low multiplicity.

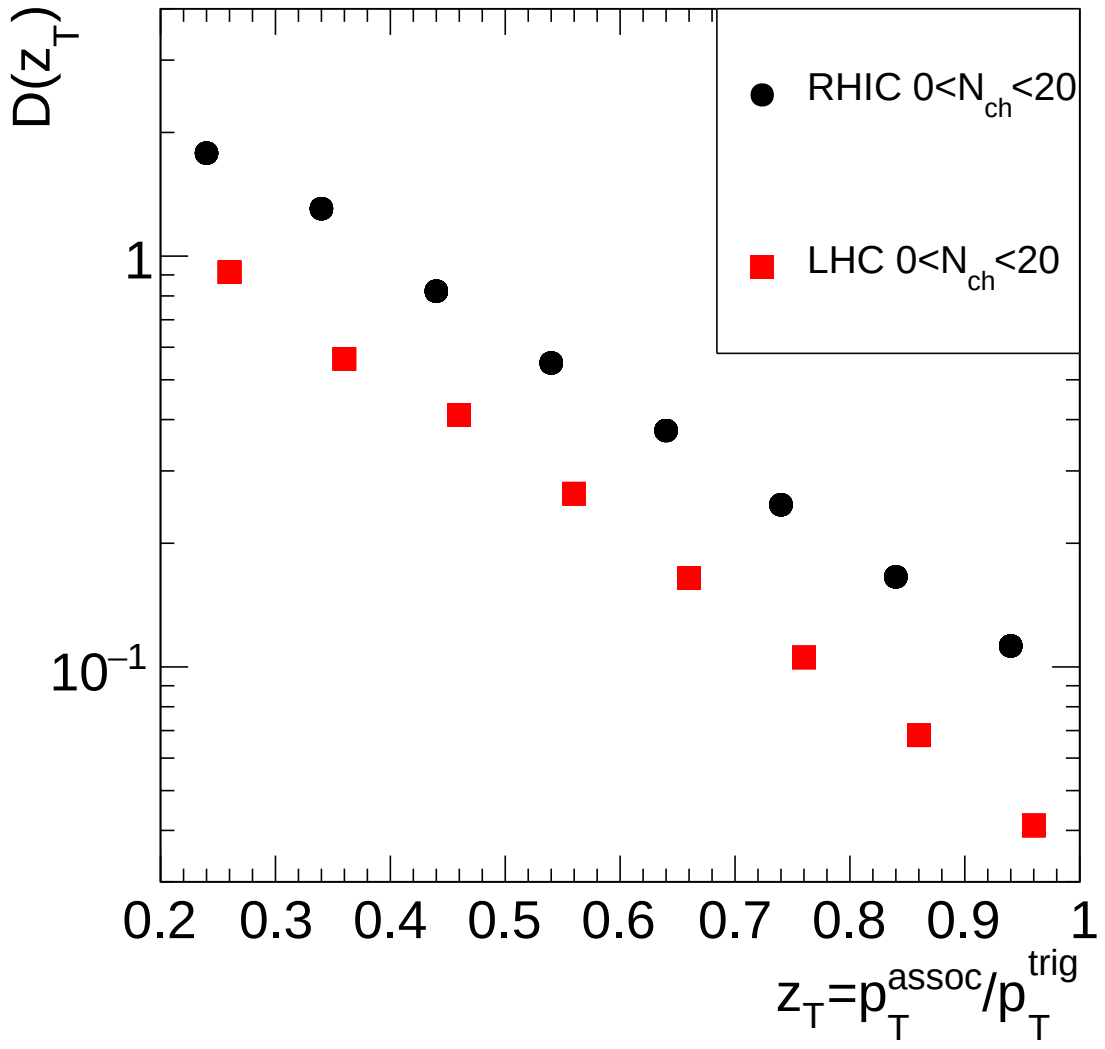

Figure 3.50: Far side yield for both RHIC and LHC energies at low multiplicity.

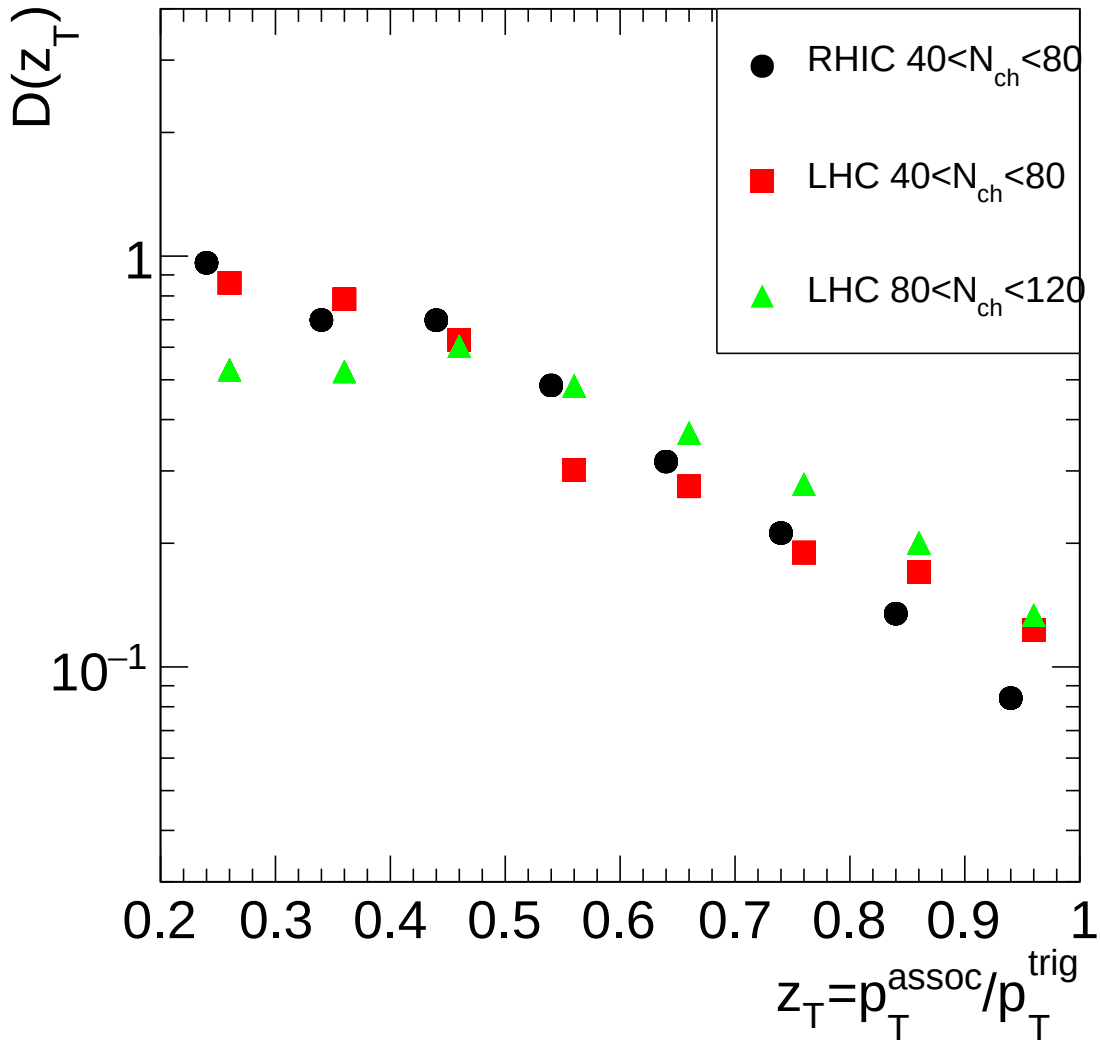

Figure 3.51: Near side yield for both RHIC and LHC energies at high multiplicity.

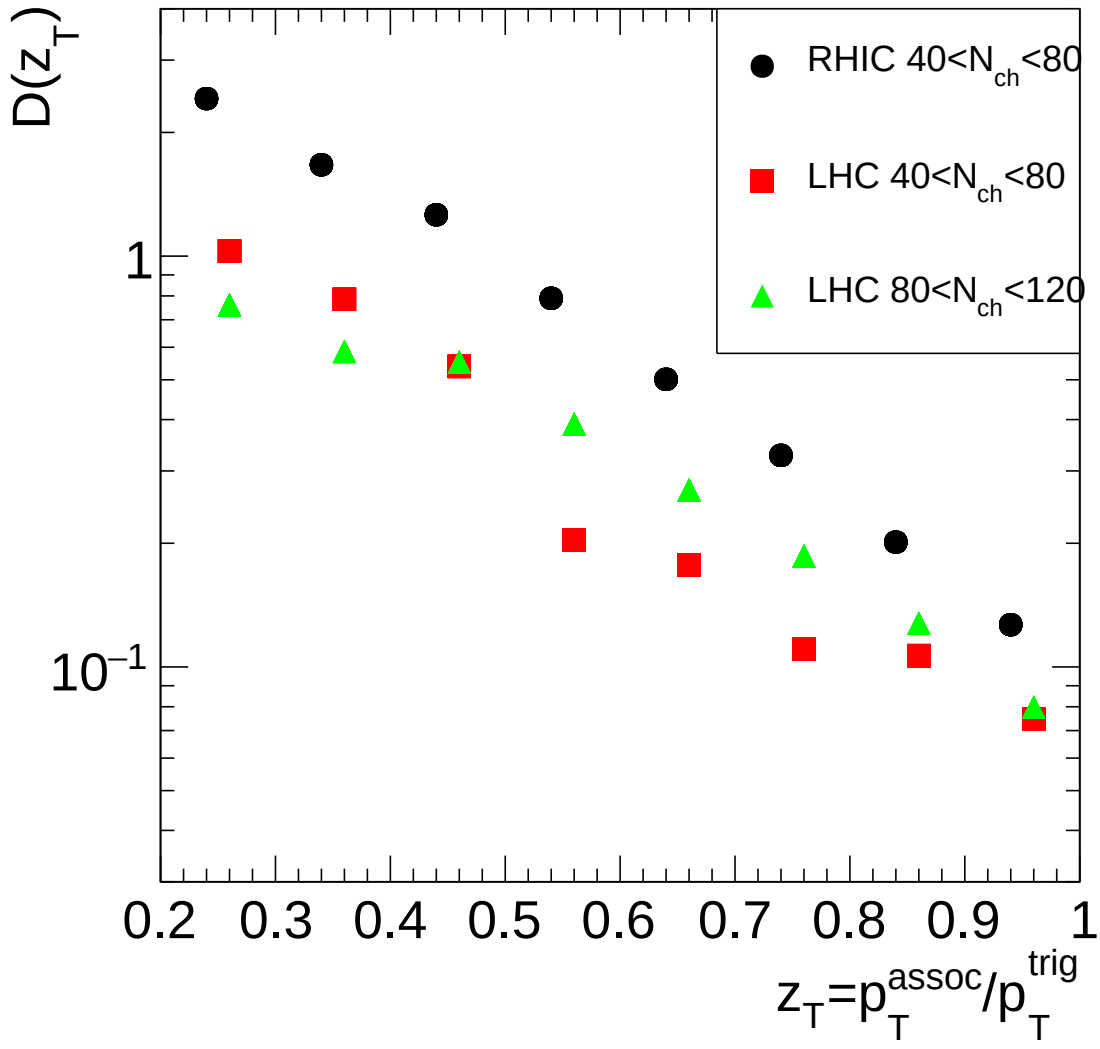

Figure 3.52: Far side yield for both RHIC and LHC energies at high multiplicity.

3.4 Results

In order to search for the medium effect, the quark-gluon plasma in proton-proton collisions, the ratio between the yields of the near side and away side at low and high multiplicity are calculated and plotted as a function of z_T as shown in figures 3.53 and 3.54.

At RHIC energy, the ratio is smaller than 1 and doesn't show any strong dependence on z_T. These results are consistent with the previously published results at RHIC where the value of jet suppression extracting from the spectra and the two-particle azimuthal correlation show no dependence neither on p_T nor z_T [43]. However the pattern of the results at LHC carries a different message, where the ratio of the low multiplicity events are smaller than 1 but higher than 1 for the high multiplicity. The results at LHC suggest the medium effect for the event with high multiplicity and accordingly the possibility of the QGP formation within those types of events. The formation of QGP or the medium effect at the high multiplicity event at LHC was recently observed through the ridge formation and the strangeness enhancement. [41, 49]

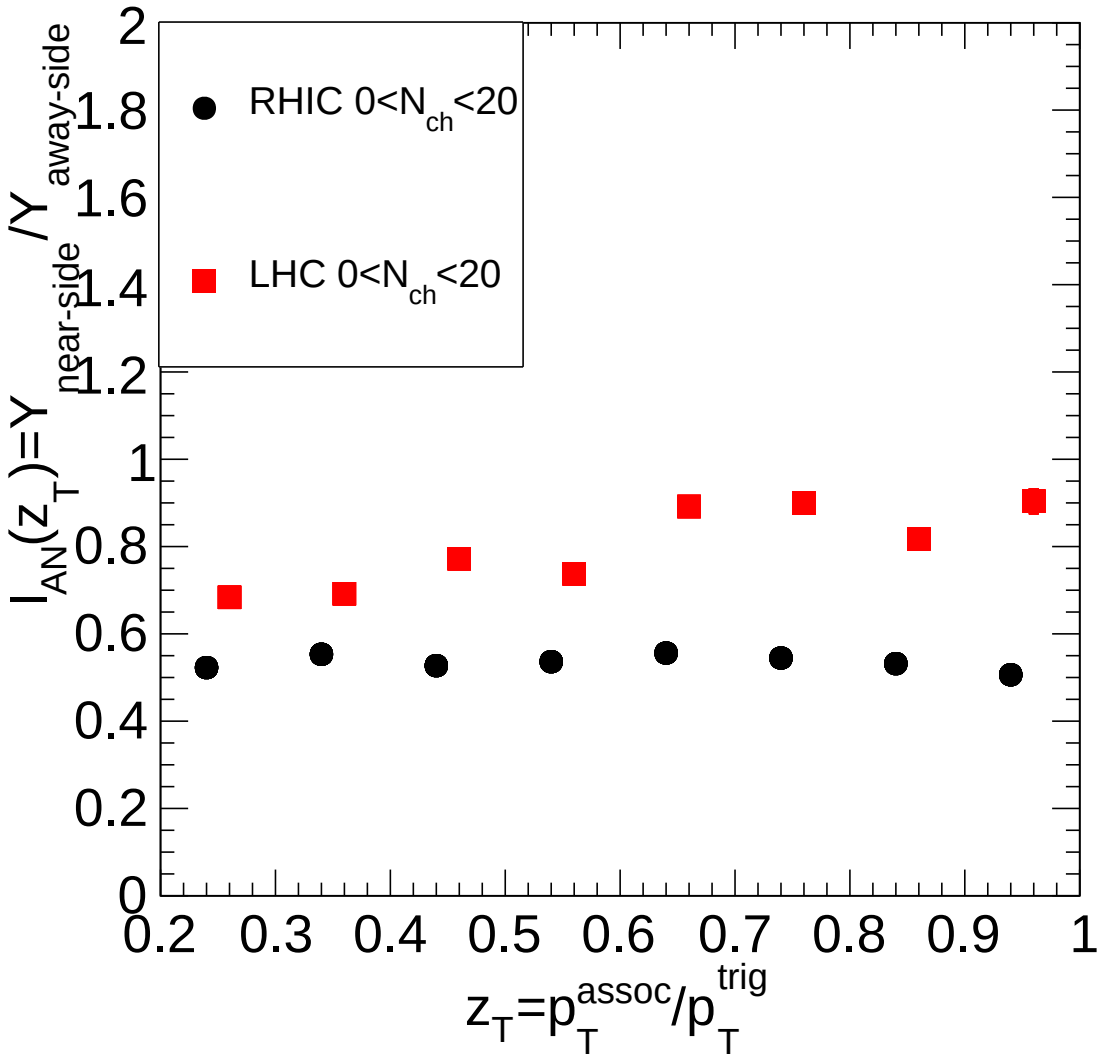

Figure 3.53: Ratio between the near side and far side yields at low multiplicity.

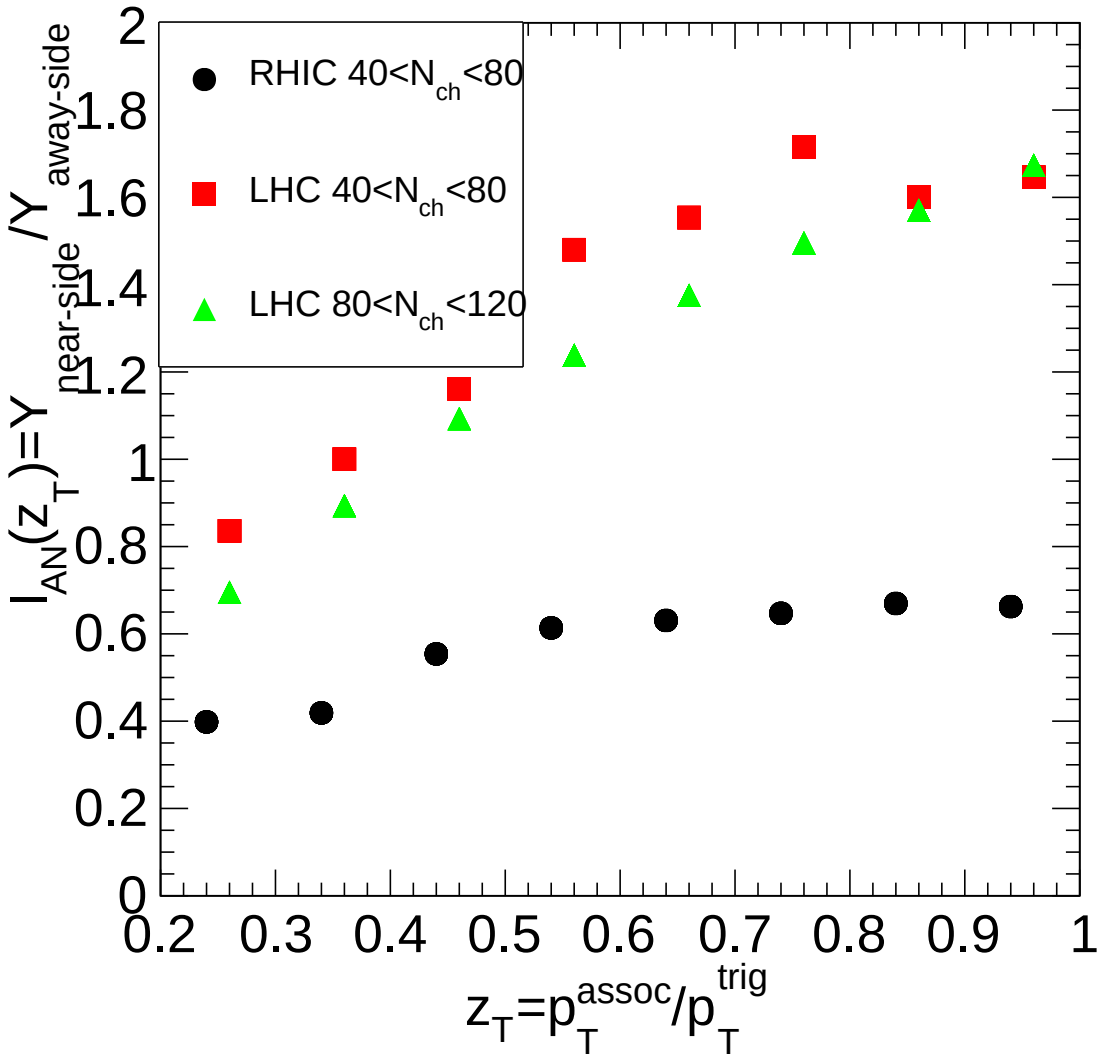

Figure 3.54: Ratio between near side and far side yields at high multiplicity.

Chapter 4

Conclusion and Outlook

A remarkable development of understanding our universe and its formation has been made over the last century. The physics of the early universe is still to be understood in great details. So far, the cosmic microwave background signal represents the earliest signature for the formation of our universe. However the possibility of the QGP formation in the collider experiments could provide more insight about the physics of the first second after the big bang. Therefore the worldwide effort has been carried out by RHIC and LHC in order to search for the QGP formation, the early phase of our universe. Interesting results from RHIC and LHC have indicated the possibility of the QGP formation in the nucleus-nucleus collisions.

The suppression of the spectra of the strongly interacting particles (hadrons) in nucleus-nucleus collisions compared to the nucleon-nucleon collisions at LHC and RHIC suggests the strong interaction between the propagating parton and the formed QCD medium in nucleus-nucleus collisions [25, 26, 30, 31]. These results have been confirmed with the similar spectra of the electromagnetic interacting particles (direct photon) and the weakly interacting particles (Z^0 and $W^{\pm}$) from nucleus-nucleus collisions and nucleon-nucleon collisions. Combining these two sets of results significantly indicates the formation of the QGP in the central nucleus-nucleus collisions (the event with high multiplicity) [22, 36, 37]. However the absence of different levels of suppression for light vs. heavy quarks and quark vs. gluon jets, in contrast to the basic principle of the theory of strong interaction, made the extraction of the medium properties from the measured quantities extremely difficult. This might be due the complexity of the underlying mechanisms for the event in the nucleus-nucleus collisions, therefore the search for the medium formation in nucleon-nucleon collisions might represent a clean environment in order to extract the medium properties from the observables.

This study was proposed to search for the medium effects in nucleon-nucleon

collisions. PYTHIA has been used to simulate the proton-proton collisions of similar energy to RHIC and LHC. The fact that the simulated results of this analysis have shown the suppression of the away side yields compared to the near-side yields at LHC energy for the event of high multiplicity demonstrate the possibility of medium formation in such type of collision.

In summary, the high-multiplicity event in proton-proton collision could be used to create the quark-gluon plasma in a clean environment in order to extract the medium properties which is consistent with the recent published results at LHC. [49]

More insight about the underlying physics of QGP would be provided by comparing the current results to the experimental results, and by studying how the ratio between the near and away side yields evolves with midrapidity and forward rapidity.

Bibliography

[1] Fermi National Accelerator Laboratory, via Wikimedia Commons. Standard Model, 2008.

[2] ATLAS Collaboration. arXiv: 120707214v2. *[hep-ex]*, 2012.

[3] Mark Thomson. *Modern Particle Physics*. Cambridge University Press, 2013.

[4] C. Patrignani et al. *Particle Data Group*. Chinese Physics C, 40, 100001, 2016.

[5] via Wikimedia Commons Lokal_Profil [CC BY-SA 2.5]. Quark confinement, 2009.

[6] David J. Gross and Frank Wilczek. Ultraviolet behavior of non-abelian gauge theories. *Physical Review Letters*, 1973.

[7] Stanislaw Mrowczynski. arXiv: 9905005v1. *[nucl-th]*, 1999.

[8] Rajan Gupta. arXiv: 9807028v1. *[hep-lat]*, 1998.

[9] Ismail Zakout and Carsten Greiner. arXiv: 1002.3119v5. *[nucl-th]*, 2010.

[10] Mark G. Alford et al. arXiv:0709.4635. *[hep-ph]*, 2008.

[11] via Wikimedia Commons Dark Formal [Public domain]. QCD phase diagram, 2006.

[12] Edmond Iancu. arXiv: 1205.0579v1. *[hep-ph]*, 2012.

[13] Antonin Maire. arXiv: 1506.03683v1. *[hep-ex]*, 2015.

[14] P. Rosnet. arXiv:1510.04200. *[hep-ph]*, 2015.

[15] via Wikimedia Commons Tonatsu (Tonatsu's file) [Public domain]. Impact parameter, 2007.

[16] B. Muller. Rep. prog. *Phys. 58:611*, 1995.

[17] John W. Harris and Berndt Muller. arXiv: 9602235v1. *[hep-ph]*, 1996.

[18] Barbara Betz. Jet quenching in heavy-ion collisions. *EPJ Web of Conferences*, 2012.

[19] Martin Spousta. arXiv: 1305.6400v2. *[hep-ex]*, 2013.

[20] Michael L. Miller et al. Glauber modeling in high-energy nuclear collisions. *Annu. Rev. Nucl. Part. Sci. 2007. 57:205–43*, 2007.

[21] D. d'Enterria and B. Betz. Springer lecture nnotes in physics. *(LNP)*, 2009.

[22] S. S. Adler et al. [PHENIX collaboration]. *Phys. Rev. Lett. 94, 232301*, 2005.

[23] S. S. Adler et al. [PHENIX collaboration]. *Phys. Rev. Lett. 91, 241803*, 2003.

[24] S. S. Adler et al. [PHENIX collaboration]. *Phys. Rev. Lett. 96, 202301*, 2006.

[25] J. Adams et al. [STAR collaboration]. *Phys. Rev. Lett. 91, 172302*, 2003.

[26] S. S. Adler et al. [PHENIX collaboration]. *Phys. Rev. C 69, 034910*, 2004.

[27] I. Vitev and M. Gyulassy. *Phys. Rev. Lett. 89, 252301*, 2002.

[28] I. Vitev. *Phys. G 30, S791*, 2004.

[29] David d'Enterria. arXiv: 1207.4362v2. *[nucl-ex]*, 2012.

[30] K. Aamodt et al. [ALICE collaboration]. *Phys. Lett. B 696 (2011) 30.*

[31] S. Chatrchyan et al. [CMS collaboration]. *Eur. Phys. J. C 72 (2012) 1945.*

[32] H. Appelshauser. [ALICE collaboration]. *J. Phys. G 38 (2011) 124014.*

[33] ALICE Collaboration. arXiv: 1203.2160. *[nucl-ex]*, 2012.

[34] S. Chatrchyan et al. [CMS collaboration]. *JHEP 1205 (2012) 063.*

[35] S. Chatrchyan et al. [CMS collaboration]. *Phys. Lett. B 710 (2012) 256.*

[36] CMS Collaboration. arXiv: 1205.6334. *[nucl-ex]*, 2012.

[37] S. Chatrchyan et al. [CMS collaboration]. *Phys. Rev. Lett. 106 (2011) 212301.*

[38] J. Adams et al. [STAR collaboration]. *Phys. Rev. Lett 91 072304*, 2003.

[39] C. Adler et al. [STAR collaboration]. *Phys. Rev. Lett 90 082302*, 2003.

[40] STAR Collaboration. Jet-like correlations with direct-photon and neutral-pion triggers at $\sqrt{s_{_{NN}}} = 200\ GeV$. *Physics Letters B*, 2016.

[41] S. Chatrchyan et al. arXiv: 1009.4122v1. *[hep-ex]*, 2010.

[42] Shaheen Irfan et al. arXiv: 1509.01525v2. *[nucl-th]*, 2017.

[43] Ahmed M. Hamed. arXiv: 14080791v2. *[nucl-ex]*, 2014.

[44] E. V. Shuryak. Azimuthal asymmetry at large p_t seem to be too large for a pure "jet quenching". *Phys. Rev. C*, 2002.

[45] http://home.thep.lu.se/∼torbjorn/Pythia.html.

[46] STAR Collaboration. Identified hadron spectra at large transverse momentum in p + p and d + Au collisions at $\sqrt{s_{_{NN}}} = 200\ GeV$. *Physics Letters B*, 2006.

[47] ATLAS Collaboration. Measurements of top-quark pair differential cross-sections in the lepton+jets channel in pp collisions at $\sqrt{s_{_{NN}}} = 8\ TeV$ using the ATLAS detector. *Eur.Phys.J. C76*, 2006.

[48] V. Alan Kostelecky et al. arXiv: 1610.08755v2. *[hep-ph]*, 2017.

[49] ALICE Collaboration. Enhanced production of multi-strange hadrons in high-multiplicity proton–proton collisions. *[Nature Physics]*, 2017.